# Investigation of Semiconductor Photoanodes for Photoelectrocatalytic Water Splitting

**Yuyu Bu**

A THESIS SUBMITTED FOR THE DEGREE OF
DOCTOR OF PHILOSOPHY

DEPARTMENT OF ELECTRICAL AND
ELECTRONIC ENGINEERING
TOKUSHIMA UNIVERSITY

August 2017

# Abstract

Collecting and storing solar energy in hydrogrn, as plant accomplishes through photosynthesis, is a highly desirable approach to solving the questions of energy shortage and environment pollution. Photoelectrochemical water overall splitting cell is a promising system to achieve this target. It composes by ohmic contacted semiconductor photoanode and photocathode. Now the water splitting performance of photoanode is not high enough, so that influence the performance of PEC water overall splitting cell. There are two main disadvantages to limit the property of photoande. For the one, the transfer capacity of the photogenerated carriers in the photoanode is relative weakness. The other one is that the oxidation energy barrier of the photoanode is too high to limit the water oxidation reaction by photogenerated holes.

Fabrication of crystal point defect (oxygen vacancy) on the surface of the semiconductor has been proved a feasible method to resolve above disadvantages, so that can improve the PEC performance of the photoanode. However, the mechanism is still not clear. Furthermore, to date, only point defects have been employed to modify the photoanode. Other two species of crystal defects, such as line defects and planar defects, have not been studied in this area. So, in this thesis, the modification mechanism of oxygen vacancy on Mo-doped $BiVO_4$ photoanode was investigated. Then the line defect (dislocation) has been prepared on the $WO_3$ nanoflower photoanode, and the functions of the line defect during PEC water splitting have been investigated also.

Firstly, electrochemical reduction method has been employed to treat the surface of Mo-doped $BiVO_4$ (BiMoVO) photoanode. Further experimental data indicated that when the reduction potential located at -0.8 V (vs Ag/AgCl), quasi-oxygen vacancy formed on the (020) facet (only Bi-O bonds cracked on this facet), the electrons mobility of the BiMoVO photoanode increased dramatically, and the PEC current density of it is improved largely. However, with the reduction potential increasing to -1.2 V, oxygen vacancy formed on the surface of (020) facet (both Bi-O and V-O bonds cracked on this facet simultaneously), the PEC current density is decreased obviously. Both experimental and Density Functional Theory (DFT) calculation data pointed out that a moderate level of reduction is a key factor for the adjustment of photoanode performance. Thus, these results demonstrate firstly that oxygen vacancy actually isn’t the positive factor to improve the PEC performance of a $BiVO_4$ photoelectrode, but the quasi-oxygen vacancy forming on the surface of the active facet is.

Secondly, well-defined $WO_3$ nanoflower (NF) photoanodes were fabricated. The sharp edged mountain-like structure of the titaninum substrate plays an important role to induce the $WO_3$ NF structure growth on it. The sharp edge of etched Ti substrate can provide an orientation force to control the nucleus growth process of $WO_3$ nanosheets, and finally to fabricate a flower-like $WO_3$ thin film after hydrothermal growth. The $WO_3$ NF photoanode with 8 hours growth time shows the best PEC performance, a 1.8 mA/cm$^2$ photocurrent density (bias potential 1 V vs Ag/AgCl) could be achieved in $NaSO_4$ electrolyte under 100 mW/cm$^2$ AM 1.5G sun light illumination.

Lastly, point defect such as oxygen vacancy in semiconductor, has been widely evidenced that it can influence the separation and transfer processes of the photogenerated hot charges. Except point defect, to date, scarcely any study focused on expounding the functions of line defect (such as dislocation) in the crystal of semiconductor photoanode and how to influence the photogenerated hot charges separation process. Herein, edge dislocations were found distributed on the $WO_3$ NF crystal photoanode, inducing mismatch of (002) and (020) facets. Further photoelectrochemical performances and DOS calculation results indicated that similar with surface facet heterojunction, a heterojunction system could be formed along the dislocations line due to the energy difference between the (002) and (020) facets. So, this present study provided a new understanding of the line defect in the photogenerated hot carrier separation process, and provided a novel method to improve the properties of photoelectrodes and photocatalytic materials in the near future.

Keyword: Quasi-oxygen vacancy; Edge dislocation; Mo-doped $BiVO_4$; $WO_3$ nanoflower; Photoelectrochemistry

# Outline

# Chapter 1：Background of the research

## §1.1. Background

Today, fossil fuels such as coal, oil and gas are the main energies to maintain humans live demand and supply the industrial development. However, there are two urgent questions about fossil fuels during them application process, including limited shortage capacity and environment pollution. According to statistic, the exploit time about coal and oil are both less than 50 years, so the energy crisis will coming very soon. [1-2] Meanwhile, there are many environment pollution gases (such as $CO_2$, $NO_x$ and $SO_x$, etc.) [3] emission during fossil fuels application, so that bring great pressure to the earth ecological system. Thus, in this era, developing sustainable new energy is the core method to resolve the energy crisis and environment pollution questions.

Solar power is the origin of the all fossil fuels. It is inexhaustible but decentralized energy resource. The total energy of the solar energy arriving the surface of earth every second is equal to 130 million power plants with a generated energy 500 MW every unit,[4] so solar energy is the optimal clear energy to supply our energy consumption. However, the solar energy can't be used directly because of the photons is the energy carrier. So, some green methods should be developed to converse the solar energy into others available energy forms such as electric energy, chemical energy, thermal energy and biomass. Furthermore, for the solar energy conversion method developing, there are three main points should be considered. Firstly, the conversion efficiency of the method should be improved, photon energy from the sun needs to be efficiently converted into electric and chemical fuel that can be used, transported, and stored. Secondly important point is to provide stable and constant solar energy flux for the persistent conversion. Lastly, we need develop some cost effective method to push the solar energy conversion technology into terawatt scale.[5]

Hydrogen, with high energy capacity and environmental friendly characteristics, has been widely considered as a great potential energy carrier in next-generation energy scenarios. Up to now, electrocatalytic water splitting for hydrogen and oxygen evolution is the mainly method for hydrogen gain. As shown in Figure 1-1, under standard conditions, the free energy barrier for the complete splitting of one molecule of $H_2O$ into hydrogen and oxygen is $\Delta G = 237.2$ kJ/mol, which corresponds to $\Delta E =$ 1.23 V per electron transferred (according to the Nernst equation).[6] This is not a idea method for hydrogen preparation, because of the extra electric energy consumed in during this reaction process. So, some more idea methods should be developed.

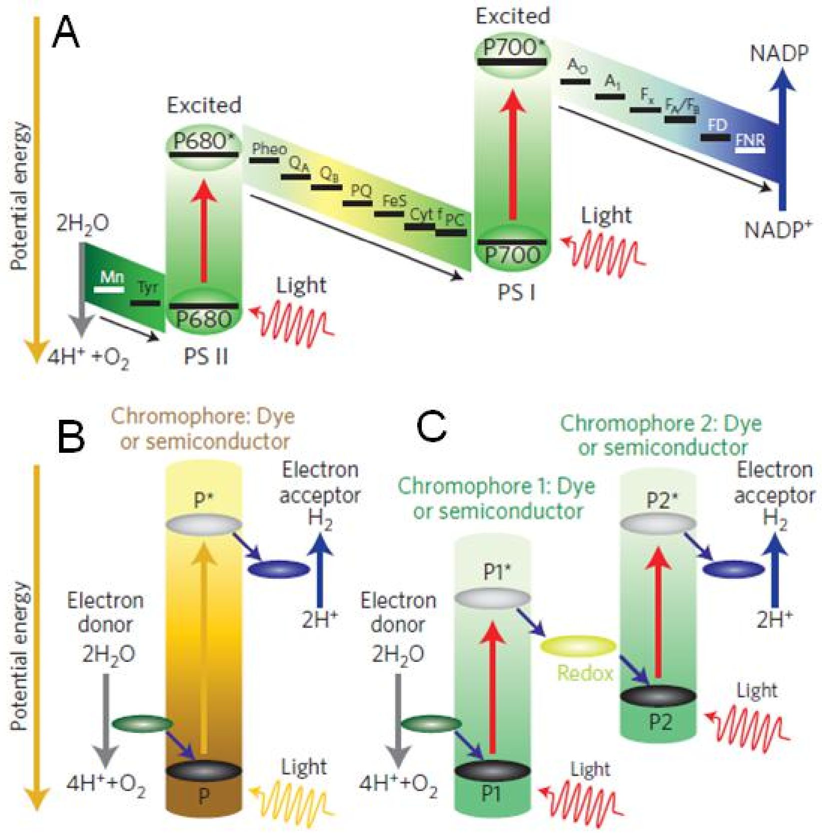

**Figure 1-1.** Photosynthesis of the plant and the artificial photosynthesis (water splitting).[6]

Photosynthesis, which provided by plants, is the most important reaction for the all biology on the earth. During the reaction, as shown in Figure 1-1A, $CO_2$ and $H_2O$ can be fixed, and transfer to organic sugar and $O_2$ by electron transfer chain after absorption the solar energy. So, artificial photosynthesis is an idea approach to resolve the energy shortage crisis of the world. Artificial photosynthesis for water splitting, as shown in Figure 1-1B and 1-1C, is a potential method for the solar energy conversion. In this reaction system, semiconductor is the core role to realize the water splitting by photovoltaic effect. The photogenerated electrons and holes can cross the water redox reaction energy barrier, so that replacing the extra applied electric energy to drive the water splitting reaction. This artificial photosynthesis method, so-called photoelectrochemical (PEC) or photocatalysis water splitting, has been investigated more than 40 years. However, there is a long way should go to push the performance of this technology to a practical application level.

## §1. 2. Working principle of PEC water splitting

Photoelectrochemical splitting is one method that it uses light-electricity to split water into hydrogen and oxygen. The mechnisem of PEC splitting water is similar to that of the photocatalysis technology. The difference between them is that PEC involves external circuit. The external circuit can further provide the external voltage on the basis of photocatalysis, promoting the bending of the band, and further facilitating the separation and transport of the photogenerated carriers.

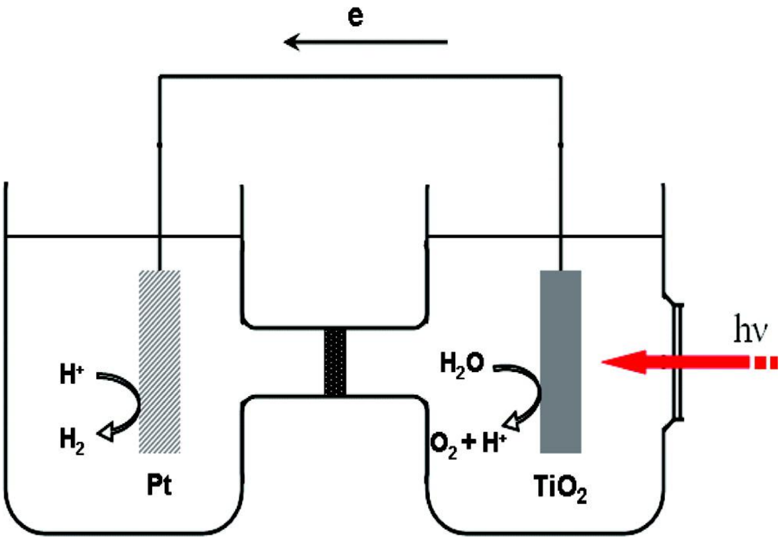

**Figure 1-2.** Schematic diagram of water splitting in photoelectrochemical cells

Traditional PEC cell is shown in Figure 1-2 (take the photoanode as an example), which can converts light energy into chemical energy. The photoanode fabricating by n-type semiconductor materials, can generate electron-hole pairs after incident light illumination. The electrons generated on the semiconductor conduction band flew through the outer circuit to the counter electrode, and reduce with the protons in the water to produce hydrogen on the surface of counter electrode. This cell system includes a photoanode (a kind of metal oxide) and a cathode (usually Pt). In the electrolyte, the oxidation and reduction reactions occur on the surface of anode and the cathode, respectively.

The reaction mechanism mainly shows as follows:

Photoanode: $h\gamma \rightarrow e^- + h$ (1-1)

$h + H_2O \text{ (liquid)} \rightarrow 1/2\ O_2 \text{ (gas)} + 2H^+$ (1-2)

Photocathode:

$2H^+ + 2e^- \rightarrow H_2 \text{ (gas)}$ (1-3)

Total reaction equation:

$$2h\gamma + H_2O\ (\text{liquid}) \rightarrow 1/2\ O_2\ (\text{gas}) + H_2\ (\text{gas}) \qquad (1\text{-}4)$$

In PEC systems, splitting water happens at the interface between the electrode and the electrolyte. When the semiconductor material immerses in the electrolyte, the electrons will transfer between the semiconductor and electrolyte until the Fermi level of oxide semiconductor ($E_F$) level off to redox potential of electrolyte ($E_0$). Meanwhile, a junction region is formed at the interface between the semiconductor and the electrolyte. In the junction region of the semiconductor, the charge density and distribution are different from that of the semiconductor bulk. The junction region is the space charge layer, which plays a key role in charge separation process. In the region of the built-in electric field, the electrons in the semiconductor move to opposite directions to the original electrons. In the junction area on the side of the electrolyte, a double layer (Helmholtz layer) is formed, which one connects in series with the space charge layer in the semiconductor. Specifically, according to the actual difference between the $E_F$ and the $E_0$, the band bending at the contact interface is also different. The Fermi level and band transition of the semiconductor with different conduction type are different from that of electrolyte. The semiconductor of n-type contacts with electrolyte tend to form different types of contact, including flat band contact, accumulation type contact, depletion type contact and inversion layer contact. However, the most common one is the depletion type contact, as shown in Figure 1-3(a). Usually, the Fermi level potential of n-type semiconductor is higher than the redox potential of the electrolyte before contacting, so the electrons in the conduction band of semiconductor transfer to the electrolyte, resulting in a depletion space charge area near the surface of semiconductor. When the system reaching equilibrium, the $E_F$ of the semiconductor is consistent with the redox potential ($E_0$) of the electrolyte, while the band of the semiconductor in the space charge region shows a upwards bending toward the electrolyte. Under the influence of the electric field in the space charge region, the photogenerated hole shifts towards the electrolyte, and then participate in oxidation reaction. However, the p-type semiconductor is the opposite. As shown in Figure 1-3(b), the p-type semiconductor is usually formed an accumulation type contacts after contact with an electrolyte. The electrons are injected from the electrolyte into the semiconductor, inducing downward bending toward the electrolyte. Then, the photogenerated electrons move towards to the electrolyte, participating in reduction reaction.

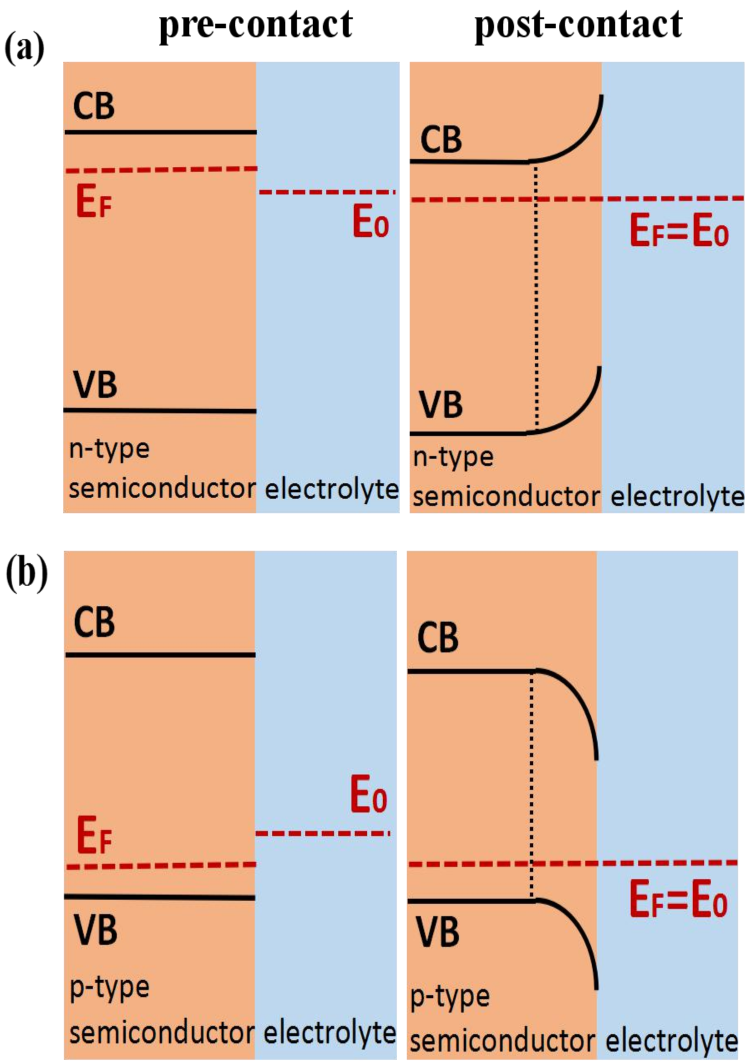

**Figure 1-3.** The Fermi level movement and band bending of n-type semiconductors (a) and p-type semiconductors (b) after contact with the electrolyte.

### 1.2.1 Photoanode

In the PEC cell, the semiconductor thin film on conduction substrate is used as the working electrode. It is connected with the counter electrode by external circuit and electrolyte ions conductor.

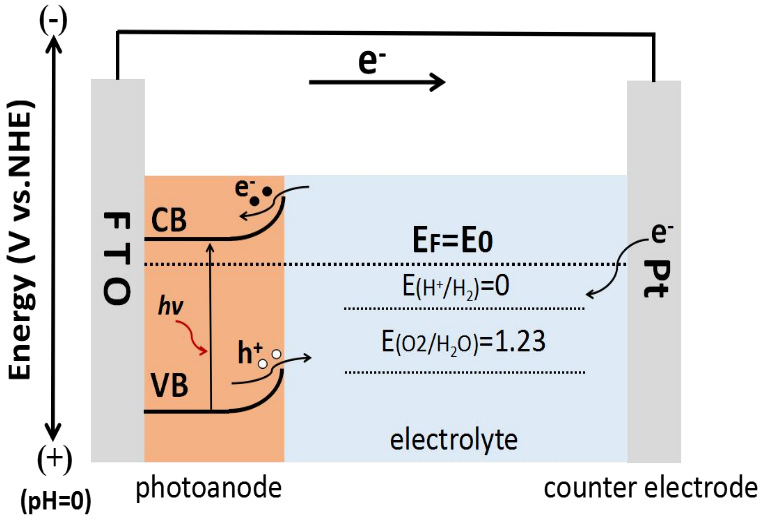

**Figure 1-4.** The schematic diagram of the potential of photoelectrochemical water splitting on n-type semiconductor as photoanode.

For n-type semiconductors (Figure 1-4), as the photoanode, if the light energy higher than the bandgap energy of the semiconductor, the holes produced in the valence band will transfer to electrolyte. If the potential of the n-type semiconductor valence band is more positive than 1.23 V vs. NHE (pH = 0), the resulting photogenerated holes can oxide the water for oxygen evolution. At the same time, the electrons generated on the semiconductor conduction band will transfer to the conductive substrate, arriving the counter electrode by extra circuit, and then participating in water reduction for hydrogen evolution [7].

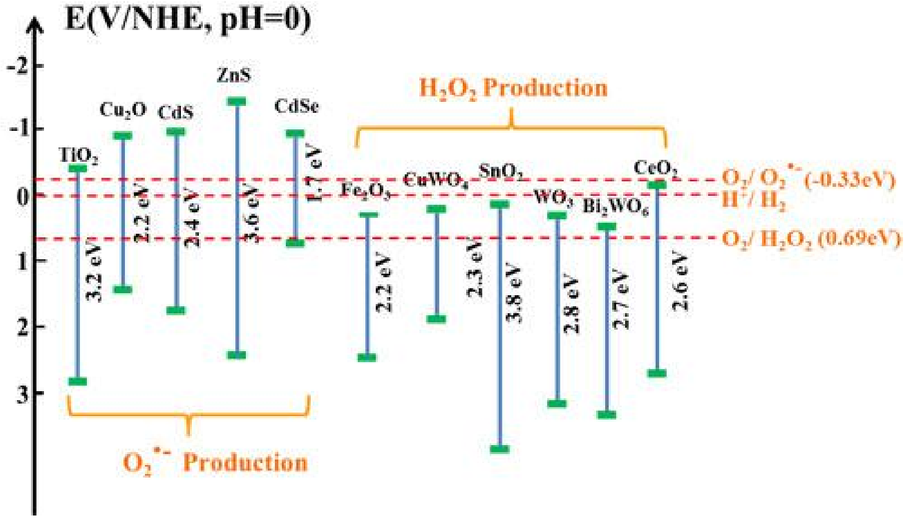

**Figure 1-5**. The band position of the partial semiconductor materials and the oxidation-reduction potential of the water.

Since Fujishima and Honda first reported that $TiO_2$ can be used as PEC water splitting material[8], the research field has received more and more attention. Photoanode materials should satisfy some special requirements including narrow band gap, negative enough conduction band potential and valence band potential for water splitting (Figure 1-5 shows the band structure of semiconductors[9]), high electron transfer rate, high stability in liquid phase and low cost. However, to date, no semiconductor has yet met all of these requirements. In order to increasing the utilized efficiency of solar energy, to develop visible light responsive photoanode materials are the initial question. Visible light accounts for 40% of the total solar energy, with the range of 400 to 800 nm, indicating that the band gap of semiconductors is suitable in 1.56 to 3.12 eV. Some Fe based materials (including $\alpha$-$Fe_2O_3$，$CaFe_2O_4$，$ZnFe_2O_4$，FeOOH), Bi based materials, such as $BiVO_4$, Ta based materials such as TaON, $Ta_3N_5$, W based materials such as $WO_3$ and $BiWO_4$, all meet the band gap requirements.

### 1.2.2 Photocathode

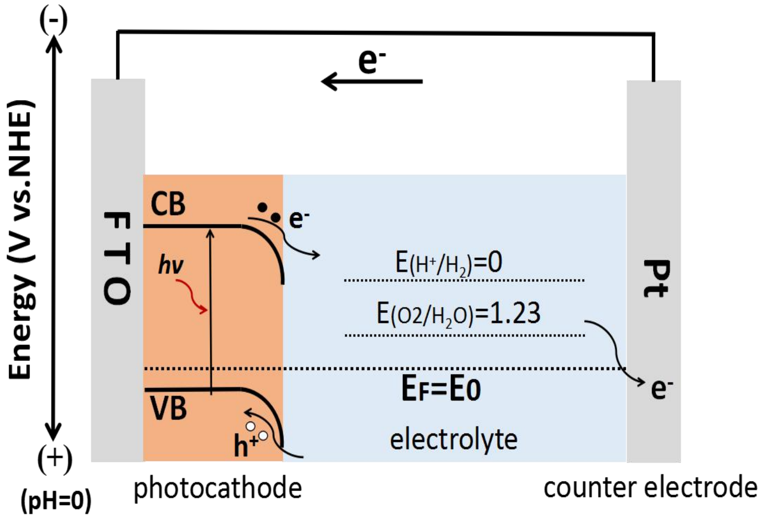

**Figure 1-6.** The schematic diagram of the potential of photoelectrochemical water splitting on p-type semiconductor as photocathode.

Among many semiconductor electrodes, the research of the photocathode is mainly focused on several kinds of p-type semiconductor materials such as Si, InP, $CuIn_{1-x}GaxS(Se)_2$, $Cu_2ZnSnS_4$ and so on [10-12]. The work of the p-type mechanism shows in Figure 1-6.

### 1.2.3 Photoanode-photocathode tandem overall water splitting cell

The complete water splitting includes the following reduction and oxidation reactions (compared to the reaction potential of reversible hydrogen electrodes (RHE)):

Reduction reaction:

$2H^+ + 2e^- \rightarrow H_2$ （$E_{red} = 0.00$ V vs. RHE） (1-5)

Oxidation reaction:

$2H_2O + 4h^+ \rightarrow O_2 + 4H^+$ （$E_{ox} = -1.23$ V vs. RHE） (1-6)

Total reaction equation:

$2H_2O \rightarrow 2H_2 + O_2$ ( $\Delta E = -1.23$ V) (1-7)

The photoanode and photocathode can be connected in series and used PEC overall water splitting without any extra applied potential. As shown in Figure 1-7, in p/n dual-photon photoelectrochemical water splitting cells. In this series cell, it requires that the n-type semiconductor valence band position below the oxidation potential of $O_2/H_2O$ and the p-type semiconductor conduction band position higher than the reduction potention of $H^+/H_2$. After deducting the optical absorption loss, the conversion efficiency of solar energy to hydrogen energy can reach 27% [13] by this type series PEC overall water splitting cell. The first reported p/n dual-photon PEC complete water splitting cell consisting of p-GaP and n-$TiO_2$, the conversion efficiency is less than 1% [14].

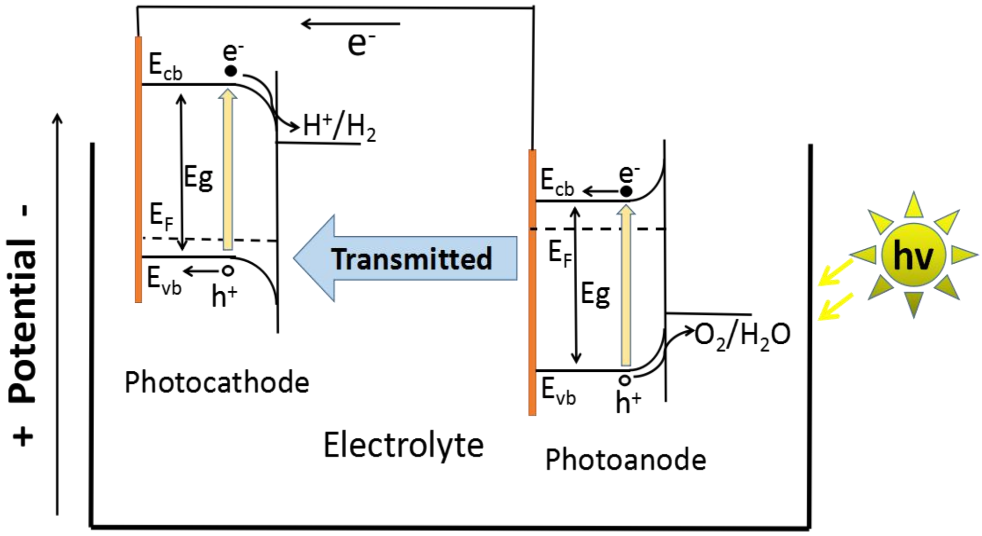

**Figure 1-7.** The schematic diagram of photoanode-photocathode series complete water splitting cell

p-CdTe/n-$TiO_2$, p-GaP/n-$SrTiO_3$, p-CdTe/n-$SrTiO_3$, p-SiC/n-$TiO_2$, p-$Fe_2O_3$/n-$Fe_2O_3$

and other dual-photon PEC water splitting cells have also been reported [15-18]. However, all of their solar energy conversion efficiency below 1%. Kainthla had reported a p-InP/n-GaAs dual-photon water splitting cell with a solar conversion efficiency of 8.2% [19]. However, the use of a large number of rare elements and poor stability limits its practical application [20].

## §1.3. The methods for PEC or photocatalytic performance improving

### §1.3.1. Semiconductor doping

As mentioned above, the study of photoelectrochemical water splitting materials was from the beginning of $TiO_2$, which a wide bandgap semiconductor, could only absorb ultraviolet light, which greatly affected its utilization of the sunlight, thus affecting the effect of photoelectrochemical water splitting. By metal and non-metallic element doping and other methods can effectively increase the absorption wavelength of the semiconductor, that's the methods commonly used by researchers. The range of elements used for ion doping is extensive, involving non-metallic ions, transition metal ions and other polymer ions. The semiconductor photocatalyst can reduce the band gap by doping the impurity element so that the light absorption spectrum range is widened to visible light. It's mainly because the molecular orbital of the dopant ion or element can coincide with the O 2p orbit to form an impurity level between the semiconductor bandgaps. This is equivalent to raising the position of the valence band, corresponding to reduce the band gap of the semiconductor. Therefore, on the one hand, for the wide bandgap semiconductor materials such as $TiO_2$, $SrTiO_3$ and ZnO, researchers narrowed its bandgap, broaden its light absorption range and make it visible photocatalytic activity through the doping of metal and non-metallic elements; on the other hand, looking for some narrow bandgap semiconductor materials with visible photocatalytic activity, it can further improve its catalytic performance by doping with external elements. These narrow bandgap semiconductors are g-$C_3N_4$, $WO_3$, CdS, $MoS_2$, $BiVO_4$, $Ag_3PO_4$, $CuInS_2$, $CuWO_4$, α-$Fe_2O_3$ and so on. But the modification by element doping is not the best method. It is possible that the incorporation of elements in the semiconductor may become new recombination center, promoting the combination of photogenerated electrons and holes, thereby reducing the efficiency of photoelectrochemical water splitting.

**Metal doping**. Generally speaking, metal doping elements mainly include p-type metal elements such as Bi, Sn, Ag and so on, and transition metal elements. The transition metal ions doped into the lattice could change the material crystal field to produce energy level decomposition, and then light irradiation caused d-d electron transition to enhance photocatalytic efficiency. Studies have shown that there is small lattice mismatch between $SnO_2$ and $TiO_2$, therefore, doping $TiO_2$ with Sn or $Sn^{4+}$ leads to good structural compatibility and stability. Xu et al. [21] prepared Sn-doped $TiO_2$ nanowire arrays by one-step hydrothermal method. As shown in Figure 1-8, Sn-doped $TiO_2$ nanowires revealed that the photocurrent density increased to 2.0 mA/cm$^2$ at 0 V vs. Ag/AgCl under 100 mW/cm$^2$ simulated sunlight illumination. The incident-photon-to-current conversion efficiency showed that the increase of photocurrent was mainly due to the enhancement of photocatalytic activity, and the electrochemical impedance test revealed that the Sn doping can significantly improve the density of n-type charge carriers.

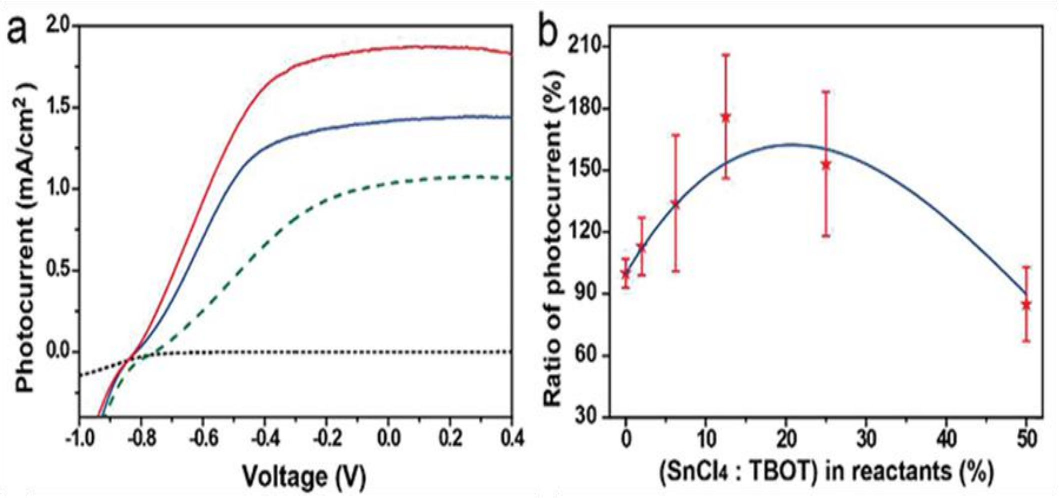

**Figure 1-8.** (a) Line sweep voltammograms of pristine $TiO_2$ NWs (green), Sn/$TiO_2$-6 NWs (blue), and Sn/$TiO_2$-12 NWs (red). (b) Ratio of measured photocurrent density between Sn/$TiO_2$ NW and pristine $TiO_2$ NW photoanodes at 0 V vs Ag/AgCl for different Sn doping ratios.

Das et al. [22] prepared bulk-Nb-doped $TiO_2$ nanotube layers by self-organizing anodization of Ti-Nb alloys. At Nb-contents around 0.1 %, a strongly increased and stable photoelectrochemical water splitting efficiency is obtained. Li et al. [23] reported a microwave-assisted reduction method with $NaBH_4$ to prepare $Ti^{3+}$ self-doped $TiO_2$ nanotube arrays (MR-TNTs). UV-vis diffuse reflection spectra showed that the light absorption spectrum range extended to the visible light region and the EIS indicated that the induced oxygen vacancies of MR-TNTs enhanced their charge separation and electrical conductivity. The photocurrent density and photoconversion efficiency under AM 1.5G irradiation were determined as 3.05 mA/cm$^2$ at 1.23 V vs. RHE and 1.66 %, respectively.

For $SrTiO_3$ with a band gap of 3.2 eV, a Rh-doped $SrTiO_3$ photocatalyst electrode that was readily prepared by Iwashina et al. [24] had a visible-light response and produced a cathodic photocurrent under visible light irradiation. When the introduction of trivalent ions such as $Al^{3+}$, $In^{3+}$ and $Cr^{3+}$ to $\alpha$-$Fe_2O_3$, it will lead to the formation of oxides with the same structure as $\alpha$-$Fe_2O_3$, which will affect the crystal of $\alpha$-$Fe_2O_3$. For example, the radius of $Al^{3+}$ is less than $Fe^{3+}$, $Al^{3+}$ doped $\alpha$-$Fe_2O_3$ leads to a narrowing lattice of the $\alpha$-$Fe_2O_3$, promotes the polar transition, and increases the conductivity of $\alpha$-$Fe_2O_3$. In non equivalence doped $\alpha$-$Fe_2O_3$, $Ti^{4+}$ and $Sn^{4+}$ doped $\alpha$-$Fe_2O_3$ are the most widely studied. Hahn et al. [25] prepared $\alpha$-$Fe_2O_3$ doped with Ti/Sn by coevaporating iron and Ti/Sn in oxygen ambient. It was showed that the deposition angle had a significant influence on the photoelectrochemical water splitting performance, and the maximum photocurrent was achieved for films grown at 75° . The IPCE of Ti-doped films deposited under optimum conditions reached 31 % at 360 nm and 1.4 V vs. RHE, better than that of the Sn-doped $\alpha$-$Fe_2O_3$ films prepared uwasnder the same conditions. The enhanced photoconversion efficiency through $Ti^{4+}$ or $Sn^{4+}$ incorporation mainly due to the formation of the strong electric field near the surface of the film, which both improved the electrons transport and inhibited the recombination.

**Nonmetal doping**. There are many non-metallic doping elements reported in the papers, such as C, N, Si and so on. Hoang et al.[26] reported that nitrogen can be incorporated into the $TiO_2$ lattice via nitridation in $NH_3$ flow at 500 °C, the low-energy threshold of the IPCE spectra of N-doped $TiO_2$ nanowires is 520 nm, and it remains as high as 18 % at 450 nm, as illustrated in Figure 1-9. Chen et al.[27] found that the silicon doping and heat treatment had synergic effect on $TiO_2$ nanorod films by increasing its crystallinity, oxygen vacancies and hydrophilicity as well as improving the electronic properties. The silicon-doped $TiO_2$ nanorod flims showed enhanced photocurrent density up to 0.83 mA/cm$^2$ at 1.23 V vs. RHE, under AM 1.5G irradiation and without any cocatalysts, which were expected to provide efficient solar water oxidation .

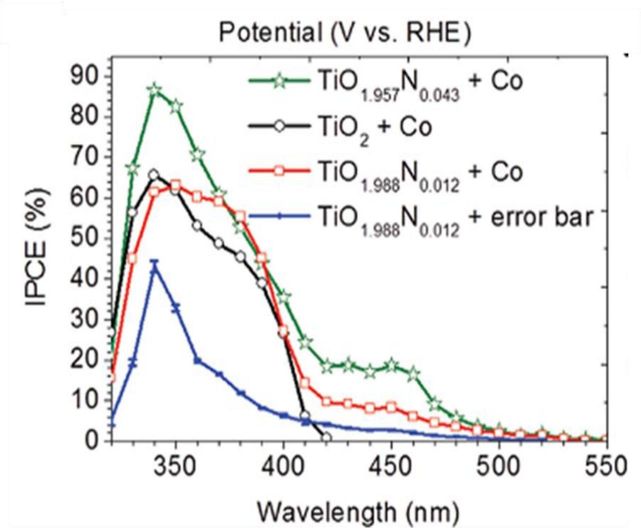

**Figure 1-9.** IPCE spectra of N-modified $TiO_2$ films at 1.4 V RHE: blue and red curves are the corresponding IPCE spectra of the $TiO_{1.988}N_{0.012}$ photoelectrode, black curve is the IPCE of unmodified $TiO_2$ sample after cobalt treatment, and green curve is the IPCE of the $TiO_{1.957}N_{0.043}$ pretreated with cobalt.

Qiu et al. [28] incorporated N on the basis of branched ZnO nanotetrapods, and the photocurrent density achieved a remarkable enhancement to 0.99 mA/cm$^2$ at 0.31 V vs. Ag/AgCl. The enhanced photocurrent is due to the increased roughness factor for boosting light harvesting associated with the ZnO nanotetrapod branching, and the extended visible light absorption of N-doping. Subsequently, Wang et al. [29] introduced N ions into the ZnO nanorod array by ion implantation method. As shown in Figure 1-10, N doping did not change the rod-like morphology of ZnO NRAs, but extended the optical absorption edges to 550 nm. Furthermore, the gradient N dopant distribution led to the formation of terraced band structure and electric field, which improved the separation efficiency of photogenerated electrons and holes of ZnO.

It has been found that there are some surface states on the surface of α-$Fe_2O_3$ photoanode as the recombination center of photogenerated holes and electrons. These surface states capture photogenerated holes and electrons, which are detrimental to photocatalytic oxidation of water. These surface states can be passivated by surface treatment, which can effectively reduce the recombination efficiency of surface electrons and holes and enhance the photoelectrochemical activity. Chemelewski et al.[30] deposited Si and Fe via RBD method to incorporate Si into $\alpha$-$Fe_2O_3$. The extraction efficiency revealed that Si-doping increased the photocurrent of films mainly by improving charge migration. It is concluded that Si can passivate the hematite surface and helps charge transfer to the solution.

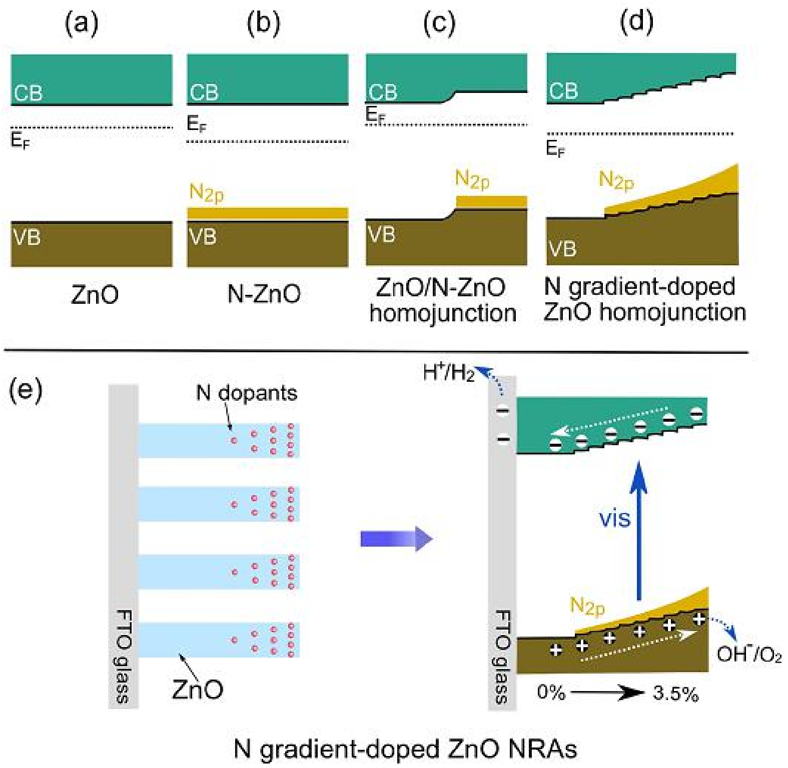

**Figure 1-10.** Energy band schematics of (a) pristine ZnO, (b) N doped ZnO, (c) ZnO/N-ZnO homojunction and (d) N gradient-doped ZnO homojunction, (e) Schematics of N gradient-doped ZnO NRAs and terraced band structure promoting charge separation.

### 1.3.2. Heterojunction composite system

Photogenerated carrier recombination is one of the important factor to limit the performance of the photoanode. So many modified methods were developed to inhibit this process to improve the PEC performance of photoanode.

The establishment of heterojunction can effectively improve the separation of photogenerated carriers. The construction of composite semiconductor heterojunction system generally follow the following principles: (i) The different semiconductor potentials of the composite structure should match, and the band gap between the two semiconductors is the driving force for separating the photogenerated charge. (ii) The semiconductor coupling interface should form a close ohmic contact, facilitating the migration of electron-holes at the interface, avoiding the formation of composite centers. (iii) After the separation of the charge, the electron acceptor side semiconductor is electronically transported, and the hole receptor side semiconductor has good hole migration ability. According to the band bending and carrier migration at the interface of composite semiconductor, the heterogeneous structure can be divided into three types: straddling type, staggered type and p-n type.

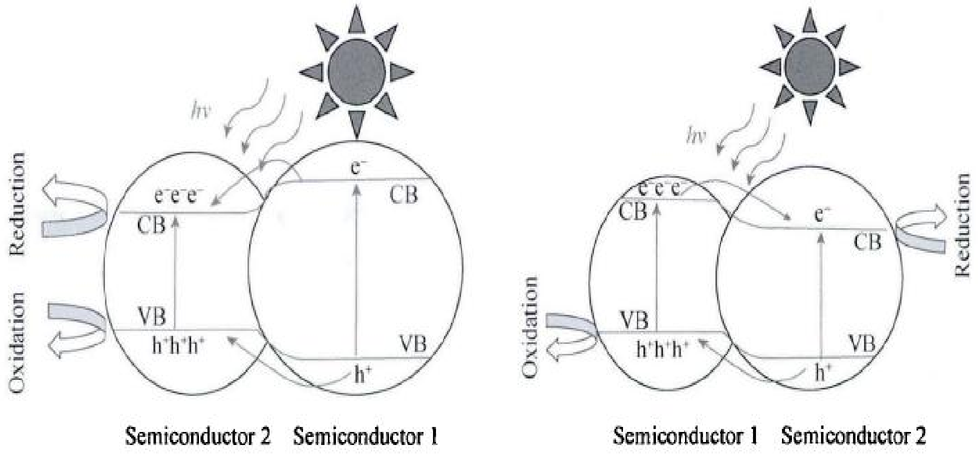

(a) Straddling alignment (b) Staggered alignment

**Figure 1-11.** Schematic of energy band structure and charge transfer process of the heterostructured semiconductors.

**Straddling type and staggered type.** Figure 1-11 shows the energy band structure and charge transfer diagram of the straddling and staggered heterostructure. As shown in Figure 1-11, the straddling type semiconductor is composed of a wide band gap semiconductor 1 coating a narrow band gap semiconductor 2. This band structure with decreasing gradient can absorb the solar energy to the maximum extent. Due to the difference of the potential energy between the conduction band and valence band of the semiconductor, the band bending occurs at the contact interface, thus, the electrons and holes excited by the semiconductor 1 flow to the semiconductor 2 and undergo redox reactions at the semiconductor 2 under illumination. In the staggered alignment, the valence band and conduction band of semiconductor 1 are higher than semiconductor 2, photogenerated electrons and holes migrate in the opposite direction under the driving of band bending, photogenerated electrons migrate from high to low along the conduction band, and the hole moves from low to high along the valence band. In generally, the level shift is more conducive to the separation of photoinduced electron hole.

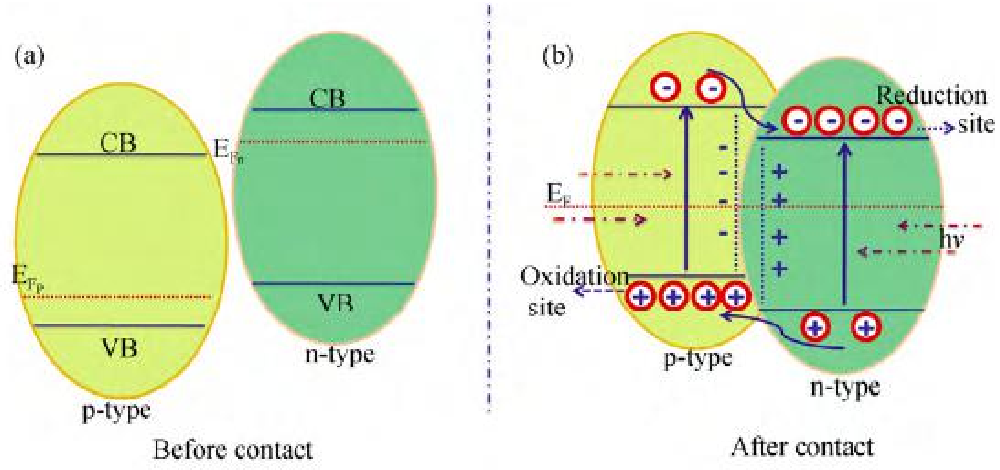

Figure 1-12 (a) Band alignment of p-type and n-type semiconductors before contact and (b) transportation of the charge carries in p-n type heterostructure

The band gap of CdS is about 2.4 eV, and the flat band potential is about -0.9 V vs. NHE. It is a visible light responsive semiconductor material. However, there is severe light corrosion in the process of water splitting by CdS. The photogenerated hole will oxidize CdS in $S^{2-}$ and release $Cd^{2+}$ simultaneously. As a result, CdS is often constructed with other broadband gap semiconductors such as CdS/$TiO_2$ [31], CdS/ZnS [32], CdS/ZnO [33] and so on. It is of great significance to find an environmentally friendly and visible light responsive photocatalytic material due to the environmental pollution of $Cd^{2+}$ released by CdS during photocatalysis [34]. $BiVO_4$ gets more and more attention due to its non-toxic, visible light response characteristics (Eg~2.4eV), but the oxygen evolution of short hole migration distance and high potential disadvantages, making it difficult to split water as single photocatalyst. $BiVO_4$ can be used with many oxide semiconductor constitute staggered type composite structure, such as $WO_3$ [35], $Fe_2O_3$ [36], ZnO [37], $TiO_2$ [38]. $WO_3$ is widely concerned due to the good electron conduction ability, the strong UV response, matching well with $BiVO_4$. First of all, $BiVO_4$ absorbs visible light, while ultraviolet light is absorbed by $WO_3$. The photon energy can be captured most efficiently by gradient absorption of incident light at different wavelengths. Secondly, because the conduction band and valence band positions of $WO_3$ are below $BiVO_4$, an interlaced band bend is formed at the heterojunction, which is beneficial to the separation of photogenerated carriers and to the enhancement of photoelectric conversion efficiency.

**P-n type**. Semiconductors can be divided into n type semiconductors relying on electron conduction and p-type semiconductors relying on hole conduction. After different types of semiconductors are combined, a stable positive and negative ion region is formed at the interface due to the carrier diffusion, that is, the p-n junction. Because of the strong electron mobility of n-type semiconductors and the strong hole conduction ability of p-type semiconductors, so p-type semiconductor is used as hole acceptor, and n-type semiconductor as electron acceptor can enhance carrier mobility. In addition, the p-n junction is oriented from n-type to p-type and the built-in electric field E can further accelerate the separation of photogenerated electrons and holes.

As shown in Figure 1-12a, the n-type semiconductor Fermi level is near the conduction band, and the p-type semiconductor Fermi level is near its valence band. After contacts, with the proliferation of electrons and holes, p-type semiconductor band can be moved on and n-type semiconductor energy band down. When the drift current and diffusion current offset, the interface near the formation of space charge area generated built-in electric field. When the two semiconductors are illuminated at the same time, the electrons are rapidly transferred to the n-type semiconductor under the built-in electric field, and the holes are rapidly transferred to the p-type semiconductor, thus effectively promoting the separation of the photogenerated carriers (Figure 1-12(b)). As a p-type semiconductor, $CaFe_2O_4$ can be combined with a variety of n-type semiconductor to form p-n junction. Lee et al. Explored the first p-n heterojunctions such as $CaFe_2O_4$/ $MgFe_2O_4$ [39]， $CaFe_2O_4/PbBi_2Nb_{1.9}W_{0.1}O_9$ [40]. The promoting effect of p-n heterojunction on photogenerated carrier separation was proved by using $H_2O_2$ as the hole trapping agent. Ahmed[41] et al. obtained anisotropic β-FeOOH nanorods by solution method through adding $CaCl_2$ to $FeCl_3$ solution, the co-deposited $Ca(OH)_2$ and β-FeOOH were annealed twice to form p-$CaFe_2O_4$/n-$Fe_2O_3$ heterojunction, and the photocurrent was nearly doubled.

Semiconductor composite structure can effectively improve the photocatalytic efficiency, and show significant role in the efficient use of sunlight, improved electron-hole separation efficiency and reduced over-potential. Different semiconductor systems have their own characteristics: the straddling type structure can be gradient to efficiently absorb solar energy, but the disadvantage is that photogenerated electron holes are flowing to narrow bandgap semiconductors, can not effectively hinder the electron hole recombination; While the staggered structure of electron holes in the band under the conditions of bending in the opposite direction of separation. The built-in electric field in p-n type structure can quickly separate the generated photogenerated charge. The results show that the construction of heterojunction can effectively improve the photoelectrochemical properties of the photoelectrode.

### 1.3.3 Surface modification

Surface modification is another effective way to improve the photoelectrochemical efficiency of photoelectrode. By surface modification, the segregation of the surface or near surface state of the photoconductor can be removed and reduced, and these surface states are generally used as the composite centers of photogenerated carriers. In the synthesis of materials, due to the surface layer of the potential field and the body phase is different, will form a defect, impurity adsorption and other surface morphology. In order to reduce the Gibbs free energy of the system, solid solution or alloy will also form segregation phase on the surface, which are not conducive to enhance the performance of the electrode. Therefore, the surface or interface modification on the photoelectrochemical thin film electrode is a direct and effective method for improving the performance of photoelectrochemical cracking water.

**Metal/Carbon Material Surface Modification Semiconductor Electrode**. The surface modification of the semiconductor photoelectrode with metal can effectively improve the photoelectrochemical cracking water capacity of the material. For instance, Liu et al. reported that the PEC water splitting performance of Au NP-covered $TiO_2$ films under visible-light stimulation was enhanced 66-fold [42]. As shown in Figure 1-13, it is found that the surface plasmon effect caused by Au surface modification effectively broadens the range of the photoreaction of the composite electrode, extends from the ultraviolet region to the visible region, and electromagnetic field simulation experiments show that the enhancement of local electric field strength on $TiO_2$ surface is the main reason to improve the photoelectrochemical performance of composite photoelectrode in visible region.

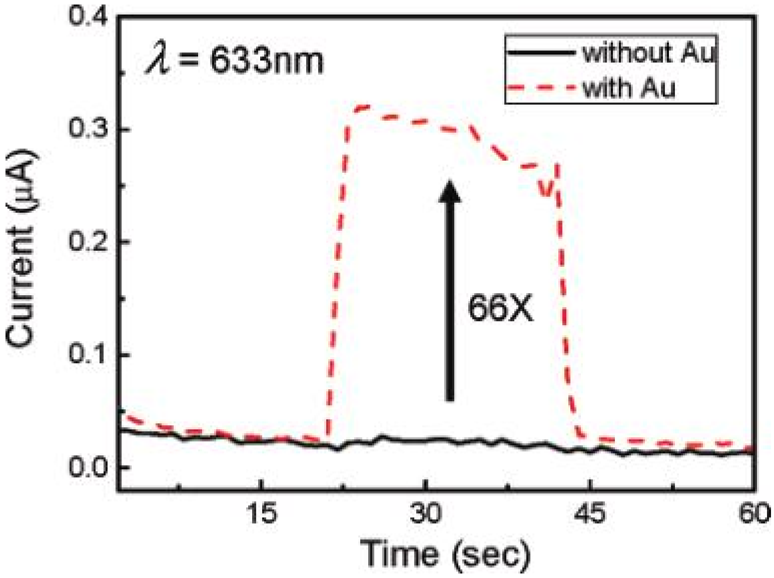

Figure 1-13. Photoinduced currents of $TiO_2$ photoanode with and without Au NPs illuminated by 633 nm light.

Due to the excellent electron transport capacity of the carbon material, it has a unique application in the photoelectric conversion and photoelectrochemical cracking water system. In the PEC water splitting system, the charge separation and transfer process play a key role in improving the utilization efficiency of the incident light and promoting the catalytic activity. In a composite of semiconductor and carbon materials, the carbon material first acts as a catalyst carrier, and the catalyst is fixed to its surface by chemical bond or physical forces between the two. Since the carbon material generally has a large specific surface area, the dispersion of the active ingredient improves the reactivity. Secondly, the heterogeneous structure between the carbon material and the semiconductor makes the photogenerated electrons easily transferred to the carbon material, reducing the recombination of electrons and holes, so as to improve the photoelectrocatalytic ability of the material. Zhang [43] et al. used carbon dots to surface-modify $TiO_2$ nanorod arrays to successfully fabricate CQDs/$TiO_2$ NT photoanodes. And the introduction of carbon dots not only broadens the optical absorption range of the material to the visible and near infrared regions, but also enhances the photogenerated charge carrier separation efficiency of the material. The experimental results show that the photocurrent density of the composite photoelectrode is 4 times of that of $TiO_2$ at 0 V vs. Ag/AgCl under simulated sunlight, and the hydrogen production rate is 14.1 μmol/h. At the same time, the composite electrode has good stability, and there is no obvious attenuation in the four cycles. Zhao [44] et al. combined $C_3N_4$ with a small amount of reduced graphene (RGO) by π-π stacking to effectively regulate the band structure of $C_3N_4$, resulting in the photocurrent density enhanced 3 times at 0.4V vs. Ag/AgCl.

**Surface loaded oxygen evolution or hydrogen evolution cocatalyst**. The performance of photoelectrocatalytic cracking water of the photoelectrode can also be improved by loading oxygen evolution or hydrogen evolution cocatalyst on the surface of the photoelectrode. For photoanode, in the electrode and the electrolyte contact interface, oxygen evolution reaction will generally occur. The photogenerated holes generated on the surface of the photoanode migrate to the contact interface while the water is oxidized to produce oxygen. Since the surface of the photoanode is likely to be oxidized, proper surface modification is required to catalyze the formation of oxygen, resulting in higher photocurrent and stronger stabilizing properties, whereas on the surface of the photoelectric anode load oxygen evolution cocatalyst is a good means of modification. Similar to the photoanode, the surface of the photocathode loaded by a layer of hydrogen evolution cocatalyst for surface modification can also greatly improve the performance of the PEC water splitting. Pt is often used as a hydrogen evolution promoter because of its good catalytic activity. The loading of oxygen or hydrogen evolution cocatalyst on the surface of the photoelectrode is an effective way for PEC water splitting of surface modified materials. [45-47]

### 1.3.4. Special nano morphology

The nano-morphology of a photoanode will influence the transfer formation of the photoinduced carriers. Morphology controlled photoanodes such as nanorods, nanotubes, and nanowires have attracted much attention, since the photogenerated charges transfer capacity, surface reaction active sites and photons absorption capacity of the photoanode can be improved [48].

### 1.3.5. Defects modification

In addition to the above metal doping, nonmetal doping, heterojunction construction, surface modification and construction of special morphologies, defect modification is one of the important methods to improve the water splitting performance of semiconductor materials. Different from the above modification methods, the defect modification usually does not need additional reagents. Besides, the preparation method of defect modification is simple and the cost is low.

There are many kinds of defect classification, according to the size of defects can be divided into point defects, line defects, surface defects and body defects. According to the causes of the problem can be divided into thermal defects, impurities and defects and non stoichiometric defects. To a certain extent, the material itself has defects, but the quantity of defects can be neglected within a certain range. Defects can greatly change the properties of materials, such as mechanical properties, electrical properties and optical properties. In the field of photoelectrochemical and photocatalytic solar energy conversion, the defects being studied are limited to oxygen vacancies and metal vacancies in point defects at present.

**Oxygen vacancies**. Oxygen vacancies in metal oxides have been widely studied by experimental characterizations and theoretical calculations [49]. The results show that oxygen vacancies can act as important active and dasoption sites for heterogeneous catalysis, thus affecting the reactivity of metal oxides [50]. In addition, the electronic structures [51], charge transfer properties [52], and surface properties are related to the oxygen vacancies during the photocatalytic reaction. However, the influence of oxygen vacancies on the performance of photoelectrochemical water splitting is twofold: on the one hand, the density of carriers increases with the increase of oxygen vacancies. On the other hand, these defects will evolve into composite centers, increasing the recombination rate of photogenerated carriers [53].

The oxygen vacancy between the valence band and the conduction band, and the impurity energy level will reduce the band gap of the semiconductor and increase the absorption range. For example, Wang etc. [50] found that the oxygen vacancies could reduce the band gap of ZnO and extended the light absorption range of ZnO to the visible region, enhanced the photocurrent density in visible light and degraded the chlorophenol under visible light. Ye etc. [54] obtained black BiOCl by irradiation the BiOCl 3 h by UV (lambda =365 nm) at Ar atmosphere, degradation mechanism of RhB under visible light irradiation was shown in Figure 1-14, the photogenerated electrons are excited state transition to oxygen vacancies, oxygen vacancies can be effectively for the trapping of photogenerated electrons, thus enabling more photogenerated holes and oxygen free radical reaction for the degradation of RhB.

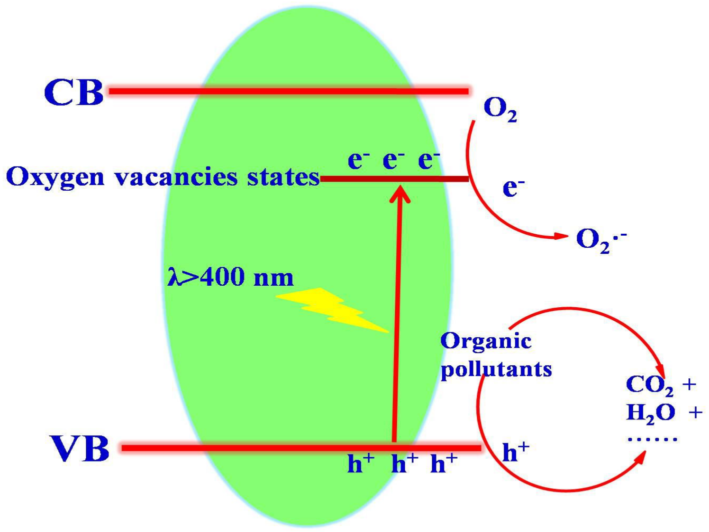

**Figure 1-14.** Band structure model and photoreaction process on black BiOCl.

Gan etc. [55] investigated the effects of different temperatures and atmosphere on the formation of oxygen vacancies in indium oxide ($In_2O_3$). The results show that the photoelectrochemical properties increase first and then decrease with the oxygen vacancies concentration. This is because oxygen vacancies can activate to the new energy levels, so that electrons transfer from the valence band to the conduction band, thus lowering the activation energy. However, the excess oxygen vacancies can capture photogenerated electrons and serve as the composite centers of photogenerated electrons and holes. Therefore, controlling the concentration of oxygen vacancies on the semiconductor surface is very important for improving the performance of photoelectrochemical water splitting.

**Metal vacancies**. Defect engineering is the key to the synthesis of metal oxides with high catalytic activity and the regulation of charge carrier types. Oxygen vacancies can increase the optical absorption and active sites of catalysts and semiconductors, and have been studied in depth. However, little research has been done on metal vacancies [56-57]. Pan etc. [58] introduced a large number of Zn vacancies in ZnO by a simple solvothermal method and subsequent annealing treatment, they found that Zn vacancy can convert n-type semiconductor into p-type semiconductor, resulting in higher photocatalytic activity.

## §1.4. Crystal defect on water splitting semiconductor photoelectrode

For a crystal semiconductor, defects are unavoidable. In a practical crystal, atoms do not fixed, but thermal motion ceaseless. In addition, influencing by some uncontrollable factors, such as formation condition, cold & hot processing, radiation and impurity, the arrangement of the atoms in a practical crystal is not so regulared and integrated, they usually deviate the idea structure. Thus, the irregularity and imperfection of the atoms arrangement in the crystal is called crystal defect.

For a crystal semiconductor, its inherent characteristics are influenced by the defects greatly, such as conductivity, permeability, plasticity and breaking strength etc. Furthermore, the local electron structure on the surface of semiconductor should be changed with the defects introducing in, so that more special catalysis centers can be formed on the surface of semiconductor crystal. Thus, defect is an important factor to influence the photocatalysis or PEC water splitting performance of a semiconductor photoelectrode.

### §1.4.1. Defects on the semiconductor

According to the geometry of the defects on semiconductor crystal, they can be defined as point defect, line defect and planar defect.

Point defect is the simplest one in that three species. It is the one defect that the lattice site or near micro area deviate the normal arrangement of the crystal, including vacancy, interstitial and impurity atom. Vacancy and interstitial are two main formations of point defect. If an atom possessing high enough vibrational energy, the energy can help the atom escape the bounding of the adjacent atoms, then jump away from the original site, left a blank point in the lattice, this blank point be called vacancy. Interstitial means that some atoms, which from the crystal-self or external, squeeze into the interstitial site of the lattice. The lattice distortion will be happened on vacancy or interstitial defect forming in the crystal, to change the energy structure of the adjacent electrons. However, the lattice distortion degree inducing by interstitial is much higher than that of vacancy.

Line defect contains various dislocations, including edged dislocation, screw dislocation and composite dislocation. The definition of dislocation is that in an integrated crystal, a part of crystal moves along a certain crystal facet and crystal orientation, inducing some kind of phenomenon with regular stagger.

The structure of edged dislocation is showed the Figure 1-14A. As shown in this figure, the upper part of the crystal is moved along the direction of applied stress, inducing an extra half plane of atoms on the upper part, The dislocation line of edge dislocation is the intersecting line, which produce by the extra half-plane of atoms intersecting with the glide facet.

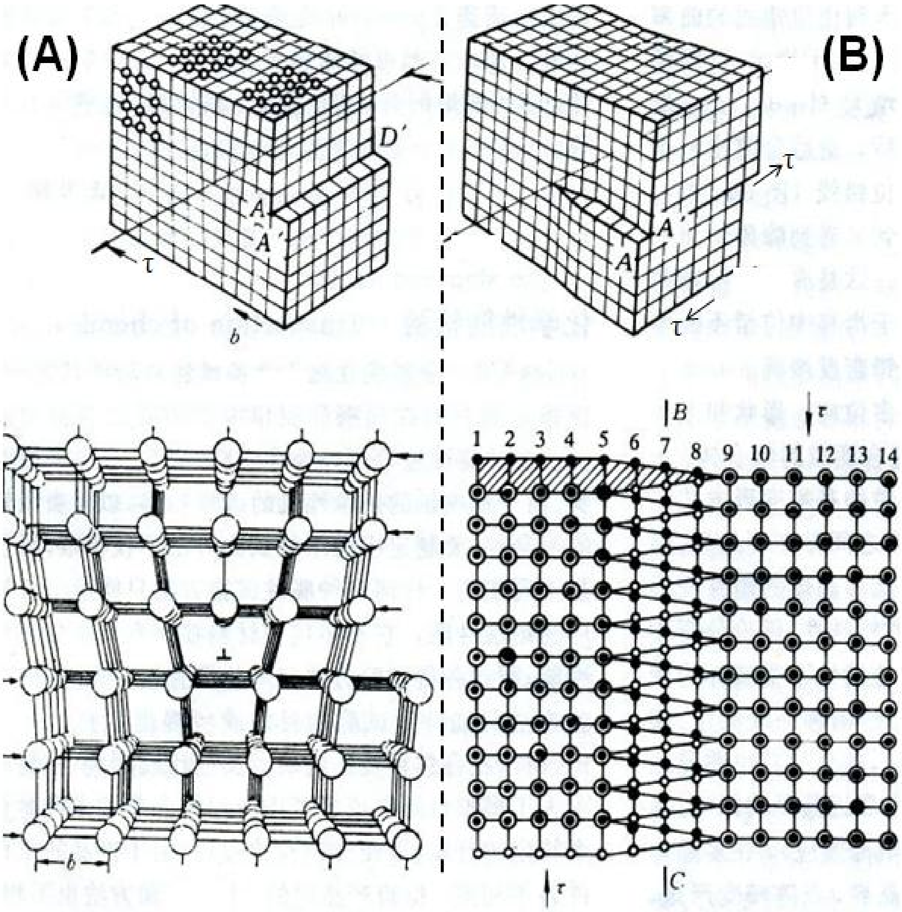

**Figure 1-14.** (A) edged dislocation, three-dimension structures (upper) and planar structure (below); (B) screw dislocation, three-dimension structures (upper) and planar structure (below).

Figure 1-14B presents three-dimension and planar structures of screw dislocation. At the right side, if the upper part and below part slipping to opposite direction at the opposite applied stresses, As shown in Figure 1-14B (below), a transition area with several atoms width can be accepted. In this transition area, the atoms are arranged by a screw situation, so this dislocation has been called as screw dislocation.

Except above two essential dislocations, the last one is composite dislocation. It mixes with the edged dislocation and screw dislocation, meaning that its sliding vector neither parallel nor vertical to the dislocation line, but intersect to the dislocation line with any angle.

The third type of defect is planar defect. Usually, the region of interface include several atoms thickness. In this region, the atom arrangement and chemical composition are often different with the one in the bulk crystal, and because of the distribution in 2-dimention, this region has been called planar defect.[59]

### §1.4.2. Influence of the PEC or photocatalytic performances by semiconductor defects

Up to now, in the three species of defects, only point defect, especial vacancy, has been employed to improve the PEC or photocatalytic performances of the semiconductors. There are three main functions of the vacancy modify method.

The band gap of the semiconductor can be narrowed by the vacancy modification. The photo absorption range of semiconductor can be enlarged to all visible region even near-infrared light by introducing a mass of vacancies on the surface of the semiconductor crystal. Chen et al. prepared black $TiO_2$ by ammonolysis reaction. This method could induce lattice distortion on the surface of $TiO_2$, where introducing large of oxygen vacancies, so that could broaden the light absorption range to 1300 nm. [60] Naldoni etc. [61] employed hydrogen reduction method to treat the P25 $TiO_2$ nanoparticle under 500 °C. And after this treatment, the band gap width of the $TiO_2$ decrease from 3.2 eV to 1.85 eV. This phenomenon attributed to the unique crystalline and defective core/disordered shell morphology of the black $TiO_2$. [61] The band gap width of BiOCl has also been narrowed by oxygen vacancy modification. Ye etc. [62] prepared black BiOCl by introducing oxygen vacancy in the crystal. Oxygen vacancy could produce impurity state inserting under the CB, in order to narrow the band gap width. Cui et al. [63] fabricated black $TiO_2$ nanotube photocatalyst. In the crystal, the $Ti^{3+}$ content is much higher than that of pure $TiO_2$, indicating high vacancy concentration. Further photocatalysis water splitting test found that the photocatalysis activity of vacancy modified $TiO_2$ was 5 times higher than that of pure $TiO_2$.

### §1.4.3. Improving the separation and transfer capacity of the photogenerated electrons and holes by defects

The photogenerated carriers can be captured by the impurity states to enhance its separation rate. For instance, introducing oxygen vacancy on the surface of $TiO_2$ can inhibit the recombination of the photogenerated electrons and holes. Kong et al. [64] found that the oxygen vacancy on the surface of $TiO_2$ can improve the photogenerated charge separation efficiency, because of the shallow energy level. However, the oxygen vacancy in the bulk of the crystal would transform into recombination centers to quench the photogenerated carriers, so that the photocatalysis or PEC performance of the semiconductor would be decreased. Expect $TiO_2$, the photocatalytic organic degradation performance of BiOCl could be improved after oxygen vacancy modification. There are two advantages of the oxygen vacancy on the surface of BiOCl. For the one, Oxygen vacancy could provide adsorption sites for the dye to enhance the catalytic reaction active area. For the other one, the shallow impurity energy level producing by oxygen vacancy could served as carriers capture center, thus could promote the separation capacity of the photogenerated charges. [65-67]

### §1.4.4. Increasing surface active reaction sites

Surface redox reaction is one of the key process for PEC or photocatalysis water splitting. If the surface redox reaction cannot process smoothly, then the un-reacted photogenerated electrons and holes will recombine and transform to heat or fluorescence. Thus, it is very important to decrease the surface redox reaction energy barrier during the PEC or photocatalytic process.

Some research found that the photocatalytic or PEC redox reaction energy barriers can be reduced by introducing oxygen vacancy. During PEC or photocatalytic water splitting process, the oxygen evolution half-reaction include a four electrons transfer, so that it is very complex. During water splitting, the oxygen evolution reaction is much harder than the hydrogen evolution reaction, because the former reaction shows a much higher reaction energy barrier than the latter one. Bikondoa et al. [68] used STM to observe the (110) facet of rutile $TiO_2$, and found that the water was reaction on the site of bridge oxygen vacancy, then transformed to ·OH radical. It is indicated that the surface oxygen vacancy can decrease the energy barrier of the oxygen evolution reaction. Selloni etc. employed First Principle Calculation method to research the water oxidation reaction on anatase $TiO_2$ (101), and found that the water molecular just can be decomposed under the condition of oxygen vacancy existing on (101) facet. [69] Furthermore, they found that only surface oxygen vacancy and Ti interstitial defects can improve the photocatalytic performance of the $TiO_2$, but the bulk oxygen vacancy would induced second recombination of the photogenerated carriers. [70, 71]

Oxygen vacancy which in the bulk of semiconductor cannot improve the performance of photocatalysis or PEC water splitting, because the bulk oxygen vacancy only can provide an indirect effect for the surface photocatalysis reaction. However, for the 2-dimention nanosheet, the oxygen vacancy just can appear on the surface or near surface of the semiconductor, so that can increase the active site of photocatalyst to improve the photocatalytic performance of it. Xie etc. [72] prepared ultrathin 2-D $CoSe_2$ nanosheet with Co vacancies on. These Co vacancies could provide active sites for photocatalysis process and decrease the energy barrier of the oxygen evolution reaction. Except PEC or photocatalytic water splitting, oxygen vacancy on the BiOBr 2-D nanosheet could improve the performance of photocatalytic nitrogen fixation. These oxygen vacancy could absorb and active the $N_2$, that transform the $N_2$ to $NH_3$. So, oxygen vacancy plays an important role in the photocatalysis process. [73]

## §1.5. Research Progress of $BiVO_4$ Photoanode

$BiVO_4$ belongs to the triad group of bismuth oxide and has a variety of forms, mainly divided into quartet scheelite phase (s-t phase), monoclinic tungsten ore phase (m phase) and tetragonal zircon phase (z-t phase). It is reported that the zircon phase is formed during the low temperature synthesis process (eg. precipitation at room temperature) and the s-t phase is required to be prepared at high temperature. Under these conditions, the three kinds of crystal structures can be transformed into each other. At 397 ~ 497°C, the tetragonal zircon phase to the monoclinic chlocomite phase can be irreversibly converted. At 255°C, A reversible change occurs between the tetragonal tungsten phase and monoclinic tungsten phase [74].

$BiVO_4$ is an n-type semiconductor photocatalyst. The results show that the band gap of $BiVO_4$ (z-t) is about 2.9 eV, which is mainly in the ultraviolet region. And the bandgap width of m-$BiVO_4$ and $BiVO_4$ (s-t) were 2.41 eV and 2.34 eV, respectively, and exhibited higher photocatalytic activity under visible light irradiation ($\lambda$> 420 nm). $BiVO_4$, as a new type of semiconductor catalyst with visible light response, has a relatively narrow bandgap (2.4 eV), is environmentally friendly and can be reused for good stability. It can use 43 % of the solar light in the 400~700 nm visible light part of the energy, so it draws considerable attention of researchers [75].

### §1.5.1. Nano-morphology $BiVO_4$ photoanode

Since Kudo et al. [76] used bismuth vanadate as a photocatalyst for the first time to use solar energy, water oxidation and suspended photocatalytic degradation of organic matter were studied on this basis [77, 78]. However, with the deepening of $BiVO_4$ research, research in the field of environment has gradually focused on the development and optimization of photoanographic materials in photoelectrochemical cells.

**Porous bismuth vanadate material.** At present, $BiVO_4$ photocatalytic anodes are often prepared using organometallic decomposition. Specifically, the organometallic substance containing $Bi^{3+}$ and $V^{3+}$ or $V^{5+}$ is dissolved and deposited on the conductive substrate by spin coating or spray pyrolysis, and the substrate with the organometallic precursor solution is decomposed and crystallized at a high temperature of 350 to 500 °C. The $BiVO_4$ photoprocesson was prepared by spin coating for the first time in 2003[79]. Since then, the reports about the preparation and improvement of $BiVO_4$ photocathodes by spin coating have been reported more and more, and the combination of electrode materials is optimized by adding ions in precursor solution.

Chemical bath deposition method (CBD) refers to the surface activation of the substrate immersed in the deposition solution, at atmospheric pressure, low temperature (generally 30~90 °C) by controlling the reaction of complex and chemical reaction, on the substrate preparation of high yield and good quality film for deposition thin films. This method does not require external electric field or other energy, cheap. Lou et al. [80] prepared $BiVO_4$ thin films by chemical bath deposition. $BiVO_4$ films were deposited at different temperatures in $BiNO_3$, EDTA and $NaVO_3$ phosphate buffered solutions. The effects of deposition time, temperature, pH of solution and buffer solution on the morphology of samples were studied. When the temperature and the pH of the sediment are high, the microcrystalline polyhedron of the $BiVO_4$ film can expose fewer planes to form a more compact film.

Ye et al. [81] have shown that it is easy to quickly and automatively prepare $BiVO_4$ thin film materials. It is proved that they can prepare $BiVO_4$ films containing various dopants by means of a simple drop casting method using computer and scanning electrochemical microscopy. This method can be used to prepare the $BiVO_4$ thin film electrode material in a large scale by using intelligent ratio, efficient mixing and rapid screening.

$BiVO_4$ photocatalytic materials can also be prepared by electrochemical synthesis method. Comparing with the conventional chemical method, it has a high purity product, less environmental pollution and other advantages, furthermore it is a highly selective synthesis method. However, this method has the problems of low reactor production intensity and complicated process conditions. Seabiod et al. [82] used a plating solution containing $Bi^{3+}$ and $V^{4+}$ under certain bias, $V^{4+}$ was oxidized to $V^{5+}$ and reacted instantaneously with $Bi^{3+}$ to form an amorphous Bi-V-O phase film with Bi: V of 2: 3.

**Nanosheets**. The morphological structure of $BiVO_4$, such as particle shape and porosity, has a great influence on the thermodynamics, kinetics and charge transport properties of the photo-anode interface. Therefore, understanding and controlling the morphology and improving the specific surface area of the material are an effective way to improve the photocatalytic activity of $BiVO_4$. Madooudand et al. [83] first prepared a highly biodegradable reactivity (001) surface by a urea-assisted hydrothermal method for the layered $BiVO_4/Bi_2O_2CO_3$ nanocomposites. The urea concentration and the relevant reaction time play a key role in determining $BiVO_4$ morphology, crystallinity and crystallite size. The higher the urea concentration is, the larger the BET specific surface area is, and the larger the pore volume and the average pore size are. The prepared nanocomposites exhibit enhanced photocatalytic activity of RhB degradation under visible light irradiation compared with $BiVO_4$ and $Bi_2O_2CO_3$ nanosheets.

**Nanorods**. Wang et al. [84] successfully prepared a m-$BiVO_4$ nanorod with a rectangular cross section by adjusting the synthetic parameters, which has a good degradation effect on rhodamine B. Eda et al. [85] Monovalite $BiVO_4$ nanorods prepared by soft template method have higher activity for the degradation of $Cu(AC)_2$ under visible light irradiation. This study shows that the high local symmetry of $VO_4$ tetrahedra and the large surface area and high crystallinity are the key factors that have stronger visible light activity for $BiVO_4$ nanorods. Zhao et al. [86] prepared porous $BiVO_4$ with monoclinic crystal structure and olive-like morphology by dodecylamine-assisted alcohol hot-hydrothermal and dipping. Surface area can reach 8.8-9.2 $m^2/g$, band gap can be 2.38-2.41 eV.

**Nanometer hollow ball**. Zhu et al. [87] made the hollow microspheres $BiVO_4$ composed of hundreds of nanorods by microwave hydrothermal synthesis with EDTA, and the visible light activity of the controllable olivine and hollow microspheres of $BiVO_4$ enhanced. The resulting hollow microspheres are constructed from a combination of rods having a length between 0.3 and 1 mm and a diameter of about 80-150 nm.

### §1.5.2. Doped $BiVO_4$ photoanode

To introduce some impurity atoms or materials, which can increase light anode carrier diffusion length of $BiVO_4$, prolong the service life of $BiVO_4$ thin film photoanode of photogenerated electrons and holes. But sometimes there are also interfere with the charge transfer and doping reduced the depletion layer width and other defects, therefore, determining the suitable and appropriate doping concentration to improve the photocatalytic activity of common is crucial. It is common such as rare earth elements, transition elements and elements such as carbon doped system.

**Doping of metal elements**. In order to determine the effective dopant, Xu et al. [88] incorporated rare earth elements such as holmium, samarium, ytterbium, europium, gadolinium, neodymium, cerium and lanthanum in $BiVO_4$. Experiments show that the rare earth elements are in the form of oxides in $BiVO_4$ samples, and $Gd^{3+}$ due to the special characteristics of the electronic structure, the doped $BiVO_4$ has the best photocatalytic performance, and its optimum doping amount is 8%. Wang et al. [89] successfully prepared La-B-$BiVO_4$ catalyst by sol-gel method using citric acid as chelate. It was found that lanthanum (III) ions and boron elements were successfully doped into the $BiVO_4$ crystal lattice. La and B co-doped $BiVO_4$ photocatalysts show more surface oxygen vacancies, larger surface area, smaller particle size, narrower band gap that makes the sample has a strong light absorption in the visible area, and have a higher degradation rate on the methyl orange in the visible light. The interaction between LA and B can effectively promote the separation of photogenerated electrons and holes.

Zhang et al. [90] successfully doped metal Ag particles with a size of 10-20 nm on $BiVO_4$ film by photoreduction.The degradation ability of Ag-doped $BiVO_4$ film under visible light was greatly improved, and the degradation rate under visible light after 4 h of the $BiVO_4$ film respectively was 94.1 % to phenol and 61.0 % to TOC. In recent years, doping system of transition metals W and Mo have attracted much attention. Ye et al. [91] found that the carrier density of the doping system increased by nearly 2 times and the photocatalytic activity was significantly improved when Bi/V/W was 4/5/1. Luo et al. [91] also found that the samples showed the best current efficiency and quantum efficiency when the Mo content was about 3%.

**Non-metallic element doping**. Lee et al. [92] prepared C-$BiVO_4$ by impregnation and they found that the photocatalytic activity was highest when the carbon doping amount was 5 wt%. With the increase of carbon content, the surface area of $BiVO_4$ composite powder increased gradually. Carbon-loaded $BiVO_4$ improved in photocatalytic activity due to increased number of surface active sites and enhanced light absorption capacity. Wang et al. [93] prepared N-$BiVO_4$ by using sol-gel method wih using citric acid as a chelating agent and hexamethylene tetramine as a nitrogen source. The results showed that when the N-doping amount was 2 wt%, the samples had strongest activity. Doped excess N reduces the light absorption. The nitrogen atom is doped into the $BiVO_4$ lattice replaced the oxygen atom sites to form the O-Bi-N-V-O bond, which contributes to the formation of more reactive $V^{4+}$ and oxygen vacancies. Zhang et al. [94] prepared a Si-$BiVO_4$ thin film by modified organo metallic decomposition. The results showed that the degradation ability of phenol was improved, which because of the decrease of grain size and the enhancement of hydrophilicity.

### §1.5.3. $BiVO_4$ based composite photoanode

The composite structure or heterojunction can effectively improve the photon absorption of the anode, promote the separation of electrons and holes and enhance the efficiency of charge transfer. It is an important measure to optimize the performance of $BiVO_4$ anode.

**Heterojunction thin film system**. Chatchai et al. [95] fabricated $WO_3/BiVO_4$ heterojunction electrodes on FTO by spin coating and noted that their current efficiency was 10 times higher than that of pure $BiVO_4$ electrodes in 0.5M $NaSO_4$ solution. Recently $BiVO_4$ couplied with Cu oxide composite electrode has a better performance [96, 97]. Zhao et al. [96] synthesized $CuO/BiVO_4$ composites by hydrothermal method and found that the degradation rate of methylene blue was nearly 5 times higher. WQian et al. [98] proved that the formation of an amorphous $FeO_x$ layer on the $BiVO_4$ anode can significantly improve the photoactivity of its water oxidation reaction. $BiVO_4/FeO_x$ photoelectric anode electrode at 1.23V vs. RHE potential can produce a photocurrent near 2.52 $mA/cm^2$, which is 3 times by the initial photoelectrochemical properties. The increase in photoelectric properties is due to the improvement in conductivity and in surface catalytic kinetics, which is because the formation of Fe II sites. The addition of amorphous iron oxide in $BiVO_4$ reduced the charge accumulation and reduced the recombination rate, this as shown in Figure 1-15.

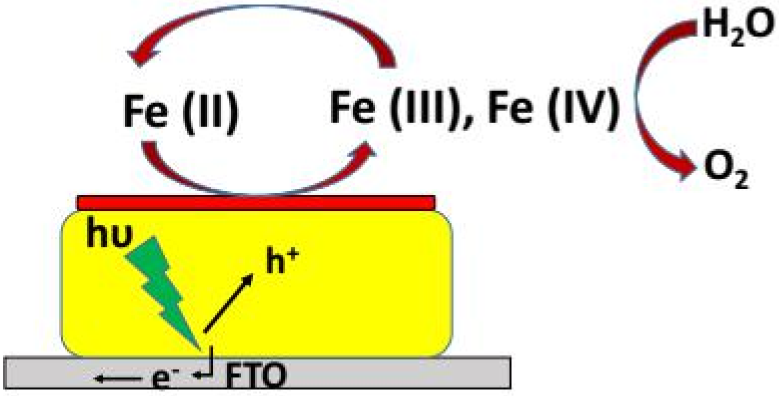

**Figure 1-15**. Mechanism of charge spearation for the $BiVO_4/FeO_x$ heterojunction.

**Metals-$BiVO_4$ composite system**. There are many methods to modify photocatalyst, and one of the common methods is the deposition of noble metals in the surface of the catalyst. The deposition of noble metals can effectively change the carrier distribution on the surface of a semiconductor material, which because the work function of most noble metals is higher than that of the semiconductor, that means that the Fermi level of the noble metals and the semiconductors is not the same. When the noble metal was modified on the semiconductor surface and came into direct contact with the semiconductor, the redistribution of the carriers on the semiconductor material surface is caused. At this point, the electrons on the semiconductor with a relatively high Fermi level are transferred to noble metal surface with the relatively low Fermi leve until the Fermi level of the semiconductor and the noble metal reaches equilibrium. That eventually forms a barrier at the two semiconductor interfaces base. The barrier can not only effectively capture the photogenerated electrons, but also can inhibit the rapid recombination of electrons and holes to extend their life, thereby improving the photocatalytic efficiency.

**Cocatalyst-$BiVO_4$ composite system**. In order to reduce the photodissociation between the anode and the electrolyte interface, enhance the visible light response and improve the photocurrent intensity, the $BiVO_4$ photoelectrode is often supported some of the oxygen evolution catalysts (OECs), such as Co-Pi catalysts [99] and FeO [100]. The cocatalyst plays an important role in promoting the catalytic reaction of the semiconductor photocatalyst. In particular, the double promoter (the oxidation and reduction promoter) is deposited onto the semiconductor photocatalyst to improve its photocatalytic activity due to the synergistic effect of the rapid consumption of photogene rated electrons and holes. Based on the photo-generated electrons and holes can separated to $BiVO_4$ different crystal face, Li et al [101] successfully prepared in the deposition of {010} and {110} on the reduction of cocatalyst and oxidation promoter ($M/MnO_2/BiVO_4$ and $M/Co_3O_4/BiVO_4$, where M represents a noble metal), as shown in Figure 1-16. The photocatalytic performance of $BiVO_4$ is improved due to the inherent properties of charge separation and the synergetic effect of double promoter.

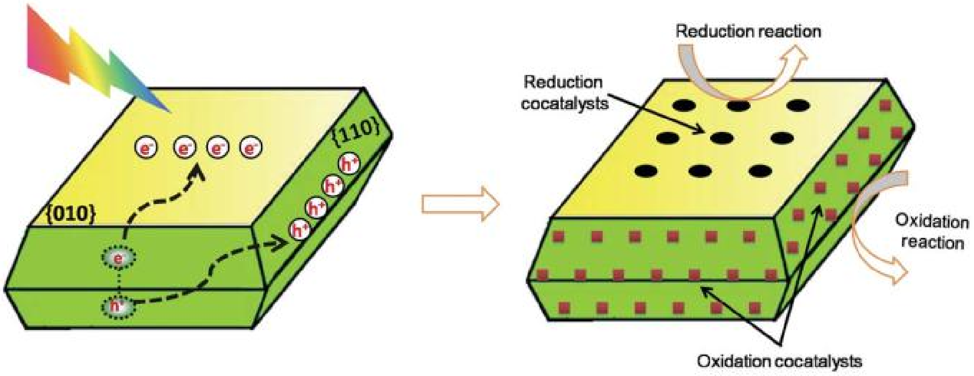

**Figure 1-16**. Selective deposition of reduction and oxidation cocatalysts on {010} and {110} facets of $BiVO_4$.

**Carbon material-$BiVO_4$ system**. Graphene, carbon nanotubes and other carbon nanomaterials are widely used in electronic components, photoelectric catalytic equipment, and so on. The coupling of reduced graphene (RGO) and carbon nanotubes can improve the charge transfer rate of $BiVO_4$ photocathodes. Ng et al.[102] oxidized graphene (GO) by mixing $BiNO_3$, $V_2O_5$ and graphene in a nitric acid solution, suspending the mixture in an ethanol solution and irradiating it, and the photo-generated electrons excited by $BiVO_4$ into RGO, and finally form RGO-$BiVO_4$ composite electrode on FTO. This composite material is a good receptor for photogenerated electrons, effectively suppressing the recombination of electron/hole pairs, improving the photocurrent density and photocatalytic performance of the electrodes, as shown in Figure 1-17.

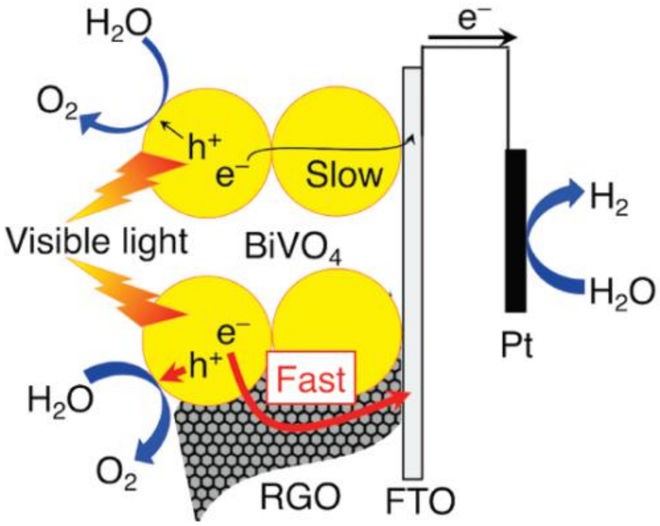

**Figure 1-17**. Reduced graphene oxide(RGO) promotes electron migration from $BiVO_4$ to FTO

# §1.6. Progress of the $WO_3$ photoanode

## §1.6.1. Nanostructure of $WO_3$ photoanode

$WO_3$ is composed of perovskite monomer, which is one of the most attractive oxides in photocatalysis and photoelectrocatalysis. Compared with a-$Fe_2O_3$, its absorption of the solar spectrum ($E_g$=1.5-1.8 eV) is about 12%, with a suitable hole diffusion length (ca. 150 nm). Compared with $TiO_2$ (0.3 $cm^2V^{-1}S^{-1}$), it has a better electron transport efficiency (ca. 12 $cm^2$ $V^{-1}$ $S^{-1}$).

From the stoichiometric aspect, the pure tungsten trioxide is a colorless transparent insulator and has no any impurity, as ideal tungsten trioxide ($WO_3$). As shown in Figure 1-18, its crystal structure is $ReO_3$, as that the unit cell structure is octahedron composed with a tungsten atom as the center, and six oxygen atoms. In addition, $WO_3$ is a superior electrode material, with photochromism (electrochromism), gas sensitivity and absorption et al. It has a wide range of applications in various research areas.

Tungsten trioxide is an ideal semiconductor material with photoactivity. It can not only absorb the sunlight, but also cheap and easy to get. The synthesis method is gentle and diverse. In recent years, the synthesis of different nano $WO_3$ gradually attractted people's attention. At present, many different morphologies of nano $WO_3$ have been successfully synthesized.

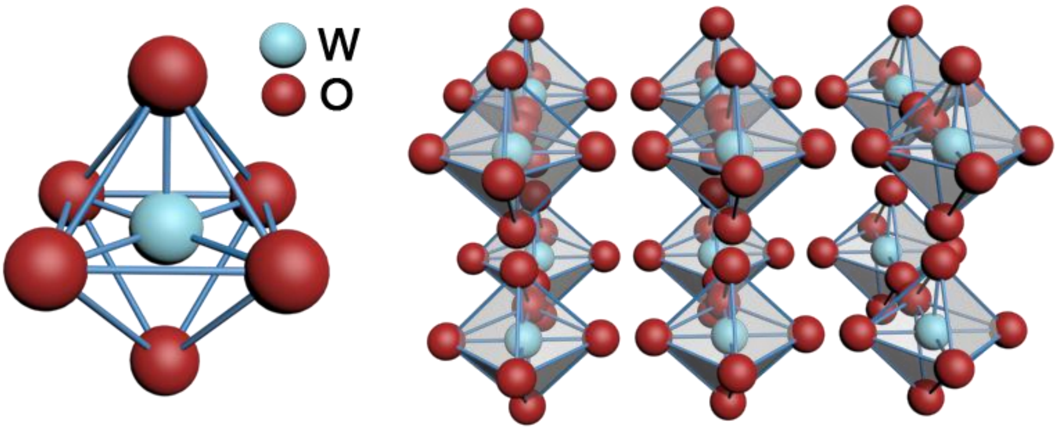

**Figure 1-18**. The crystal structure of $WO_3$

**Mesoporous $WO_3$**. Nanostructured porous films are made of the nanostructures on a specific substrate, or directly constructed a nanostructure with a special structure on the substrate. The nanostructured porous film greatly expands the application areas of nanomaterials, which can provide new components for the devices designed with special optical, electrical and catalytic properties. Compared with the powder material, it has more application values. Porous nanomaterial electrode has a two-dimensional or three-dimensional porous network structure, which can scatter and absorb much more incident light. It has a high specific surface area, which can improve the contact area of the material and electrolyte solution and increase the rate of electron transport; Porous structure also provides more active sites, which increases the photogenerated electron-hole separation efficiency.

Yang et al. [103] prepared the $WO_3$ nanoporous material with a high porosity using electrodeposition method by controlling the pH, and its photoelectrocatalytic properties became better than relatively low porosity films. Chen et al. [104] prepared the $WO_3$ porous films with ordered porous network structure taking the PS ball as template. Compared with the photoelectric properties of the unorder porous and non-porous $WO_3$, it was found that the ordered porous structure affected the photoelectrochemical properties as an important factor.

**$WO_3$ nanosheet**. Nanosheet is one of two-dimensional (2D) nanostructures with different thicknesses and it has many special potential applications in electricity, optics, photochemistry, sensor and ion exchange properties. Compared to the researches of zero-dimensional and one-dimensional (1D) nanostructure, the 2D nanostructure has been neglected over the past decade. An important reason is that the synthesis of single crystal 2D nanostructure is more difficult to control. However, a great deal of progress has recently been made in the syntheses of $TiO_2$, ZnO, $Mn_3O_4$, CoO, $Ga_2O_3$ and composite hydroxide nanosheet.

Waller et al. [105] prepared $WO_3$ nanosheets with single crystal structure by stripping $Bi_2W_2O_9$. Under light conditions of more than 250 nm, it had good performance for photocatalyic water oxidation. The oxygen production rates in UV and visible light were 69.7 $mol \cdot h^{-1}$ and 35.5 $mol \cdot h^{-1}$ respectively. Pollenux et al. [106] successfully synthesized tungsten oxide hydrate ($WO_3 \cdot H_2O$) nanosheets by heating tungsten chloride ($WCl_6$) -benzyl alcohol system. $WO_3 \cdot H_2O$ has poor thermal stability, because it can decompose and release water molecules at higher temperature. The anhydrous $WO_3$ would become more stable in practical applications. Choi et al. [107] reported a similar $WCl_6$ system that the synthesis of $WO_3$ nanosheets were in ethanol.

**$WO_3$ nanorod**. Compared to the polycrystal structure and difficulty of collecting of the $WO_3$ nanomaterials, the ordered single crystal $WO_3$ nanorods prepared on the solid substrate are not only recyclable, but there also is no grown monocrystal in crystal boundary, which is conducive to the rapid transmission of photogenerated carriers, and reduce the probability of the photogenerated electron-hole recombination. At the same time, the $WO_3$ nanorod has a larger specific surface area and strong adsorption capacity, which can greatly improve the photocatalytic efficiency, so the synthesis of ordered nanorods has become a hot spot in recent years in the field of photocatalysis. It is worth mentioning that the prepared $WO_3$ nanorods are firmly grown on a variety of substrates without additional load immobilization. It can be easily applied to photocatalytic degradation of organic contaminants, and the transparent substrate can also make better use of light. Bai et al. [108] carried out a new hydrothermal synthesis method of $WO_3$ nanorods at 100 °C without using special equipment and toxic reagents, which may be particularly beneficial in reducing the cost of practical applications. By adjusting the amount of oxalic acid and controlling the amounts of $WO_4^{2-}$ and $H^+$, it is ensured that small and uniform crystal seeds are formed in strong acid solutions. By hydrothermal method, using $Na_2WO_4 \cdot 2H_2O$ as raw material and NaCl as additive, Zheng et al. [109] prepared directly ordered $WO_3$ nanorod arrays on indium tin oxide transparent conductive substrate. As the results shown, the single $WO_3$ nanorods have the structure of hexagonal single crystal. With the increase of the pH value of the precursor fluid, the $WO_3$ nanorod bundles parallel to the substrate were gradually transformed into nanorod arrays grown perpendicular to the substrate.

**$WO_3$ nanoflower**. As shown in Figure 1-19, Yu et al.[110] prepared layered tungsten trioxide with large scale by hydrothermal treatment using sodium tungstate in aqueous nitric acid solution. It has been found that the 3-D tungsten trioxide was composed of some 2-D layers, which was further composed of amounts of interconnected nanoplates with different sizes. The flower-like components has holes with specific levels, exhibiting a higher photocatalytic activity on visible light than the samples without layered porous structure. From results, it was confirmed that the layered tungsten trioxide was stable and not corroded by light.

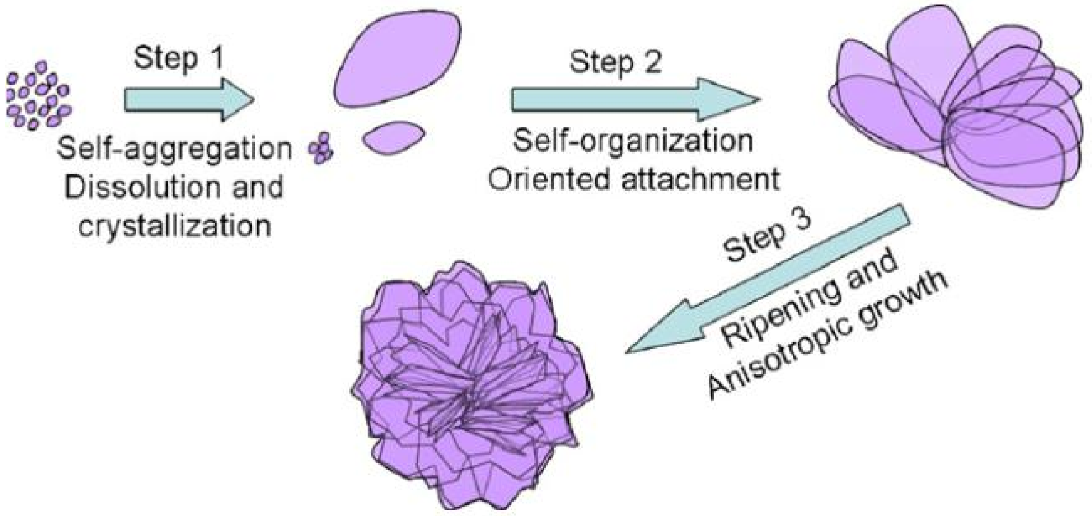

**Figure 1-19**. The synthesis of flower-like $WO_3$.

### §1.6.2 Doped $WO_3$ photoanode

**Metal element doped $WO_3$ photoanode**. When metal element is doped into semiconductor photoanode, the level doping element is located in the semiconductor bandgap, the following reaction occurs: On the one hand, doped element can reduce the recombination of photogenerated electrons as a trap and improve the efficiency of semiconductor anode conversion efficiency. On the other hand, it can absorb photons with low energy, expand the energy absorption edge and improve the photoelectric properties. But excessive doping would reduce the average distance between the traps, resulting in an increase in the probability of combination of photogenerated electron-hole pairs. Metal element doping not only increases the light absorption by changing the band gap of the semiconductor, but also increases the initial potential by changing the positions of valence band and conduction band of the semiconductor. At present, most of studies for doping the metal element mainly focus on doping transition metal element. Transition metal elements have many different valence states, so a certain amount of transition metal elements can produce low traps on the semiconductor photoelectrode doping, which contributes to the separation of photogenerated electron-hole pairs, and effectively improve the the conversion efficiency of photoelectrochemical water decomposition, but excessive doping produces more low traps, which contributes to the photogenerated electron-hole pairs. Du et al. [111] prepared $WO_3$ materials doped with different amounts of cerium by the solid-state sintering, and the doping moderate amount of cerium can enhance the fluorescence intensity of the samples. Under the visible light irradiation, the water photocatalytic decomposition was carried out. The catalytic activity of $WO_3$ catalyst doped with 0.05 wt% cerium at 600 ° C was the highest, and the oxygen evolution rate of the catalyst improved 1.5 ~ 1.7 times. Xiang et al. [112] prepared $WO_3$ by ion exchange method. The performance of photocatalytic degradation of rhodamine was greatly improved after doping $WO_3$ with Au.

**Nonmetal element doped $WO_3$ photoanode**. Nonmetal element doped semiconductor crystal is that nonmetal element is doped into the semiconductor crystal, which changes the original band structure of the semiconductor photoelectrode, resulting in a decrease in the band width of the semiconductor photoelectrode. Doping nonmetal element ocurrs orbital hybridization with the orbit of semiconductor, which produces a new band structure, optimizing the photoelectrochemical hydrolysis after doping. The general quantum conversion efficiency is higher than that of metal element. Semiconductor photoelectrode with wide bandgap is doped with metal element, which can effectively reduce the band width, resulting a red shift in light absorption band edge, thereby expanding the absorption range of visible light.

N-doping can effectively improve the photoelectrochemical properties of $WO_3$. Paluselli et al. [113] confirmed that the N atom was substituted for the O atom, and the $WO_3$ band gap became narrowed due to the hybridization of the N 2p orbit and the O 2p orbit. Cole et al. [114] prepared $WO_3$ films on glass substrates by magnetron sputtering, adjusting doping amounts of N by controlling different $N_2$ partial pressures. N doping resulted in a decrease in bandgap width of $WO_3$. With the increase of the partial pressure concentration, the photoelectric performance of the $WO_3$ decreased. It was concluded that the N-doping reduced the crystallinity of $WO_3$, increased the crystal boundary and the defect, and decreased the electron transport performance of $WO_3$, resulting the photoelectric performance of the materials.

C doping is also an effective method to improve the photoelectric response of semiconductor materials. Ding et al. [115] prepared C-doped $WO_3$ by immersing degreased cotton as a template in $WO_3$ sol. As the results shown, C doping not only reduced the forbidden band width of $WO_3$ to 2.12 eV, but also introduced new states, reducing the energy of transiting the electrons from the valence band to the conduction band.

### §1.6.3. $WO_3$ composite photoanode

**$WO_3$ based heterojunction system**. A lot of research results present, the band of two different semiconductors matched in energy band coupled together, would form a heterojunction. On both sides of the heterojunction band, due to their different characteristics such as energy band, can form space potential. Using the complementarity of energy level structures of two kinds of semiconductors promote the rapid transfer of the photogenerated carriers; moreover, What photogenerated electrons from one semiconductor inject into another semiconductor can effectively block the composite pathway of electrons and holes, inhibit the recombination of photogenerated carriers and improve quantum efficiency, improving photocatalytic efficiency [116].

**Metal-$WO_3$ shottky heterojunction system**. Recombination of photogenerated carrier is the main factor affecting the performance of semiconductor materials, and reducing the recombination probability of photogenerated carrier is an effective way to improve the photoelectric properties of semiconductor materials. The research found that there is a Schottky barrier the metal particles loaded on the semiconductor and the semiconductor, which can effectively reduce the recombination of the electrons and holes, improving the photoelectric properties of semiconductor effectively. However, what coated with excessive metal or too large particles of accelerates recombination of electrons and holes, reducing the performance of semiconductor. Therefore, choosing the metal particles whose conductivity and particle size matched with semiconductor materials is an important direction to realize development of loading metal on semiconductor material.

Solarska [117] prepared nano $WO_3$ layer doped with Ag on the surface of FTO by magnetron sputtering method, and porous $WO_3$ films were prepared using tungstic acid/polyethylene glycol precursor by sol-gel method. Compared with the current density of pure $WO_3$ porous film, the current density of Ag/$WO_3$ photoanode increased by 60 %, the photoelectric conversion efficiency increased by 50 %. Liu et al. [118] synthesized $WO_3$ nanofilms by hydrothermal method doping with gadolinium (Gd). Mott–Schottky results demostrated that the CB and VB potentials of $WO_3$ were shifted to more negative values. Photoinduced I-V curves indicated that the photocurrent density increased by 153 % after Gd doping.

**Surface cocatalyst-$WO_3$ system**. The PEC performance of photoanode can be improved by loading suitable co-catalysts to decrease the surface reaction energy barriers of it. As shown in Figure 1-20, the oxidation and reduction reactions can be facilitated by loading oxidation or reduction cocatalysts on semiconductors, because it can provide active sites, meanwhile, suppressing the charge recombination and reverse reactions.

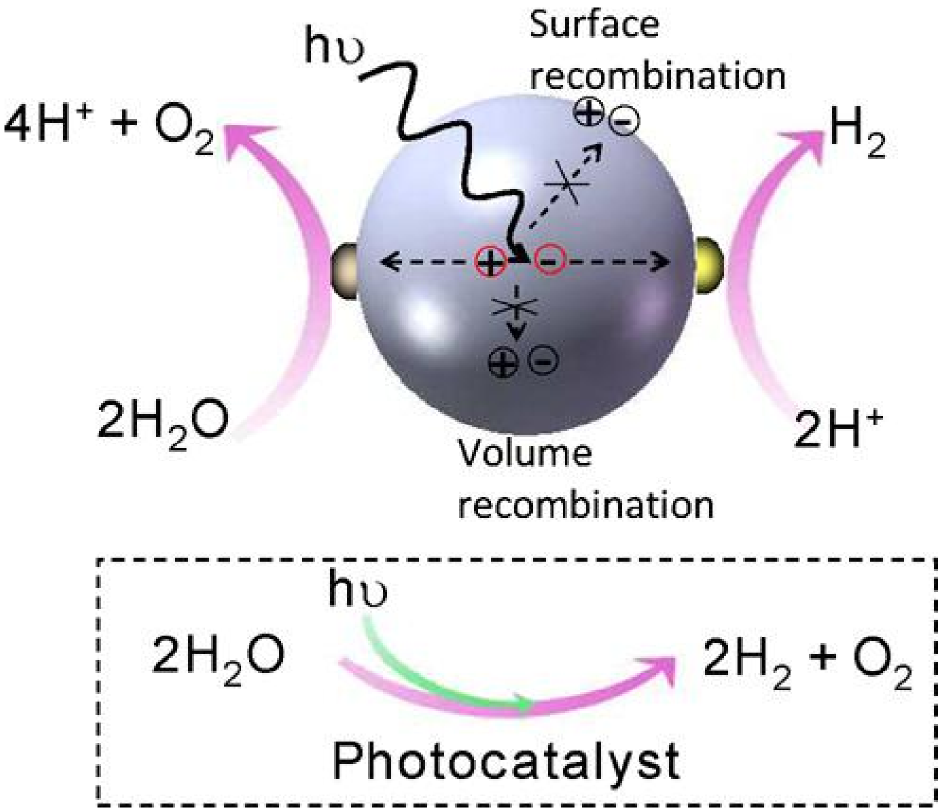

**Figure 1-20**. The reaction between the cocatalyst and semiconductor

He et al. [119] synthesized novel $WO_3$/g-$C_3N_4$/$Ni(OH)_x$ hybrids by a two-step strategy of high temperature calcination and in situ photodeposition. Their photocatalytic performance was investigated using TEOA as a hole scavenger under visible light irradiation. The loading of $WO_3$ and $Ni(OH)_x$ cocatalysts boosted the photocatalytic $H_2$ evolution efficiency of g-$C_3N_4$. $WO_3$/g-$C_3N_4$/$Ni(OH)_x$ with 20 wt% defective $WO_3$ and 4.8wt% $Ni(OH)_x$ showed the highest hydrogen production rate of 576 μmol/(g·h), which was 5.7, 10.8 and 230 times higher than those of g-$C_3N_4$/4.8 wt% $Ni(OH)_x$, 20wt% $WO_3$/g-$C_3N_4$ and g-$C_3N_4$ photocatalysts, respectively. The remarkably enhanced $H_2$ evolution performance was ascribed to the combination effects of the Z-scheme heterojunction ($WO_3$/g-$C_3N_4$) and loaded cocatalysts $Ni(OH)_x$, which effectively inhibited the recombination of the photoexcited electron-hole pairs of g-$C_3N_4$ and improved performance of $H_2$ evolution. Some other co-catalyst, such as Co-Pi, has been demonstrated an excellent co-catalyst for PEC water oxidation [120].

## §1.7. The motivation and outline of this research

Collecting and storing solar energy in chemical bonds, as plant accomplishes through photosynthesis, is a highly desirable approach to solving the question of energy shortage. The “Holy Grail” of solar energy conversion and storage is the PEC water splitting using semiconductors thin film photoelectrode, to transform solar energy in the simplest chemical energy, $H_2$.[121] As shown in Figure 1-21, efficiently splitting water into usable hydrogen could become a new industrial photosynthesis that would provide clean fuel and industrial raw material for $CO_2$ fixable. To accomplish this new photosynthesis, an economically viable, stable and high-efficiency water splitting cell needs to be developed. [122] PEC water splitting can also be achieved by photovoltaic modules omhic connected to independent catalytic electrodes system. Water splitting cells with direct semiconductor/liquid reduction interface are attractive because they avoid complex fabrication and systems costs involved with the use of separate electrolyzers ohmic contact to p-n junction solar cells.[123] Another attractive advantage of PEC water splitting is that an electric field can be applied at the semiconductor/liquid junction to improve the photogenerated charges separation process. So, PEC water splitting, a significant and useful technology, needs to be research quickly.

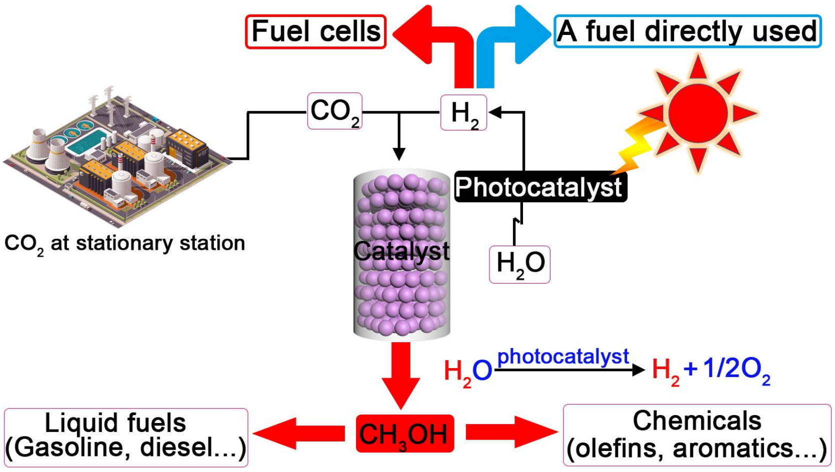

**Figure 1-21**. Application approach of the hydrogen energy conversed from photocatalysis method.

PEC water overall splitting cell is composed by ohmic contact a photoanode and a photocathode. Now the water splitting performance of photoanode is not high enough, so that influence the performance of PEC water overall splitting cell. There are two main disadvantages to limit the property of photoande. For the one, the transfer capacity of the photogenerated carriers in the photoanode is relative weakness. The other one is that the oxidation energy barrier of the photoanode is too high to limit the water oxidation reaction by photogenerated holes. Fabrication of oxygen vacancy on the surface of the semiconductor photoanode has been proved an efficiency method to resolve above two disadvantages. However, which one state of the oxygen vacancy can improve the PEC performance of photoanode and the mechanism are still not clear. This is an essential question about oxygen vacancy modified photoanode. So, in this thesis, firstly, I have mark some research works on this topics. Furthermore, to date, only point defects have been employed to modify the photoanode. Other two species of crystal defects, such as line defects and planar defects, have not been studied in this area. In this thesis, the line defect (dislocation) has been prepared on the semiconductor photoanode, and the functions of the line defect during PEC water splitting have been investigated also.

This thesis reports on investigation of defect on semiconductor photoanode for photoelectrochemical water splitting. This thesis is divided into four sections:

Chapter 2 is the experimental section, in which the synthesis process and experimental setups using in this thesis was introduced, including photoanode preparation method, PEC performance testing setup, PEC water splitting for hydrogen and oxygen evolution testing setup, technologies for defects analysis, electrochemical testing measurements and theoretical calculations.

Chapter 3 fabricates mesoporous $BiVO_4$ and Mo-doped $BiVO_4$ (BiMoVO) photoanodes by electrochemical deposition and elements thermal exchange method. The potentiostatic reduction method was employed to fabricate oxygen vacancy on the surface of the photoanodes, meanwhile the states of the oxygen vacancy was controlled. Furthermore the functions of the oxygen vacancies with different states were studied. And the results indicated that the real reason for the improving PEC performance of BiMoVO photoanode was not the well-defined surface oxygen vacancy formation, but only the Bi-O bonds crack on the surface of (020) facet.

Chapter 4, in this chapter, we employed a chemical etching method to treat the titanium foil substrate to accomplish a sharp-mountain like nano structure. Then $WO_3$ nanoflower (NF) like thin film was growth on it by hydrothermal method. The growth process, optical property, electrochemical property and PEC water oxidation performance of these NF $WO_3$ photoanodes were tested.

Chapter 5, in this chapter, the line defect (edged dislocation) was found on the surface of $WO_3$ NF single crystal. The line defects on the surface of $WO_3$ nanosheet were characterized carefully. Furthermore the functions of the edged dislocation during the PEC water splitting process were investigated also.

At last, the future research works of photoanode modification base on crystal defects were prospected in Chapter 6.

## §1.8. Reference

[1] N. S. Lewis and D. G. Nocera, “Powering the planet: Chemical challenges in solar energy utilization,” *Proc. Natl. Acad. Sci.*, 103, (2006) 15729.

[2] J. E. Trancik, “Renewable energy: Back the renewables boom,” *Nat.*, 507, (2014) 300.

[3] M. Gong, D. Y. Wang, C. C. Chen, B. J. Hwang and H. Dai, “A mini review on nickel-based electrocatalysts for alkaline hydrogen evolution reaction,” *Nano Res.*, 9, (2016) 28.

[4] M.G. Walter, E.L. Warren, J.R. McKone, S.W. Boettcher, Q. Mi, E.A. Santori and N.S. Lewis, “Solar Water Splitting Cells,” *Chem. Rev.,* 110, (2010) 6446.

[5] N. S. Lewis, “Toward cost-effective solar energy use,” *Science*, 315, (2007) 798.

[6] Y. Tachibana, L. Vayssieres and J. R. Durrant, Artificial photosynthesis for solar water-splitting. *Nat. Photon.*, 6, (2012) 511.

[7] T. Hisatomi, J. Kubota and K. Domen, “Recent advances in semiconductors for photocatalytic and photoelectrochemical water splitting,” *Chem. Soc. Rev.*, 43, (2014) 7520.

[8] A. Fujishima and K. Honda, “Electrochemical photolysis of water at a semiconductor electrode,” *Nature*, 238, (1972) 37.

[9] J. H. Li and J. Z. Zhang, “Optical properties and applications of hybrid semiconductor nanomaterials,” *Coordin. Chem. Rev*, 253, (2009) 3015.

[10] A. G. Munoz, C. Heine, M. Lublow, H. W. Klemm, N. Szabo, T. Hannappel and H. J. Lewerenz, “Photoelectrochemical conditioning of MOVPE p-InP films for light-induced hydrogen evolution: chemical, electronic and optical properties,” *ECS J. Solid State Sci. Technol.*, 2, (2013) Q51.

[11] P. Jackson, D. Hariskos, E. Lotter, S. Paetel, R. Wuerz, R. Menner, W. Wischmann and M. Powalla, “New world record efficiency for Cu(In, Ga)$Se_2$ thin-film solar cells beyond 20%,” *Prog. Photovoltaics: Res. Appl.*, 19, (2011) 894.

[12] D. Yokoyama, T. Minegishi, K. Maeda, M. Katayama, J. Kubota, A. Yamada, M. Konagai and K. Domen, “Photoelectrochemical water splitting using a Cu(In, Ga)$Se_2$ thin film,” *Electrochem. Commun.*, 12, (2010) 851.

[13] M.G. Walter, E.L. Warren, J.R. McKone, S.W. Mi, Q. Boettcher, E. A, Santori and N. S. Lewis, “Solar water splitting cells,” *Chem. Rev.*, 110, (2010) 6446.

[14] A.J. Nozik, “p-n photoelectrolysis cells,” *Appl. Phys. Lett.*, 29, (1976) 150.

[15] K. Ohashi, J. McCann and J. M. Bockris, “Stable photoelectrochemical cells for the splitting of water,” *Nature*, 266, (1977) 610.

[16] K. Ohashi, J. McCann and J. M. Bockris, “Hydrogen and electricity from water and light,” *Int. J. Energy Res.*, 1, (1977) 259.

[17] J. Akikusa and S.U. Khan, “Photoelectrolysis of water to hydrogen in p-SiC/Pt and p-SiC/n-$TiO_2$ cells,” *Int. J. Hydrogen Energy*, 27, (2002) 863.

[18] W.B. Ingler Jr., S.U.M. Khan, “A Self-Driven p/n-$Fe_2O_3$ Tandem Photoelectrochemical Cell for Water Splitting,” *Electrochem. Solid-State Lett.*, 9, (2006) G144.

[19] R.C. Kainthla, B. Zelenay and J.M. Bockris, “Significant Efficiency Increase in Self-Driven Photoelectrochemical Cell for Water Photoelectrolysis,” *J. Electrochem. Soc.*, 134, (1987) 841.

[20] Q. P. Chen, J.H. Li, X.J. Li, K. Huang, B.X. Zhou, W.M. Cai and W.F. Shangguan, "Visible-light responsive photocatalytic fuel cell based on $WO_3$/W photoanode and $Cu_2O$/Cu photocathode for simultaneous wastewater treatment and electricity generation," *Environ. Sci. Technol.*, 46, (2012) 11451.

[21] M. Xu, P.M. Da, H.Y. Wu, D.Y. Zhao and G.F. Zheng, "Controlled Sn-Doping in $TiO_2$ Nanowire Photoanodes with Enhanced Photoelectrochemical Conversion," *Nano lett.*, 12, (2017) 1503.

[22] C. Das, P. Roy, M. Yang, H. Jha and P. Schmuki, "Nb doped $TiO_2$ nanotubes for enhanced photoelectrochemical water-splitting," *Nanoscale*, 3, (2011) 3094-3096.

[23] H. Li , J.Q. Chen, Z.B. Xia, and J.H. Xing, "Microwave-assisted preparation of self-doped $TiO_2$ nanotube arrays for enhanced photoelectrochemical water splitting," *J. Mater. Chem. A*, 3, (2015) 699.

[24] K. Iwashina and A. Kudo, "Rh-doped $SrTiO_3$ photocatalyst electrode showing cathodic photocurrent for water splitting under visible-light irradiation," *J. Am. Chem. Soc.*, 133, ( 2011) 13272-13275.

[25] N.T. Hahn and C.B. Mullins, "Photoelectrochemical Performance of Nanostructured Ti- and Sn-Doped α- $Fe_2O_3$ Photoanodes," *Chem. Mater.*, 22, (2010) 6474-6482.

[26] S. Hoang, S.W. Guo, N. T. Hahn,.A. J. Bard,and C. B. Mullins, "Visible Light Driven Photoelectrochemical Water Oxidation on Nitrogen-Modified $TiO_2$ Nanowires," *Nano lett.* , 12,(2011) 26.

[27] C.L. Chen, Y.L. Wei, G.Z. Yuan, Q.L. Liu, R.R. Lu, X. Huang, Y. Cao, and P.H. Zhu, "Synergistic Effect of Si Doping and Heat Treatments Enhances the Photoelectrochemical Water Oxidation Performance of $TiO_2$ Nanorod Arrays," *Adv. Funct. Mater.*, (2017) 1701575

[28] Y.C. Qiu, K.Y. Yan, H. Deng, and S.H. Yang, "Secondary Branching and Nitrogen Doping of ZnO Nanotetrapods:Building a Highly Active Network for Photoelectrochemical Water Splitting," *Nano lett.*, 12, (2011) 407.

[29] M. Wang , F. Ren, J.G. Zhou, G.X. Cai, L. Cai, Y.F. Hu, D.N. Wang, Y.C. Liu, L.J. Guo, and S.H. Shen, "Photoelectrochemical Water Splitting under Visible Light: Engineered Impurity Distribution and Terraced Band Structure," *Sci. Rep.*, 5, (2015) 12925.

[30] W.D. Chemelewski, N.T. Hahn, and C.B. Mullins, "Effect of Si Doping and Porosity on Hematite's (α-$Fe_2O_3$) Photoelectrochemical Water Oxidation

Performance," *J. Phys.Chem. C*, 116, (2012) 5255.

[31] X.J. Zhang, M. Zeng, J.W. Zhang, A.M. Song, and S.W. Lin, "Improving photoelectrochemical performance of highly-ordered $TiO_2$ nanotube arrays with cosensitization of PbS and CdS quantum dots," *RSC Adv.*, *6*, (2016) 8118.

[32] Y.P. Xie, Z.B. Yu, G. Liu, X.L. Ma, and H.M. Cheng, "CdS-mesoporous ZnS core-shell particles for efficient and stable photocatalytic hydrogen evolution under visible light," *Energy Environ. Sci.*, 7, (2014) 1895.

[33] G.M. Wang, X.Y. Yang, F. Qian, J.Z. Zhang, and Y. Li, "Double-sided CdS and CdSe quantum dot co-sensitized ZnO nanowire arrays for photoelectrochemical hydrogen generation," *Nano Lett.*, 10, (2010) 1088.

[34] David Eisenberg, Hyun S. Ahn, and Allen J. Bard, "Enhanced photoelectrochemical water oxidation on bismuth vanadate by electrodeposition of amorphous titanium dioxide," *J. Am. Chem. Soc.*, 136, (2014) 14011.

[35] J.Z. Su, L.J. Guo, N.Z. Bao, and Craig A. Grimes, "Nanostructured $WO_3/BiVO_4$ heterojunction films for efficient photoelectrochemical water splitting," *Nano Lett.*, 11, (2011) 1928.

[36] Y. Hou, F. Zuo, Alex Dagg, and P.Y. Feng, "Visible Light-Driven $\alpha$-$Fe_2O_3$ Nanorod/Graphene/$BiV_{1-x}Mo_xO_4$ Core/Shell Heterojunction Array for Efficient Photoelectrochemical Water Splitting," *Nano Lett.*, 12, (2012) 6464.

[37] Savio J. A. Moniz, J. Zhu, and J.W. Tang, "1D Co-Pi modified $BiVO_4$/ZnO junction cascade for efficient photoelectrochemical water cleavage," *Adv. Energy Mater.*, 4, (2014) 1066.

[38] M.Z. Xie, X.D. Fu, L.Q. Jing, P. Luan, Y.J. Feng, and H.G. Fu, "Long‐lived, visible‐light‐excited charge carriers of $TiO_2/BiVO_4$ nanocomposites and their unexpected photoactivity for water splitting," *Adv. Energy Mater.*,4, (2014) 39.

[39] Hyun Gyu Kim, Pramod H. Borse, Jum Suk Jang, Euh Duck Jeong, Ok-Sang Jung, Yong Jae Suh and Jae Sung Lee, "Fabrication of $CaFe_2O_4/MgFe_2O_4$ bulk heterojunction for enhanced visible light photocatalysis," *Chem. Commun.*, (2009) 5889.

[40] Hyun G. Kim Dr., Pramod H. Borse Dr., Wonyong Choi and J. S. Lee, "Photocatalytic nanodiodes for visible‐light photocatalysis," *Angew. Chem., Int. Ed.*, 117, (2005) 4661.

[41] Mahmoud G. Ahmed, Tarek A. Kandiel, Amira Y. Ahmed, Imme Kretschmer,

Farouk Rashwan and Detlef Bahnemann, “Enhanced photoelectrochemical water oxidation on nanostructured hematite photoanodes via p-$CaFe_2O_4$/n-$Fe_2O_3$ heterojunction formation,” *J. Phys. Chem. C*, 119, (2015) 5864.

[42] Z.W. Liu, W.B. Hou, Prathamesh Pavaskar, Mehmet Aykol and Stephen B. Cronin, “Plasmon resonant enhancement of photocatalytic water splitting under visible illumination,” *Nano Lett.*, 11, (2011) 1111.

[43] X. Zhang , F. Wang , H. Huang , H.T. Li , X. Han , Y. Liu and Z.H. Kang, “Carbon quantum dot sensitized $TiO_2$ nanotube arrays for photoelectrochemical hydrogen generation under visible light,” *Nanoscale*, 5, (2013) 2274.

[44] Y.J. Zhang, Toshiyuki Mori, L. Niu and J.H. Ye, “Non-covalent doping of graphitic carbon nitride polymer with graphene: controlled electronic structure and enhanced optoelectronic conversion,” *Energy Environ. Sci.*, 4, (2011) 4517.

[45] Masanobu Higashi, Kazunari Domen and Ryu Abe, “Fabrication of efficient TaON and $Ta_3N_5$ photoanodes for water splitting under visible light irradiation,” *Energy Environ. Sci.*, 4, (2011) 4138.

[46] Y.B. Li, L. Zhang, Almudena Torres-Pardo, Jose M. Gonza′lez-Calbet, Y.H. Ma, Peter Oleynikov, Osamu Terasaki, Shunsuke Asahina, Masahide Shima, Dongkyu Cha, L. Zhao, Kazuhiro Takanabe, Jun Kubota and Kazunari Domen “Cobalt phosphate-modified barium-doped tantalum nitride nanorod photoanode with 1.5% solar energy conversion efficiency,” *Nat. Commun.*, 4, (2013) 2566.

[47] M.J. Liao, J.Y. Feng, W.J. Luo, Z.Q. Wang, J.Y. Zhang, Z.S. Li, T. Yu and Z.G. Zou, “$Co_3O_4$ nanoparticles as robust water oxidation catalysts towards remarkably enhanced photostability of a $Ta_3N_5$ photoanode,” *Adv. Funct. Mater.*, 22, (2012) 3066.

[48] L. Gao, Y.C. Cui, J. Wang, Alessandro Cavalli, Anthony Standing, Thuy T. T. Vu, Marcel A. Verheijen, Jos E. M. Haverkort, Erik P. A. M. Bakkers and Peter H. L. Notten, “Photoelectrochemical hydrogen production on InP nanowire arrays with molybdenum sulfide electrocatalysts,” *Nano Lett.*, 14, (2014) 3715.

[49] Z.R. Zhang, O. Bondarchuk, J.M. White, B.D. Kay and Z. Dohnálek, “Imaging adsorbate O-H bond cleavage: methanol on $TiO_2$ (110),” *J. Am. Chem. Soc.*, 128, (2006) 4198.

[50] J.P. Wang, Z.Y. Wang, B.B. Huang, Y.D. Ma, Y.Y. Liu, X.Y. Qin, X.Y. Zhang and Y. Dai, “Oxygen vacancy induced band-gap narrowing and enhanced visible light photocatalytic activity of ZnO,” *ACS Appl. Mater. Interfaces*, 4, (2012) 4024.

[51] K.R. Lai, W. Wei, Y.T. Zhu, M. Guo, Y. Dai and B.B. Huang, “Effects of

oxygen vacancy and N-doping on the electronic and photocatalytic properties of $Bi_2MO_6$ (M= Mo, W),” *J. Solid State Chem.*, 187, (2012) 103.

[52] L.Q. Jing, B.F. Xin, F.L. Yuan, L.P. Xue, B.Q. Wang and H.G. Fu, “Effects of surface oxygen vacancies on photophysical and photochemical processes of Zn-doped $TiO_2$ nanoparticles and their relationships,” *J. Appl. Phys. C.*, 110, (2006) 17860.

[53] A.D. Martinez, E.L. Warren, P. Gorai, K.A. Borup, D. Kuciauskas, P.C. Dippo, B.P. Ortiz, R.T. Macaluso, S.D. Nguyen, A.L. Greenaway, S.W. Boettcher, A.G. Norman, V. Stevanovic, E.S. Toberer and A.C. Tamboli, “Solar energy conversion properties and defect physics of $ZnSiP_2$,” *Energy Environ. Sci.*, 9, (2016) 1031.

[54] L.Q. Ye, K.J. Deng, F. Xu, L.H. Tian, T.Y. Peng and L. Zan, “Increasing visible-light absorption for photocatalysis with black BiOCl,” *Phys. Chem. Chem. Phys.*, 14, (2012) 82.

[55] J.Y. Gan, X.H. Lu, J.H. Wu, S.L. Xie, M.H. Yu, Z.S. Zhang, Y.C. Mao, S.C. Wang, Y. Shen and Y.X. Tong, “Oxygen vacancies promoting photoelectrochemical performance of $In_2O_3$ nanocubes,” *Sci. Rep.*, 3, (2013) 1021.

[56] N.H. Hong, J. Sakai and V. Brizé, “Observation of ferromagnetism at room temperature in ZnO thin films,” *J. Phys.: Condens. Matter*, 19, (2007) 036219.

[57] M.V. Limaye, S.B. Singh, R. Das, P. Poddar and S.K. Kulkarni, “Room temperature ferromagnetism in undoped and Fe doped ZnO nanorods: microwave-assisted synthesis,” *J. Solid State Chem.*, 184, (2011) 391.

[58] L. Pan, S.B. Wang, W.B. Mi, J.J. Song, J.J. Zou, L. Wang and X.W. Zhang, “Undoped ZnO abundant with metal vacancies,” *Nano Energy*, 9, (2014) 71.

[59] H.F. Mataré, “Defect electronics in semiconductors,” *John Wiley & Sons*, 1971.

[60] X. B. Chen, L. Liu, P. Y. Yu and S. S. Mao, “Increasing solar absorption for photocatalysis with black hydrogenated titanium dioxide nanocrystals,” *Science*, 331, (2011) 746.

[61] A. Naldoni, M. Allieta, S. Santangelo, M. Marelli, F. Fabbri, S. Cappelli, C. L. Bianchi, R. Psaro and V. D. Santo, “Effect of Nature and Location of Defects on Bandgap Narrowing in Black $TiO_2$ Nanoparticles,” *J. Am. Chem. Soc.*, 134, (2012) 7600.

[62] L. Ye, K. Deng, F. Xu, L. Tian, T. Peng and L. Zan, Increasing visible-light absorption for photocatalysis with black BiOCl. *Phys. Chem. Chem. Phys.*, 14, (2012) 82.

[63] H. Cui , W. Zhao, C. Yang, H. Yin, T. Lin, Y. Shan, Y. Xie, H. Gu and F. Huang,

"Black $TiO_2$ nanotube arrays for high-efficiency photoelectrochemical water-splitting," *J. Mater. Chem. A*, 2, (2014) 8612.

[64] M. Kong, Y. Li, X. Chen, T. Tian, P. Fang, F. Zheng and X. Zhao, "Tuning the relative concentration ratio of bulk defects to surface defects in $TiO_2$ nanocrystals leads to high photocatalytic efficiency," *J. Am. Chem. Soc.*, 133, (2011) 16414.

[65] X. Zhang, X.B. Wang, L.W. Wang, W.K. Wang, L.L. Long, W.W. Li and H.Q. Yu, "Synthesis of a highly efficient BiOCl single-crystal nanodisk photocatalyst with exposing {001} facets," *ACS Appl. Mater. Interfaces*, 6, (2014) 7766.

[66] J. Jiang, K. Zhao, X. Y. Xiao and L. Z. Zhang, "Synthesis and facet-dependent photoreactivity of BiOCl single-crystalline nanosheets," *J. Am. Chem. Soc.*, 134, (2012) 4473.

[67] G. S. Li, B. Jiang, S. N. Xiao, Z. C. Lian, D. Q. Zhang, J. C. Yu and H. X. Li, "An efficient dye-sensitized BiOCl photocatalyst for air and water purification under visible light irradiation," *Environ. Sci.: Processes Impacts*, 16, (2014) 1975.

[68] O. Bikondoa, C. L. Pang, R. Ithnin, C. A. Muryn, H. Onishi and G. Thornton, "Direct visualization of defect-mediated dissociation of water on $TiO_2$ (110)," *Nat. Mater.*, 5, (2006) 189.

[69] A. Tilocca and A. Selloni, "Structure and reactivity of water layers on defect-free and defective anatase $TiO_2$ (101) surfaces," *J. Phys. Chem. B*, 108, (2004) 4743.

[70] A. Tilocca and A. Selloni, DFT-GGA and DFT+U simulations of thin water layers on reduced $TiO_2$ anatase. *J. Phys. Chem. C*, 116, (2012) 9114.

[71] U. Aschauer, Y. He, H. Cheng, S. C. Li, U. Diebold and A. Selloni, "Influence of subsurface defects on the surface reactivity of $TiO_2$: water on anatase (101)," *J. Phys. Chem. C*, 4, (2009) 1278.

[72] Y. Liu, H. Cheng, M. Lyu, S. Fan, Q. Liu, W. Zhang, Y. Zhi, C. Wang, C. Xiao, S. Wei, B. Ye and Y. Xie, "Low overpotential in vacancy-rich ultrathin $CoSe_2$ nanosheets for water oxidation," *J. Am. Chem. Soc.*, 136, (2014) 15670.

[73] H. Li, J. Shang, Z. Ai and L. Zhang, "Efficient visible light nitrogen fixation with BiOBr nanosheets of oxygen vacancies on the exposed {001} facets," *J. Am. Chem. Soc.*, 137, (2015) 6393.

[74] A.K. Bhattacharya, K.K. Mallick and A. Hartridge, "Phase transition in $BiVO_4$," *Mater. Lett.*, 30, (1997) 7.

[75] K. Sayama, A. Nomura, T. Arai, T. Sugita, R. Abe, M. Yanagida, T. Oi, Y.

Iwasaki, Y. Abe and H. Sugihara, “Photoelectrochemical decomposition of water into $H_2$ and $O_2$ on porous $BiVO_4$ thin-film electrodes under visible light and significant effect of Ag ion treatment,” *J. Phys. Chem. B*, 110, (2006) 11352.

[76] P. Cai, S.M. Zhou, D.K. Ma, S.N. Liu, W. Chen and S.M. Huang, “$Fe_2O_3$-modified porous $BiVO_4$ nanoplates with enhanced photocatalytic activity,” *Nano-Micro Lett.*, 7, (2015) 183.

[77] A. Kudo, K. Omori and H. Kato, “A novel aqueous process for preparation of crystal form-controlled and highly crystalline $BiVO_4$ powder from layered vanadates at room temperature and its photocatalytic and photophysical properties,” *J. Am. Chem. Soc.*, 121, (1999) 11459.

[78] H.Y. Jigng, H.X. Dai, X. Meng, L. Zhang, J.G. Deng and K. Ji, “Morphology-dependent photocatalytic performance of monoclinic $BiVO_4$ for methyl orange degradation under visible-light irradiation,” *Chin. J. Catal.*, 32, (2011) 939.

[79] K. Sayama, A. Nomura, Z.G. Zou, R. Abe, Y. Abeb and H. Arakawa, “Photoelectrochemical decomposition of water on nanocrystalline $BiVO_4$ film electrodes under visible light,” *Chem. Commun.*, (2003) 2908.

[80] W.J. Luo, Z.Q. Wang, L.J. Wan, Z.S. Li, T. Yu and Z.G. Zou, “Synthesis, growth mechanism and photoelectrochemical properties of $BiVO_4$ microcrystal electrodes,” J. Phys. D: Appl. Phys., 43, (2010) 405402.

[81] H. Ye, J. Lee, J.S. Jang and A.J. Bard, “Rapid screening of $BiVO_4$-based photocatalysts by scanning electrochemical microscopy (SECM) and studies of their photoelectrochemical properties,” *J. Phys. Chem. C*, 114, (2010) 13322.

[82] J.A. Seabold and K.S. Choi, “Efficient and stable photo-oxidation of water by a bismuth vanadate photoanode coupled with an iron oxyhydroxide oxygen evolution catalyst,” *J. Am. Chem. Soc.*, 134, (2012) 2186.

[83] P. Madhusudan, J. Ran, J. Zhang, J.G. Yu and G. Liu, “Novel urea assisted hydrothermal synthesis of hierarchical $BiVO_4/Bi_2O_2CO_3$ nanocomposites with enhanced visible-light photocatalytic activity,” *Appl. Catal., B*, 110, (2011) 286.

[84] X.k. Wang, G.c. Li, J. Ding, H.R. Peng and K.Z. Chen, “Facile synthesis and photocatalytic activity of monoclinic $BiVO_4$ micro/nanostructures with controllable morphologies,” *Mater. Res. Bull.*, 47, (2012) 3814.

[85] S. Eda, M. Fujishima and H. Tada, “Low temperature-synthesis of $BiVO_4$ nanorods using polyethylene glycol as a soft template and the visible-light-activity for copper acetylacetonate decomposition,” *Appl. Catal., B*, 125, (2012) 288.

[86] Z.X. Zhao, H.X. Dai , J.G. Deng, Y.X. Liu, and C. Tong, "Au Enhanced visible-light photocatalytic activities of porous olive-shaped sulfur-doped $BiVO_4$-supported cobalt oxides," *Solid State Sci.*, 18, (2013) 98.

[87] Z.F. Zhu, J. Du, J.Q. Li, Y.L. Zhang, and D.G. Liu, "An EDTA-assisted hydrothermal synthesis of $BiVO_4$ hollow microspheres and their evolution into nanocages," *Ceramurgia Int.*, 38, (2012) 482.

[88] H. Xu, C.d. Wu, H.m. Li, J.y. Chu, G.s. Sun, Y.g. Xu and Y.S. Yan, "Synthesis, characterization and photocatalytic activities of rare earth-loaded $BiVO_4$ catalysts," *Appl. Surf. Sci.,* 256, (2009) 597.

[89] M. Wang, Y.S. Che, C. Niu, M.Y. Dang and D. Duo, "Lanthanum and boron co-doped $BiVO_4$ with enhanced visible light photocatalytic activity for degradation of methyl orange," *J. Rare Earths*, 31, (2013)878.

[90] X.F. Zhang, Y.B. Zhang, X. Quan and S. Chen, "Preparation of Ag doped $BiVO_4$ film and its enhanced photoelectrocatalytic (PEC) ability of phenol degradation under visible light," *J. Hazard. Mater.*, 167, (2009) 911.

[91] W.J. Luo, Z.S. Li, T. Yu and Z.G. Zou, "Effects of surface electrochemical pretreatment on the photoelectrochemical performance of Mo-doped $BiVO_4$," *J. Phys. Chem. C*, 116, (2012), 5076.

[92] D.K. Lee,I.S. Cho, S. Lee, S.T. Bae, J.H. Noh, D.W. Kim and K.S. Hong, "Effects of carbon content on the photocatalytic activity of C/$BiVO_4$ composites under visible light irradiation," *Mater. Chem. Phys.*, 119, (2010) 106.

[93] M. Wang, Q. Liu, Y.S. Che, L.F. Zhang and D. Zhang, "Characterization and photocatalytic properties of N-doped $BiVO_4$ synthesized via a solgel method," *J. Alloys Compd.*, 548, (2013) 70.

[94] X.F. Zhang, X. Quan, S. Chen and Y.B. Zhang, "Effect of Si doping on photoelectrocatalytic decomposition of phenol of $BiVO_4$ film under visible light," *J. Hazard. Mater.*, 177, (2010) 914.

[95] P. Chatchai, Y. Murakami, S. Kishioka, A.Y. Nosaka and Y. Nosaka, " Efficient photocatalytic activity of water oxidation over $WO_3$/$BiVO_4$ composite under visible light irradiation," *Electrochim. Acta*, 54, (2009) 1147.

[96] W.R. Zhao, Y. Wang, Y. Yang, J. Tang and Y.N. Yang, "Carbon spheres supported visible-light-driven CuO-$BiVO_4$ heterojunction: preparation, characterization, and photocatalytic properties," *Appl. Catal., B*, 115, (2012) 90.

[97] We.Z. Wang, X.W. Huang, S. Wu, Y.X. Zhou, L.J. Wang, H.L. Shi, Y.J. Liang

and B. Zou, “Preparation of p-n junction $Cu_2O/BiVO_4$ heterogeneous nanostructures with enhanced visible-light photocatalytic activity,” *Appl. Catal., B*, 134, (2013) 293.

[98] L. Qian, P.F. Liu, L. Zhang, C.W. Wang, S. Yang, L.R. Zheng, A.P. Chen and H.G. Yang, “Amorphous ferric oxide as a hole-extraction and transfer layer on nanoporous bismuth vanadate photoanode for water oxidation,” *Chin. J. Catal.*, 38, (2017) 1045.

[99] A.p. Zhang and J.Z. Zhang, “Characterization and photocatalytic properties of $Au/BiVO_4$ composites ,” *J. Alloys Compd.*, 49, (2010) 631.

[100] D. Wang, R.G. Li, J. Zhu, J.Y. Shi, J.F. Han, X. Zong and C. Li, “Photocatalytic water oxidation on $BiVO_4$ with the electrocatalyst as an oxidation cocatalyst: essential relations between electrocatalyst and photocatalyst,” *J. Phys. Chem. C*, 116, (2012) 5082.

[101] R.G. Li, H.X. Han, F.X. Zhang, D.G. Wang and C. Li, “Highly efficient photocatalysts constructed by rational assembly of dual-cocatalysts separately on different facets of $BiVO_4$,” *Energy Environ. Sci.*, 7, (2014) 1369.

[102] Y.H. Ng, A. Iwase, A. Kudo and R. Amal, “Reducing graphene oxide on a visible-light $BiVO_4$ photocatalyst for an enhanced photoelectrochemical water splitting,” *J. Phys. Chem. Lett.* , 1, (2010) 2607.

[103] B. Yang, H. Li, M. Blackford and V. Luca, “Novel low density mesoporous $WO_3$ films prepared by electrodeposition,” *Curr. Appl. Phys.*, 6, (2006) 436.

[104] X.Q. Chen, J.H. Ye, S.X. Ouyang, T. Kako, Z.S. Li and Z.G. Zou, “Enhanced incident photon-to-electron conversion efficiency of tungsten trioxide photoanodes based on 3D-photonic crystal design,” *Acs Nano*, 5, (2011) 4310.

[105] M.R. Waller, T.K. Townsend, J. Zhao, E.M. Sabio, and R.L. Chamousis, N.D. Browning and F.E. Osterloh, “Single-crystal tungsten oxide nanosheets: Photochemical water oxidation in the quantum confinement regime,” *Chem. Mater.*, 24, (2012) 698.

[106] J. Polleux, N. Pinna, M. Antonietti and M. Niederberger, “Growth and assembly of crystalline tungsten oxide nanostructures assisted by bioligation,” *J. Am. Chem. Soc.*, 127, (2005), 15595.

[107] H.G. Choi, Y.H. Jung and D.K. Kim, “Solvothermal synthesis of tungsten oxide nanorod/nanowire/nanosheet,” *J. Am. Ceram. Soc.*, 88, (2005), 1684.

[108] S.L. Bai, K.W. Zhang, R.X. Luo, D.Q. Li, A.F. Chen and C.C. Liu, “Low-temperature hydrothermal synthesis of $WO_3$ nanorods and their sensing

properties for $NO_2$," *J. Mater. Chem.*, 22, (2012) 12643.

[109] F. Zheng, M. Guo and M. Zhang, "Hydrothermal preparation and optical properties of orientation-controlled $WO_3$ nanorod arrays on ITO substrates," *CrystEngComm*, 15, (2013) 277.

[110] J.G. Yu and L.F. Qi, "Template-free fabrication of hierarchically flower-like tungsten trioxide assemblies with enhanced visible-light-driven photocatalytic activity," *J. Hazard. Mater.*, 169, (2009), 221.

[111] J.P. Du, Q.Y. Chen, J. Zhao and J. Li, "$WO_3$ doped with Ce: characterization and photocatalytic properties for water splitting," *Chinese J. Inorg. Chem.*, 6, (2007) 011.

[112] Q. Xiang, G.F. Meng, H.B. Zhao, Y. Zhang, H. Li, W.J. Ma and J.Q. Xu, "Au nanoparticle modified $WO_3$ nanorods with their enhanced properties for photocatalysis and gas sensing," *J. Phys. Chem. C*, 114, (2010) 2049.

[113] D. Paluselli, B. Marsen, E.L. Miller and R.E. Rocheleau, "Nitrogen doping of reactively sputtered tungsten oxide films," *Electrochem. Solid-State Lett.*, 8, (2005), G301.

[114] B. Cole, B. Marsen, E. Miller, Y.F. Yan, B. To, K. Jones and M. Al-Jassim, "Evaluation of nitrogen doping of tungsten oxide for photoelectrochemical water splitting," *J. Phys. Chem. C*, 112, (2008) 5213.

[115] X.H. Ding, D.W. Zeng, S.P. Zhang and C.S. Xie, "C-doped $WO_3$ microtubes assembled by nanoparticles with ultrahigh sensitivity to toluene at low operating temperature," Sens. Actuators B, 155, (2011) 86.

[116] I. Grigioni, K.G. Stamplecoskie, E. Selli and P.V. Kamat, "Dynamics of photogenerated charge carriers in $WO_3/BiVO_4$ heterojunction photoanodes," *J. Phys. Chem. C*, 119, (2015) 20792.

[117] R. Solarska, A. Królikowska and J. Augustyński, "Silver nanoparticle induced photocurrent enhancement at $WO_3$ photoanodes," *Angew. Chem., Int. Ed.*, 49, (2010) 7980.

[118] Y. Liu, J. Li, W.Z. Li, Y.H. Yang, Y.M. Li and Q.Y. Chen, "Enhancement of the photoelectrochemical performance of $WO_3$ vertical arrays film for solar water splitting by gadolinium doping," *J. Phys. Chem. C*, 119, (2015) 14834.

[119] K.L. He, J. Xie, X.Y. Luo, J.Q. Wen, S. Ma, X. Li, Y.P. Fang and X.C. Zhang, "Enhanced visible light photocatalytic $H_2$ production over Z-scheme g-$C_3N_4$ nansheets/$WO_3$ nanorods nanocomposites loaded with $Ni(OH)_x$ cocatalysts," *Chin. J.*

*Catal.*, 38, (2017) 240.

[120] Y. Pihosh, I. Turkevych, K. Mawatari, T. Asai, T. Hisatomi, J. Uemura, M. Tosa, K. Shimamura, J. Kubota, K. Domen and T. Kitamori, “Nanostructured $WO_3/BiVO_4$ photoanodes for efficient photoelectrochemical water splitting,” *Small*, 10, (2014) 3692.

[121] A. J. Bard and M. A. Fox, “Artificial photosynthesis: solar splitting of water to hydrogen and oxygen,” *Acc. Chem. Res.* 28, (1995) 141.

[122] N. S. Lewis, “Light work with water,” *Nature*, 414, (2001) 589.

[123] J.A. Turner, “A realizable renewable energy future,” *Science*, 285, (1999) 1493.

# Chapter 2：Introduction of the experimental synthesis methods and test instruments

## §2.1. Experimental reagents

The reagents used in this thesis are showed in Table 2-1, and all regents never purify further.

**Table 2-1.** Experimental reagents

| Molecular formula | Purity | Manufacture factory |
|---|---|---|
| $Bi(NO_3)_3•5H_2O$ | AR | Aladin Industrial Corporation |
| KI | AR | Aladin Industrial Corporation |
| $HNO_3$ | AR | Aladin Industrial Corporation |
| p-benzoquinone | AR | Sigma-Aldrich |
| Vanadyl(IV) acetylacetonate | AR | Sigma-Aldrich |
| Molybdenyl acetylacetonate | AR | Sigma-Aldrich |
| Dimethyl sulfoxide | AR | Aladin Industrial Corporation |
| NaOH | AR | Aladin Industrial Corporation |
| Sodium sulfate | AR | Aladin Industrial Corporation |
| Titanium foil | 99.99% | Sigma-Aldrich |
| Ethanol | AR | Aladin Industrial Corporation |
| Acetone | AR | Aladin Industrial Corporation |
| HCl (37 %) | AR | Aladin Industrial Corporation |
| $H_2WO_4$ | AR | Sigma-Aldrich |
| Polyvinyl alcohol | AR | Aladin Industrial Corporation |
| $H_2O_2$ (30%) | AR | Aladin Industrial Corporation |
| $WCl_6$ | AR | Sigma-Aldrich |
| Silver slurry | - | Uninwell |

## §2.2. Experimental method

### §2.2.1. Electrochemical deposition

Electrochemical deposition is a method to fabricate thin film on conductive substrate under the extra applied electric field. The mechanism of electrochemical deposition is that ohmic contacted cathode and anode are immersed into the selected electrolyte to deposit a thin film with the redox reactions which drive by extra applied direct current. Commonly, electrochemical deposition method includes four steps, (I) the procedure of liquid mass transfer. In this procedure, the reaction ions will migrate to the liquid layer near the surface of the electrode; (II) Proconversion procedure. In this procedure, the reaction ions transfered at the electrode surface or liquid layer near the surface of electrode, which before the electrochemical reaction, such as surface ion adsorption and coordination number change of the complex ion etc. In this step, no electrons take part in. (III) Electron transfer procedure. In this procedure, the reaction ions get electrons, generating reduction products; (IV) Post conversion procedure. In this step, the products converse on the surface of electrode or liquid layer near the electrode after the electrochemical reaction. Such as the products desorption, decompose and dehydration etc.

### §2.2.2. Hydrothermal growth

Hydrothermal growth is the generic terms of the chemical reaction which occur in the fluid (water, water solution and/or steam) under certain temperature and pressure. The synthesis mechanism of hydrothermal growth method is that for some metal, their metal hydroxide solubility is much higher than that of their metal oxide, inducing metal oxide precipitate.

As the reaction temperature, the hydrothermal growth can be divided into subcritical reaction and supercritical reaction. The reaction temperature of the former one is between the 100 ~ 240 °C, it is suitable for industrial and laboratory application to prepare some nanomaterials with special morphologies. The reaction temperature of supercritical reaction is higher than 1000 °C, and the pressure higher than 0.3Gpa. In this situation, the water goes into supercritical state. The special characters of the supercritical water can be used to reaction with the reacting matter to prepare products with special properties.

## §2.3. Experimental Instrument

### §2.3.1. X-Ray Diffraction

The X-Ray Diffraction (XRD) results of the samples were tested by the machine of D/MAX-2500/PC-XRD. Measurement parameters: the wavelength of CuKα ray is 0.154 nm, voltage is 40 kV, current is 20 mA. XRD can be employed to test the long-range order structure of the crystal. It is an efficient method to research the microstructure of the crystal to get the information of the crystal structure, property and diameter.

### §2.3.2. Scanning Electron Microscopy

The working mechanism of Scanning Electron Microscopy (SEM) is that an extreme narrow electron beam was used to scan the sample to stimulate secondary electrons from the surface of it. The amount of secondary electrons relative to the incident angle of the electron beam, that is relative to the surface structure of the sample. These secondary electrons will collecte by the prober, and be transformed to optical signal by the scintillator. Then the optical signal will be conversed to electric signal, thus control the intensity of the electron beam on the fluorescent screen, showing the scanning image synchronous with the electron beam. This scanning image is a three-dimension one, corresponding to the surface structure of the observed sample. In this thesis, JEOL JSM-6700F SEM was employed to observe the surface morphology of these photoanodes.

### §2.3.3. Transmission Electron Microscopy

Transmission Electron Microscopy (TEM) is an advanced measurement to observe the microstructure of the crystal from the atom level. In this thesis, the defect structures were observed by High-Resolution TEM, the acceleration voltage was 200 V. For sample preparation, the thin film on conducting substrate was separated by scraping, and dispersed into the alcohol with 15 Min ultrasonic. Then we sucked up 1μL dispersed solution, and added on the cupper micro grid, dried by the infrared lamp illumination.

### §2.3.4. X-ray Photoelectron Spectroscopy

The working mechanism of X-ray Photoelectron Sectroscopy (XPS) is based on the Einstein photoelectron emission law, it is appropriate for atoms, molecular and the solid formed by them. XPS is one of the effective technology to research the occupied electron state of the nanomaterials, because the electron structure of the solid can be copied via the suitable photons stimulation. In this thesis, Axis Ultra-XPS was emolyed to test the surface electron state of the prepared photoanode thin films, to point out the state of the defects.

### §2.3.4. Photoelectrochemical performance evaluate measurement

In this thesis, the PEC performance test measurement is shown in Figure 2-1. It is including Xenon light, quartzose reaction cell, electrochemical working station, platinum foil counter electrode and reference electrode etc. Figure 2-1a shows simulate sun light system, in this system the Xenon lamp used as incident light, the light filtered by AM 1.5G and water, and the light intensity controlled at 100 mW/cm$^2$. Figure 2-1b shows the test cell, including work electrode (WE), reference electrode (RE) and counter electrode (CE). The photoanode served as work electrode, with a active area 1cm×1cm. the Ag/AgCl and platinum foil served as RE and CE, respectively. An electrochemical work station (CHI 660D) was employed to test the PEC performance of these photoanodes. The produced hydrogen and oxygen can be pumped out along the sparger tube and collected by a vacuum system, then tested via a gas chromatography (GC).

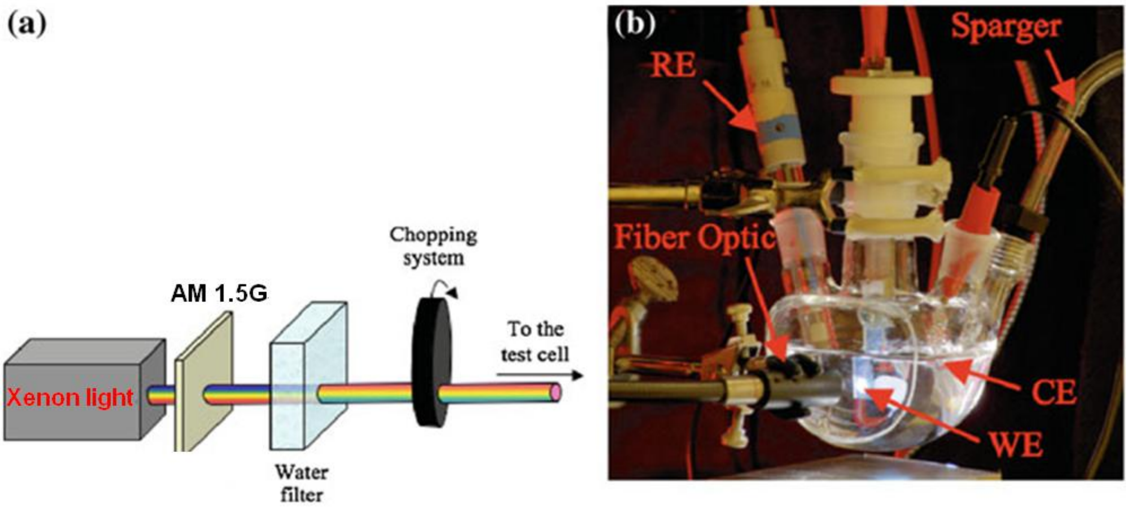

Figure 2-1. PEC performance evaluation system (a) simulate sun light system; (b) PEC reaction cell.

### Incident Photon-to-Current Efficiency (IPCE)

The Incident Photon-to-Current Efficiency (IPCE) is one of the most important diagnostic figures of merit for PEC devices; it describes the photocurrent collected per incident photon flux as a function of illumination wavelength. In a PEC system, IPCE is usually obtained from a chronoamperometry (potentiostatic) measurement. In this system, a bias can be applied between the sample/working electrode versus a counter electrode (2-electrode experiment) or a reference electrode (3-electrode experiment) while measuring the current that arises from subjecting the PEC electrode to monochromatic light at various wavelengths. The difference between the steady state current under monochromatic illumination and the steady state background current is the photocurrent that arises due to redox reactions occurring at the surface of the working electrode. The IPCE corresponds to the ratio of this photocurrent (converted to an electron rate) versus the rate of incident photons (converted from the calibrated power of a light source). Calibrated monochromated light (alone, or superimposed over a background illumination level in the case of a white light bias experiment) should be used for this experiment to give IPCE as a function of wavelength λ (nm).

$$IPCE(\lambda)=\frac{electrons/cm^2/s}{photons/cm^2/s}=\frac{j_{ph}(mA/cm^2)\times 1239.8(V\times nm)}{P_{mono}(mW/cm^2)\times\lambda(nm)} \tag{2-1}$$

where 1239.8 V 9 nm represents a multiplication of h (Planck’s constant) and c (the speed of light), Pmono is the calibrated and monochromated illumination power intensity in mW/cm$^2$, and λ (nm) is the wavelength at which this illumination power is measured.

# Chapter 3：Improvement of the PEC performance of Mo-doped BiVO4 photoanode via controlling the state of oxygen vacancy

## §3.1. Introduction for the oxygen vacancy on $BiVO_4$ photoanode

Conversion of Solar energy to chemical energy by photocatalysis or photoelectrochemistry methods have been widely considered as potential technologies, and attracted great attention in the past 40 years. [1-5] $BiVO_4$ has been widely considered as a potential photoanode material for photoelectrochemical (PEC) water oxidation, due to its wide light absorption range, high photocorrosion resistance and high cost-effective. [6-9] It is widely known that there are three main processes to decide the PEC performance of a photoelectrode, including photons absorption, photogenerated charge separation and surface electrochemical reaction. Recent years, on one hand, many methods including elements doping, [10-13] nanostructure design, [14-16] facet engineering[17-20] and surface modification [21-24] have been developed to improve the PEC operating processes of $BiVO_4$ photoanodes be mentioned above. Meanwhile, on the other hand, more and more research found that the free charge density in well-defined $BiVO_4$ crystal is too low to limit the photogenerated electrons transfer process of it. [25, 26] So, for further improving the PEC performance of $BiVO_4$ photoanode, this obstacle need to be surpassed. It found that surface reduction was a considerable technique to improve the free charge density of a semiconductor photoanode, including hydrogen high temperature treatment, [27-29] $NaBH_4$ reduction [30, 31] and electrochemical reduction, [32, 33] etc. And the PEC performance of these semiconductor photoanodes usually can be improved greatly after the reduction treatment. While the mechanism related is still far from clear. To date, the main accepted reason for the PEC property improvement is usually that the valency state of the metal element in semiconductor is changed with the reduction processing, leading to the formation of oxygen vacancy on the surface, thus increases the charge donor density of it. However, due to mostly resting on the speculation level, it is still lack of powerful and direct evidence to certify. Cooper et al. [34] treated the $BiVO_4$ photoanode in hydrogen at high temperature. Their results showed that the hydrogen were assigned to interstitial and substitutional sites at the surface of $BiVO_4$, then shifted the Femi level to approach the conduction band edge to enhance the n-type characteristic of $BiVO_4$. Rossell et al. [35] employed electron energy-loss spectroscopy in scanning transmission electron microscopy to find a 5-nm-thick reduction shell on the surface of monocline $BiVO_4$, which contributed to the vanadium reducing from +5 to about +4, thus, charge neutrality near the surface demands for ~15% oxygen vacancies. Ding et al. [36] reduced the $BiVO_4$ surface by $NaBH_4$ assistance, and found that the donor density of it was increased with the oxygen vacancy formation, so that improved the PEC performance of $BiVO_4$ photoanode.

As is well-known, oxygen vacancy can be classified into point defect,[37-39] which is a double-edged sword for the PEC performance of a photoelectrode. On one hand, the charge carrier density will be increased with the oxygen vacancy formed. On the other hand, these point defects will evolve into recombination center that to imcrease the recombination rate of the photogenerated charges.[40, 41] Thus, the state of the oxygen vacancy on the surface of the semiconductor may be very important for the PEC performance. In this study, we prepared mesoporous BiMoVO photoanode by electrochemical deposition and elements thermal exchange method successively. The potentiostatic method was employed to reduce the surface of it. The analysis results indicated that the surface state of the BiMoVO photoanode was changed gradually with the reduction potential enhancing. Combining with DFT calculation and the corresponding PEC performance, we can propose that the real reason for the improving PEC performance of BiMoVO photoanode was not the well-defined surface oxygen vacancy formation, but only the Bi-O bonds crack on the surface of (020) facet.

## §3.2. Experimental section

### §3.2.1. Preparation of oxygen vacancy modified BiVO4 and BiMoVO photoanodes

$BiVO_4$ and BiMoVO thin films were prepared by adapting a literature procedure.[6] Typically, as shown in Figure 3-1, 2 mmol $Bi(NO_3)_3{\bullet}5H_2O$ dissolved in 50mL 0.4mol/L KI solution, and adjust the pH to 1.7 by dilute $HNO_3$; subsequently, dropped 20 mL 4 mmol p-benzoquinone into the as-prepared solution by linearly with strong stirring. In order to deposition BiOI thin film, which is the precursor of $BiVO_4$, a potentiostatic method (provide by a CHI 660D, Shanghai Chenhua Instrument Co., Ltd., China) was employed. The deposition process was carried out in the above mixture solution by a three-electrode system, in which fluorine doped tin oxide (FTO) conducting glass, Ag/AgCl electrode and Platinum (Pt) served as work electrode, reference electrode and counter electrode, respectively. The deposition potential was controlled at -0.1 V with 4 Min to achieve an orange BiOI thin film on FTO. In order to transfer the BiOI into $BiVO_4$ and BiMoVO, V and V-Mo organic solution was prepared, respectively. Simply, 1 mmol vanadyl(IV) acetylacetonate or1 mmol vanadyl(IV) acetylacetonate and 0.03 mmol Molybdenyl acetylacetonate dissolved into 5 mL dimethyl sulfoxide by ultrasonic dispersion. Subsequently, coating 0.2 mL metal-organic solution on the surface of BiOI thin film, and dried at 80 °C, followed annealing at 450 °C in ambient for 2 hours. The prepared thin films were immersed into 1 M NaOH solution to dissolve the remaining $V_2O_5$ and $Mo_2O_5$, so that achieved the preparation of $BiVO_4$ and BiMoVO photoanodes. To control the state of the oxygen vacancy on the surface of BiMoVO, a potentiostatic method was employed. Some different reduction bias potentials (-0.6 V, -0.8 V, -1.0 V, -1.2 V vs Ag/AgCl) was applied on the BiMoVO photoanode for 5 Min by a three electrode system mentioned above in 0.1 M $Na_2SO_4$ solution, respectively, and the electrochemistry reduction BiMoVO photoanodes marked as -0.6-BiMoVO, -0.8-BiMoVO, -1-BiMoVO and -1.2-BiMoVO.

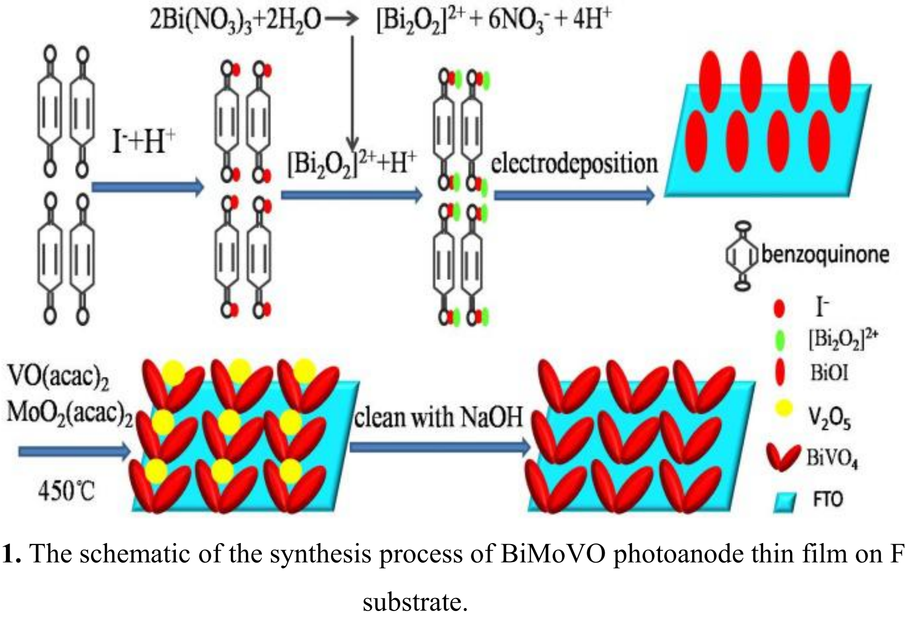

**Figure 3-1.** The schematic of the synthesis process of BiMoVO photoanode thin film on FTO substrate.

### §3.2.2. Characterizations of the prepared samples

Micro-morphologies of these photoanodes were observed by a scanning electron microscopy (SEM, JEOL JSM-6700F) and a field emission high-resolution transmission electron microscope (FE-HRTEM, Tecnai G2 F20). X-ray diffraction (XRD, D/MAX-2500/PC) was used to identify the crystalline structures of these photoanodes. Bonding information about these photoanodes were characterized by X-ray photoelectron spectroscopy (XPS, Axis Ultra). The optical absorption properties were characterized by UV–visible spectrophotometer (U-41000; HITACHI). The fluorescence spectrum (PL, Fluoro Max-4) was employed to characterize the PL density of these photoanodes.

### §3.2.3. Electrochemistry and Photoelectrochemistry measurements

A three-electrode system was used to measure the electrochemical and PEC performances of these photoanodes. Typically, photoanode, a piece of platinum, and Ag/AgCl (saturated KCl) were served as the working, counter, and reference electrodes, respectively. The water splitting photoelectrode was illuminated under 1 Sun and AM 1.5 G using a 300 W xenon lamp (PLS-SXE300, Beijing Changtuo Co. Ltd., Beijing, China) for solar simulation, The light intensity was controlled by a spectroradiometer (Thorlabs, PM100D). All tests were performed in 0.1 M $Na_2SO_4$ electrolyte. A front illumination style was employed to stimulate the photoanode. The photoinduced current density with time (*I-t*) curves were measured at a bias potential of 1 V (*vs.* Ag/AgCl). The linear sweep voltammetry (*I-V*) curves were measured from 0 to 1.5 V (*vs.* Ag/AgCl) at a scan rate of 0.05 V $s^{-1}$. The incident photon-to-current conversion efficiency (IPCE) of the photoelectrodes were tested at 1 V (*vs.* Ag/AgCl) bais potential using a 300 W xenon lamp with a monochromator. The electrochemical impedance spectroscopy (EIS) was carried out at a bias potential of 0 V and the frequency range is $10^5 \sim 10^{-2}$ Hz. With an AC voltage magnitude of 5 mV, using 12 points/decade, the EIS data were simulated and analyzed by ZsampWin software. Mott-Schottky plots were measured at the potential range of -0.5 V ~ 1.0 V and the frequency of 1000 Hz with an AC voltage magnitude of 10 mV.

### §3.2.4. Calculation details

All the calculations were performed with Perdew–Burke–Ernzerhof functional (PBE) within the generalized gradient approximation (GGA), in which the $DMol^3$ module package in Materials Studio was used.[47] The valence orbitals of the atoms were described by setting the double-numeric-quality basis set with polarization functions (DNP) and the core electrons were substituted by DFT semi-core pseudopotentials (DSPPs). Among the two exposed surfaces of (020) and (200) **(Figure 1D and 1E)** of the monoclinic clinobisvanite $BiVO_4$, (020) surface was found to be the active surface. [45] To model the clinobisvanite $BiVO_4$ (020) surface, a two-layer p(1×1) slab corresponding to 8 $BiVO_4$ unit cell (48 atoms) was used, in which a vacuum layer of 15Å was applied. Atomic positions were relaxed until the energy change was less than $2.0\times10^{-5}$ Ha/atom, the residual force was less than 0.004 Ha/Å, and the maximum displacement was less than 0.005 Å.

## §3.3. Results and Discussion

### §3.3.1. Crystal structure and morphology

Figure 3-2A presents the large angle XRD results of BiMoVO and -0.8-BiMoVO thin film growth on FTO substrate. BiMoVO shows a typical monoclinic phase of $BiVO_4$ (JCPDS No. 04-010-5713), indicating that the crystal structure of BiMoVO thin film has not changed after Mo doping. Figure 3-2B shows the small-angle diffraction XRD results of BiMoVO and -0.8-BiMoVO thin film. From this result, we can find that the diffraction peak of BiMoVO at 2θ = 29.34° is moved to smaller angle after reducing at -0.8 V for 5 Min. This phenomenon indicates that the crystal distorted by the constant potential reduction.

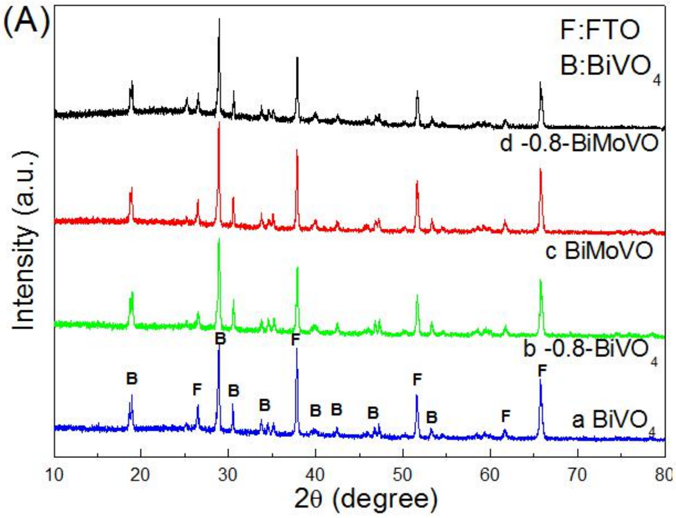

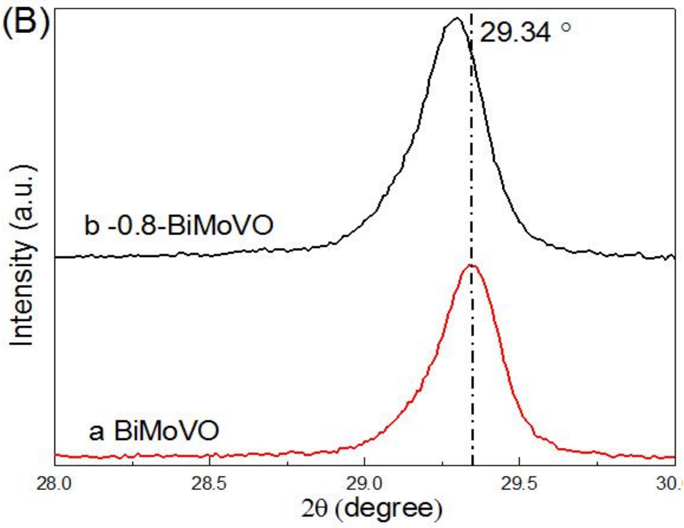

**Figure 3-2**. XRD result of (A) BiMoVO and -0.8-BiMoVO; (B) small-angle diffraction of the BiMoVO and -0.8-BiMoVO.

The SEM was employed to observe the surface morphologies of the $BiVO_4$, -0.8-$BiVO_4$, BiMoVO and -0.8-BiMoVO photoanodes, and the results were shown in Figure 3-3A to 3-3D. As presented in these figures, all thin films show porous structure, which can provide sufficient surface activity sites for the water PEC splitting reaction. Compared with the four SEM images, there is no obvious difference on the morphology, indicating that both Mo doping and constant potential reduction cannot change the mesoporous structure of the photoanode thin film.

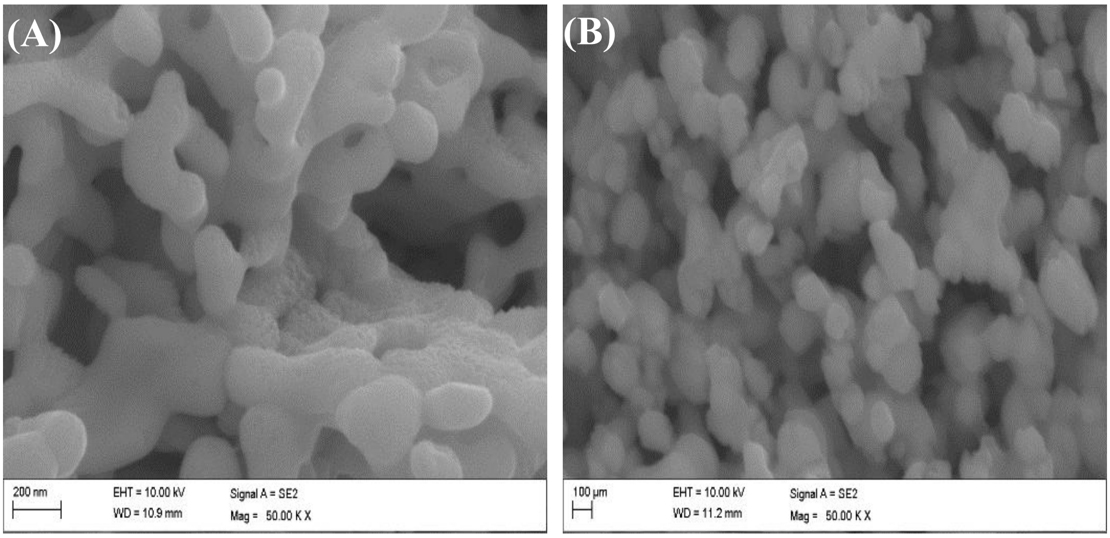

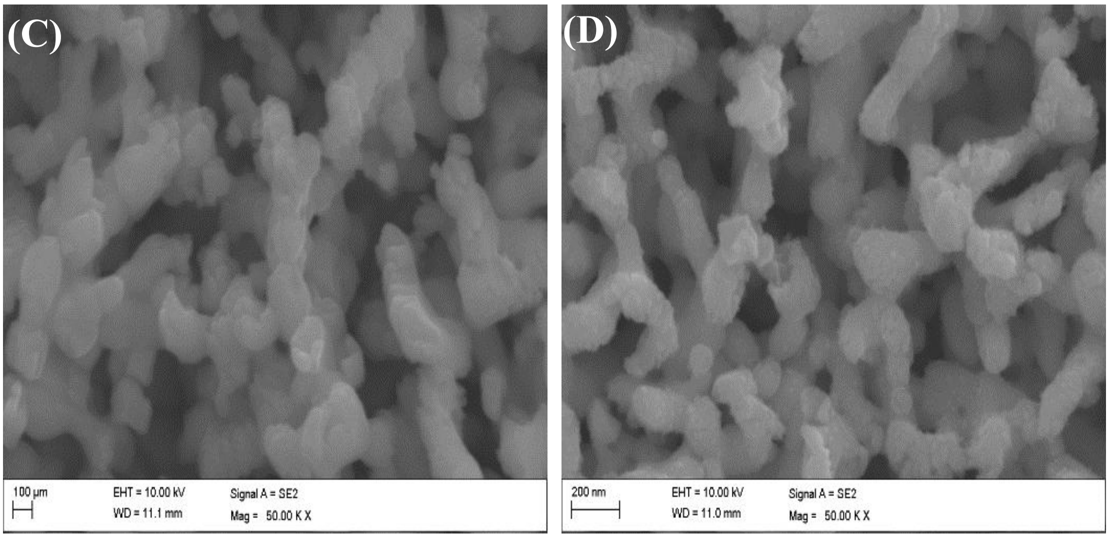

**Figure 3-3.** SEM images of (A) $BiVO_4$, (B) -0.8-BiVO, (C) BiMoVO, (D) -0.8-BiMoVO.

**Figure 3-4** shows the cross-section SEM image of -0.8-BiMoVO thin film, we can find that a thin film with a thickness of 500 nm covered on the surface of FTO. In order to clarify the surface situation more clearly before and after electrochemical reduction of these two samples, the TEM technique was used to observe them further.

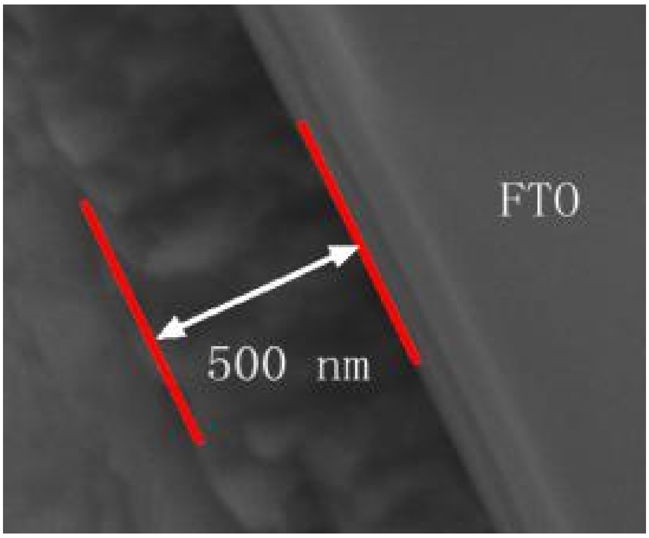

**Figure 3-4.** Cross-section SEM of the -0.8-BiMoVO thin film growth on FTO.

Figure 3-5A and Figure 3-5B show the low resolution TEM of BiMoVO and -0.8-BiMoVO particles respectively. As shown in these two TEM images, some BiMoVO nanoparticles homogeneous distribute on the surface of larger BiMoVO particles. However, on the low resolution TEM images, there is no nanostructure morphology difference. So the high resolution TEM (HRTEM) technology should be employed to observe the nanostructure of BiMoVO and -0.8-BiMoVO further.

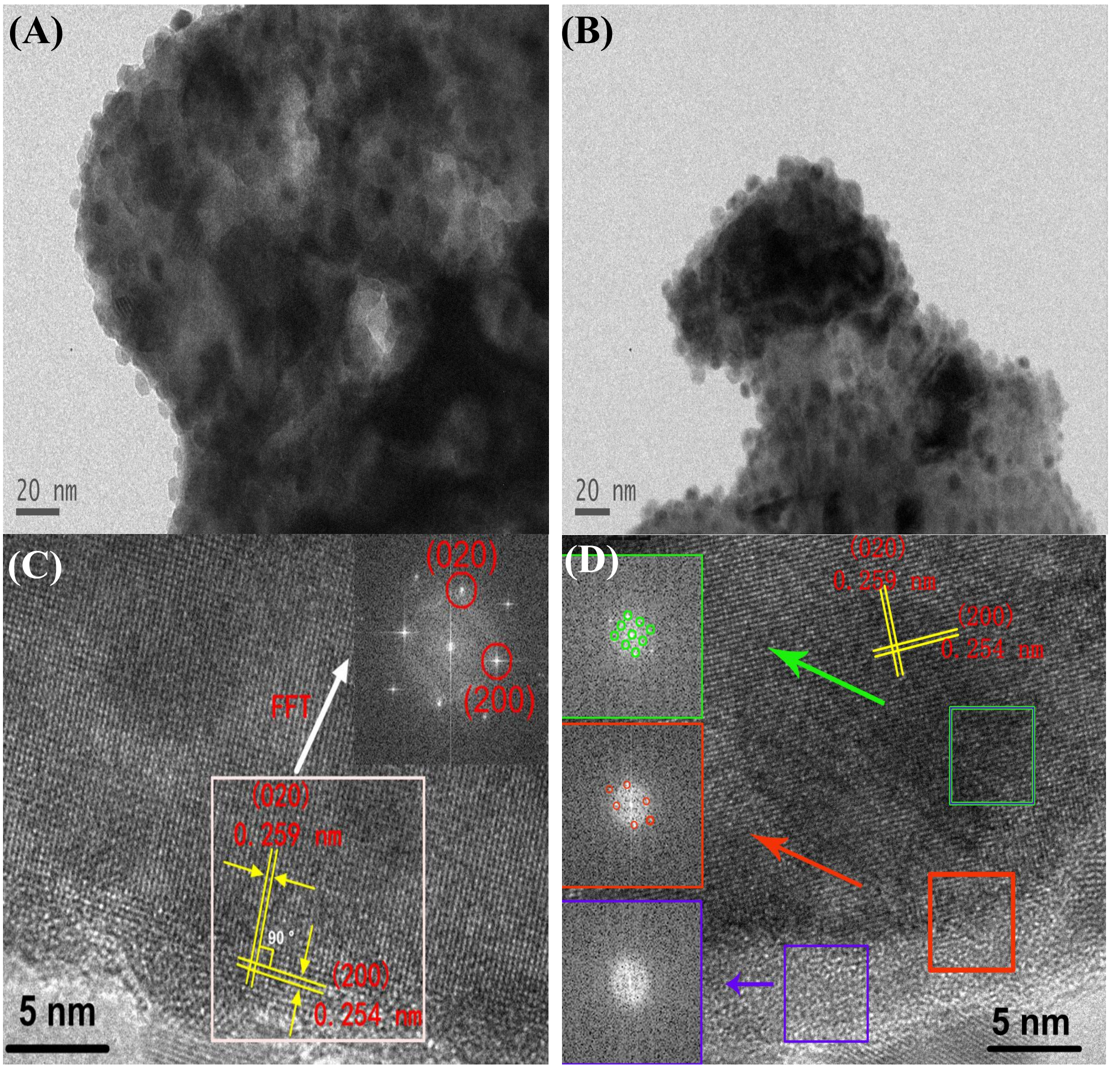

**Figure 3-5.** Low resolution TEM of (A) BiMoVO and (B) -0.8-BiMoVO; High resolution TEM of (C) and (D). The FFT ED patterns of BiMoVO and -0.8-BiMoVO are inserted in (C) and (D), respectively.

The corresponding HRTEM images of these two samples are presented in Figure 3-5C and 3-5D. As shown in Figure 3-5C, two perpendicular lattice fringes with d-spacing of 0.259 nm and 0.254 nm are noted. They are consistent with BiVO$_4$ (020) and (200) planes of reference (JCPDS no. 04-010-5713). A corresponding FFT-ED pattern (Inset in Figure 3-5C) generated by HRTEM image could be indexed to the (020) and (200) planes of the monoclinic BiMoVO. The HRTEM image of -0.8-BiMoVO is shown in Figure 3-5D. After electrochemical reduction at -0.8 V, the two perpendicular lattice fringes corresponding to (020) and (200) facets can be observed also. The FFT transformation method was employed to analyze the surface (blue area), interface (red area) and bulk (green) of this particle. After FFT transformation, the surface layer presents an amorphous structure. At the interface, the crystallinity of this area is increased obviously. In the bulk, compared with the interface area, the crystallinity enhanced further. This phenomenon indicated that an amorphous layer with a thickness ~5 nm is coated on the surface of -0.8-BiMoVO particle, and the crystallinity of -0.8-BiMoVO particle is increased gradually from the surface to the bulk. So, it means that the electrochemical reduction process can damage the structure of the surface crystal planes of (020) or (200) facets, most possibly the (020), a widely considered highly active crystal plane of $BiVO_4$.[18-20] Furthermore, as shown in Figure 3-6, the exposed (200) has been evaluated. To this facet, optimization calculations indicated that it is a very stable surface with nearly no obvious structure changes, which can be attributed to the nature of nearly all metal atoms terminated surface. This facet is difficult to be influenced during electrochemical reduction, so it is not considered too much.

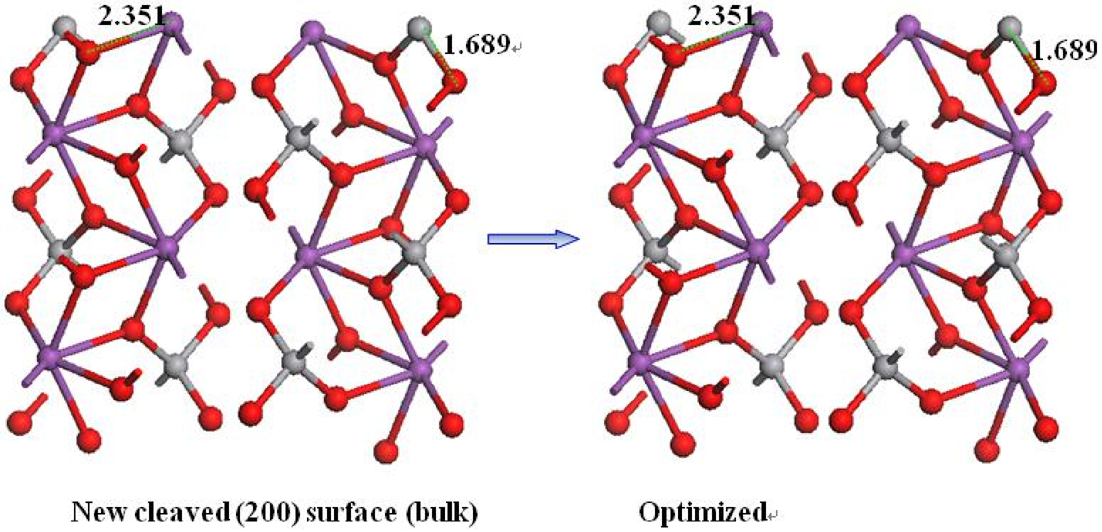

**Figure 3-6.** $BiVO_4$ (200) surface new cleaved (bulk) and optimized. The red, oxygen; grey, vanadium; purple, bismuth.

### §3.3.2. PEC performances and optical characters

Then the PEC performances property of $BiVO_4$, -0.8-$BiVO_4$, BiMoVO, -0.8-BiMoVO photoanodes would be investigated, the corresponding results are shown in Figure 3-7. Figure 3-7A and 3-7B present the photoinduced I-V curves and photoinduced I-t curves of $BiVO_4$ and -0.8-$BiVO_4$ photoanode. From the photoinduced I-V curves results (Figure 3-7A) we can find that with the scanning potential increasing from -0.4 V to 1.5 V, both photocurrents of $BiVO_4$ and -0.8-$BiVO_4$ photoanodes are increased gradually. However, after constant potential reduction, the -0.8-$BiVO_4$ photoanode achieved a 1.4 mA/cm$^2$ photocurrent density when the applied bias potential arriving 1.5 V, which value is 1.75 times higher than that of the $BiVO_4$ photoanode under the same test conditions. Figure 3-7B presents the photoinduced I-t curves of $BiVO_4$ and -0.8-$BiVO_4$ photoanodes. The photogenerated current density of -0.8-$BiVO_4$ photoanode is near 0.8 mA/cm$^2$ (bias potential is 1 V vs Ag/AgCl) after three cycles light on and cut off, but the $BiVO_4$ photoanode shows a 0.42 mA/cm$^2$ photocurrent density at the same test condition. This phenomenon demonstrates that the PEC performance of pure $BiVO_4$ can be improved by the constant potential reduction at -0.8 V.

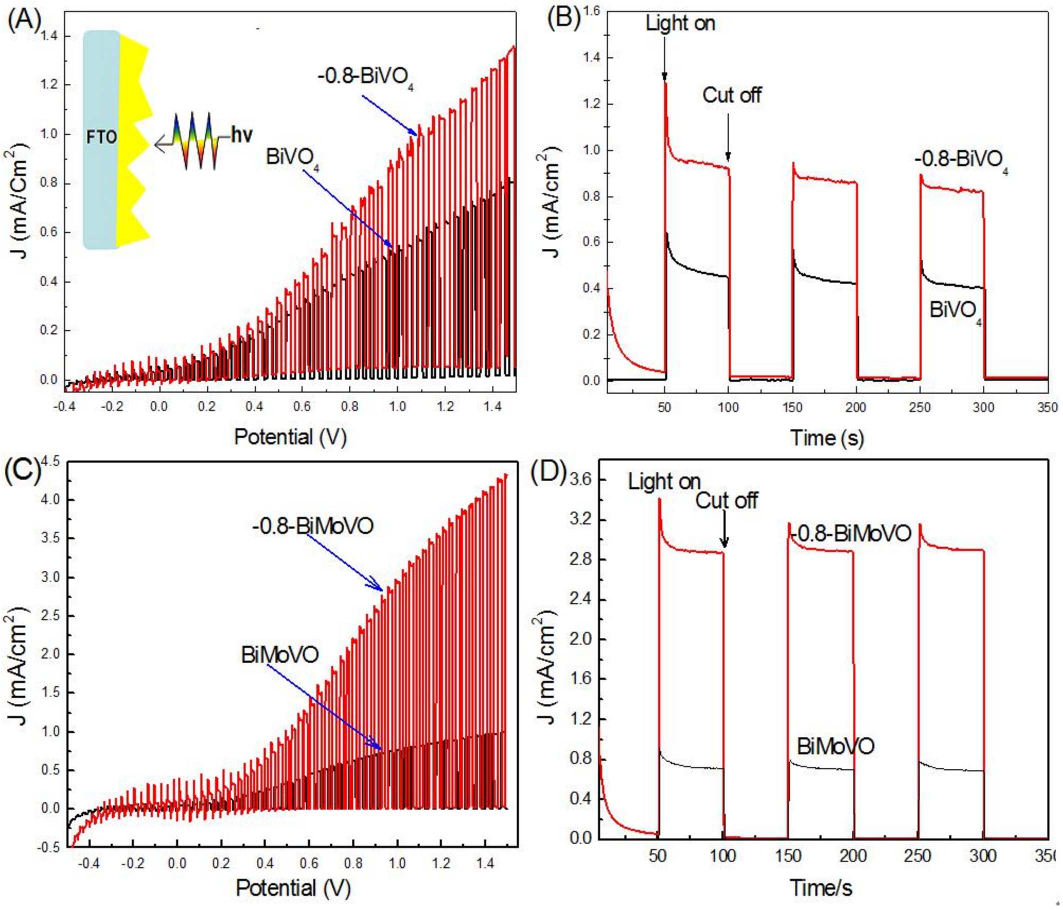

**Figure 3-7.** (A) and (B) photoinduced I-V curves and photoinduced I-t curves of $BiVO_4$ and -0.8-$BiVO_4$ photoanodes, respectively; (C) and (D) photoinduced I-V curves and photoinduced I-t curves of BiMoVO and -0.8-BiMoVO photoanodes, respectively. All samples were tested under AM 1.5 G (100 mW/cm$^2$) illumination, in 0.1 M $Na_2SO_4$ electrolyte.

Figure 3-7C and 3-7D show the photoinduced I-V curves and photoinduced I-t curves of BiMoVO and -0.8-BiMoVO photoanodes. The photoinduced I-V curves results of these two photoanodes are showed in Figure 3-7C. We can find that with the scanning potential increasing from -0.4 V to 1.5 V, both photocurrents of BiMoVO and -0.8-BiMoVO photoanodes are increased. However, the -0.8-$BiVO_4$ photoanode is increased sharply when the bias potential exceeding 0.2 V, and achieves a 4.3 mA/cm$^2$ photocurrent density when the applied bias potential arriving 1.5 V, which value is near 4.3 times higher than that of the $BiVO_4$ photoanode under the same test conditions. Figure 3-7B presents the photoinduced I-t curves of BiMoVO and -0.8-BiMoVO photoanodes. The photogenerated current density of -0.8-$BiVO_4$ photoanode is near 3.0 mA/cm$^2$ (bias potential is 1 V vs Ag/AgCl) after three cycles light on and cut off, but the $BiVO_4$ photoanode shows a 0.7 mA/cm$^2$ photocurrent density at the same test condition. Compared with the above PEC performances results, we can accept the information that the PEC performance improving effect on BiMoVO photoanode by constant potential reduction is much higher than that of $BiVO_4$ photoanode. Thus, in the next section, the BiMoVO photoanode was selected to investigate carefully.

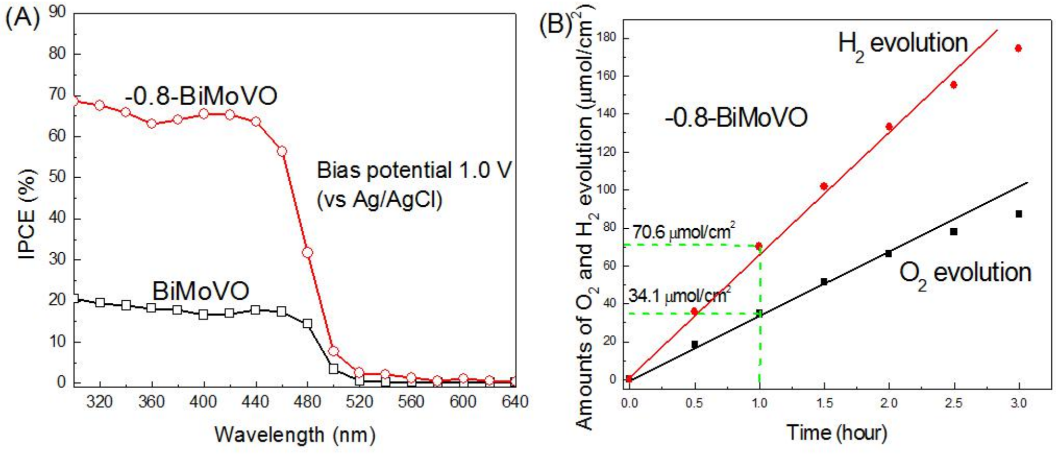

**Figure 3-8.** (A) IPCE results of BiMoVO and -0.8-BiMoVO photoanode, (B) PEC water splitting for hydrogen and oxygen evolution performance of -0.8-BiMoVO, tested under AM 1.5 G (100 mW/cm$^2$) illumination, in 0.1 M $Na_2SO_4$ electrolyte, bias potentiao 1.0 V (vs. Ag/AgCl).

The IPCE values of BiMoVO and -0.8-BiMoVO photoanode was tested by monochromatic light (from 300 nm to 640 nm) stimulating, and the results shown in

Figure 3-8A. At the range of the incident light wavelength shorter than 440 nm, all the IPCE values of -0.8-BiMoVO photoanode higher than 60 %, but in the same area, the BiMoVO photoanode is near 20 %. When the incident light wavelength exceeding 440 nm, IPCE value of both photoanodes are reduced dramatically, and terminated at 520 nm. The PEC water splitting for hydrogen and oxygen evolution performance of -0.8-BiMoVO photoanode is showed in Figure 3-8B. The total test time was 3 hours. In the first one hour, the oxygen and hydrogen evolution amounts are 34.1 and 70.6 μmol/cm$^2$, respectively, the proportion of the oxygen and hydrogen amount is near 1:2, which value very approaches to the theoretical proportion of the water splitting, indicating the water was decomposed completely by the PEC process of the photoanode. However, both the oxygen and hydrogen evolution amount points are non-linear in 3 hours, this phenomenon indicated that the PEC performance of -0.8-BiMoVO is not so stable during working process.

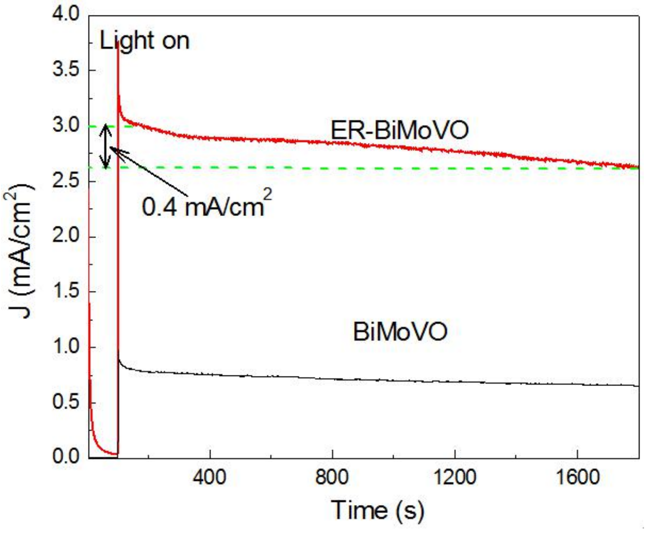

**Figure 3-9.** photocurrent stability of BiMoVO and -0.8-BiMoVO photoanode.

The PEC performance stabilities of BiMoVO and -0.8-BiMoVO photoanode are showed in Figure 3-9, the photocurrent density of BiMoVO photoanode is relatively low, and shows a high stability. For the -0.8-BiMoVO photoanode, the photocurrent density is much higher than the former one. However, the photocurrent density decreased 0.4 mA/cm$^2$ in 30 Min continual illumination, indicating that the reduced surface of BiMoVO by electrochemical method should be modified by other surface passivation layer.

Figure 2E presents the UV-Vis DRS curves of these photoanodes. Compared with the BiMoVO thin film, the absorption threshold of -0.8-BiMoVO thin film blue shift to near 496 nm, indicating that the reduced BiMoVO layer which covered on bulk surface, possess larger bandgap (2.5 eV) than the bulk BiMoVO. So, the increased PEC property did not contributed to enhancing the photon absorption range, but other reasons instead.

The PL results of BiMoVO and -0.8-BiMoVO photoanodes are shown in Figure 2F. As shown in this figure, there are two main peaks on the both curves, which result similar to the Shan's work.[42] The peak near 500 nm is the main PL peak for $BiVO_4$, and the peak present at 442 nm induced by the new energy level introducing by VIB subgroup elements doping. PL peak intensity of BiMoVO photoanode is dramatically quenched after electrochemical reduction. As we know, electron diffusion distance is an important parameter which inverse ratio to the PL intensity. It means that the longer the electron diffusion distance of a photoanode thin film, the higher the photogenerated electron lifetime. Furthermore, the electron diffusion distance of a photoanode is proportional to the free charge density of it. Thus, due to the results of PL, we can get information that electrochemical reduction treatment at -0.8 V may increase the free charge density of the BiMoVO photoanode.

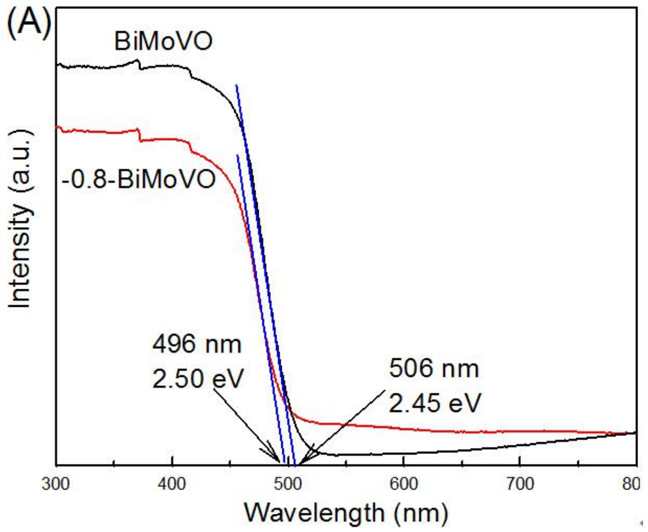

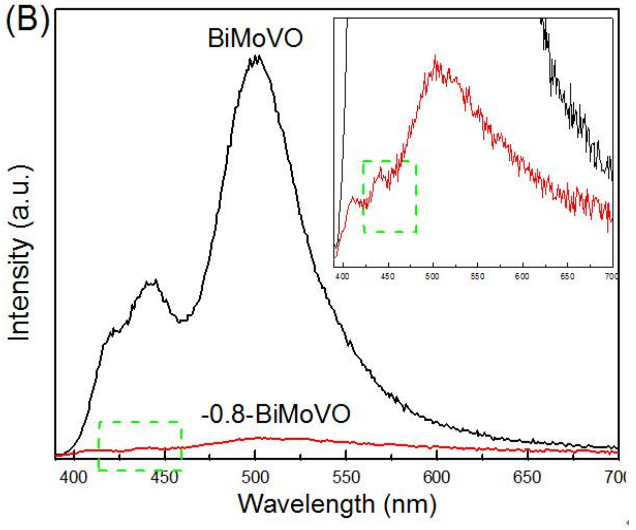

**Figure 3-10.** the UV/Vis diffuse reflectance spectra (DRS) and photoluminescence (PL) spectra of BiMoVO and -0.8-BiMoVO photoanode thin film (Insert is the zoomed PL spectrum of -0.8-BiMoVO).

### §3.3.3. Electrochemical behavior analysis

Thus, in order to clarify why the PEC performance of BiMoVO photoanode improved after electrochemical reduction at -0.8 V, the Mott-shottcky plots and EIS electrochemical techniques were employed to test and the results and data analysis is shown in Figure 3-11.

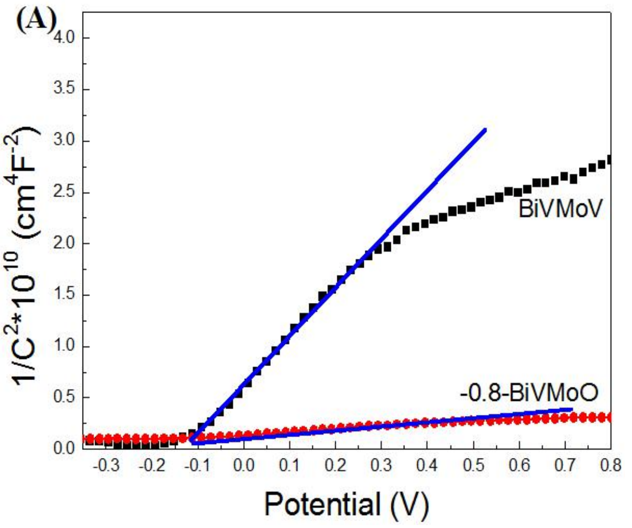

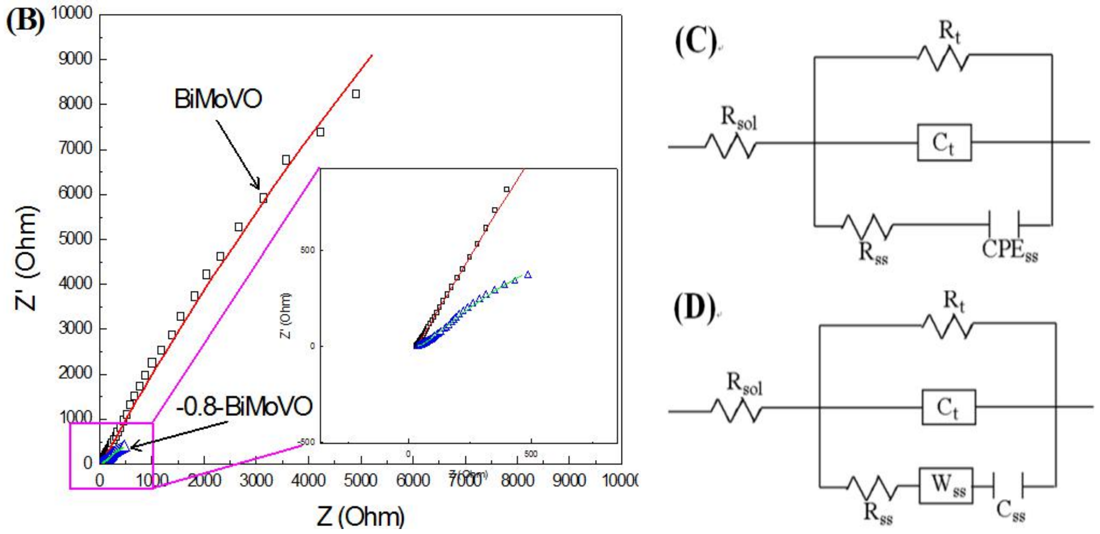

**Figure 3-11.** (A) Mott-shottky plots and (B) EIS curves of BiVMoO and -0.8-BiVMoO photoanodes in 0.1 M $Na_2SO_4$ electrolyte. (C) is the fit circuit for the BiVMoO EIS curve; (D) is the fit circuit for -0.8-BiVMoO EIS curve.

Mott-Schottky plots can be used to study the relation between the applied potential and the space charge region capacitance. The specific formula express is as follows:

$$1/C^2 = 2 (e\varepsilon\varepsilon_0 N_D)^{-1} \cdot (E - E_{fb} - \kappa T/e) \tag{3-1}$$

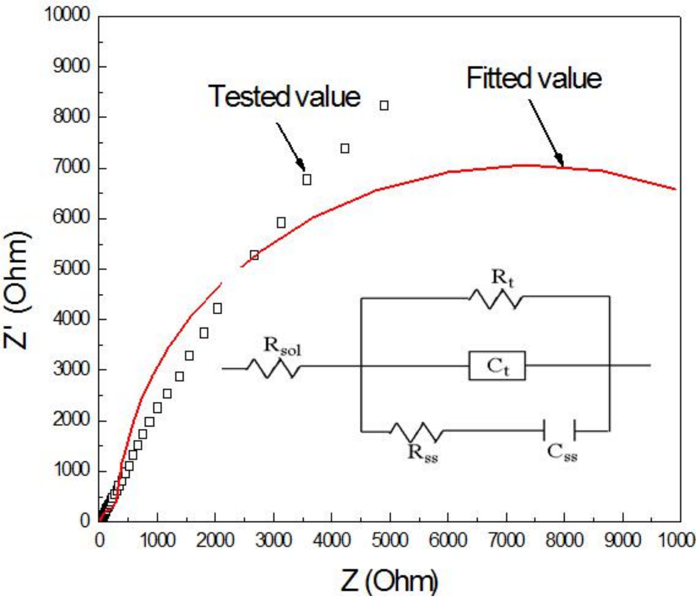

**Figure 3-12**. The EIS result of BiMoVO photoanode fitted as the insert electric circuit.

where C is the space charge region capacitance; e is the elemental charge, $\varepsilon_0$ is the permittivity of free space, $\varepsilon$ is the relative permittivity of the semiconductor, $N_D$ is the free charge density, E is the applied potential, $E_{fb}$ is the flat band potential, κ is the Boltzmann constant and T is the temperature. From formula (3-1), we can find that free charge density is inverse ratio to the slope along the straight part of the curve. However, In this case, both photoanodes are not perfect planar, thus, we cannot calculate the density of the free carriers quantificationally, but only evaluation the change tendency of the free carrier carriers on the photoanode qualitatively. [43, 44] So, from Figure 3-11A, we can find that compared with BiMoVO photoanode, the slope of -0.8-BiMoVO photoanode dramatically decrease to near zero, this phenomenon directly indicates that the free charge density of -0.8-BiMoVO photoanode is increased largely by the electrochemical reduction at -0.8 V.

EIS technique was employed to research the electrochemical property of these two photoanodes. There are two key characteristics of the photoanode thin film to decide its PEC performance. One is the electron transfer resistance of the thin film, and the other one is the semiconductor-electrolyte interface electron exchange resistance. The former one decided the photogenerated charge diffusion distance in the semiconductor thin film, and the latter one decided the interface electrochemical reaction energy barrier of the photoanode. The corresponding results are showed in Figure 3-11B to 3-11D. As shown in Figure 3-11B, compared with the BiMoVO photoanode, the impedance arc of -0.8-BiMoVO photoanode decreased dramatically. Because of the huge change of the EIS data, different fit circuits should be employed to simulate the BiMoVO and -0.8-BiMoVO photoanodes. The corresponding fit circuits and fit data are shown in Figure 3-11C and 3-11D respectively. In Figure 3-11C, $R_{sol}$ was the solution resistance; $R_t$ and $C_t$ were the electron transfer resistance and capacitance of the photoanode thin film; $CPE_{ss}$ was constant phase angle element (If replaced the $CPE_{ss}$ by a pure capacitance $C_{ss}$, as shown in Figure 3-12, the fit would be faulted). $R_{ss}$ was used to describe the charge transfer resistance between the semiconductor and the electrolyte interface. This fit circuit shows a good simulation of the EIS curve of BiMoVO photoanode (As show in Figure 3-11B, the measured data are marked by hollow symbols, while, the solid lines are the fitted curves using the fit circuit which provided in Figure 3-11C).

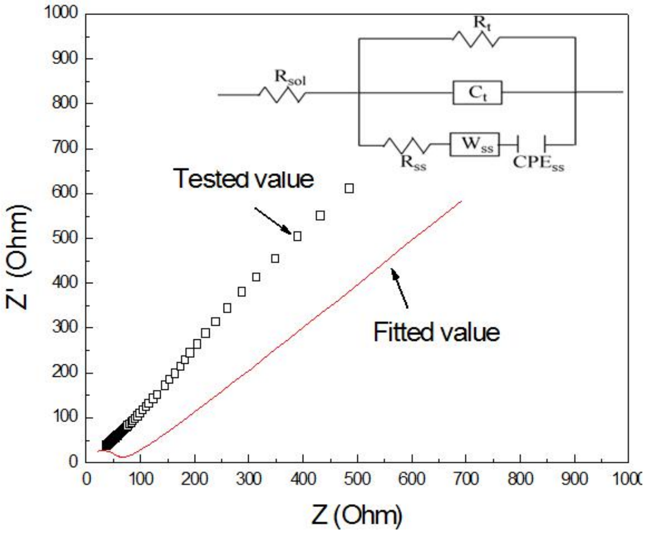

**Figure 3-13**. The EIS result of -0.8-BiMoVO photoanode fitted as the insert electric circuit.

**Table 1.** Fitted parameters of the EIS of BiMoVO and -0.8-BiMoVO photoelectrodes base on the circuits showed in Figure 3-11C and 3-11D.

| Sample | BiMoVO | -0.8-BiMoVO |
|---|---|---|
| $R_{sol}$ (Ω $cm^2$) | 28.90 | 38.60 |
| $R_t$ (Ω $cm^2$) | $1.34\times10^5$ | $1.69\times10^3$ |
| CPE ($Ω^{-1}$ $cm^2$ sn) | $1.25\times10^{-2}$ | - |
| $C_t$ (F $cm^{-2}$) | $3.86\times10^{-6}$ | $8.71\times10^{-6}$ |
| $C_{ss}$ (F $cm^{-2}$) | - | $6.771\times10^{-3}$ |
| $R_{ss}$ (Ω $cm^2$) | 11.53 | 10.99 |
| $W_{ss}$ (Ω $cm^2$) | - | $2.34\times10^{-3}$ |

Table 1 shows the corresponding fit data, in which two key parameters $R_t$ and $R_{ss}$ are $1.34 \times 10^5$ and 11.53 Ω/cm$^2$, respectively. Figure 3-11D presents the fit circuit and fit data of -0.8-BiMoVO photoanode. Compared with Figure 3-11C, a pure $C_{ss}$ was used to replace $CPE_{ss}$ (In this case, as shown in Figure 3-13, if use $CPE_{ss}$ to replace $C_{ss}$, the fit data would be faulted), and a Warburg element ($W_{ss}$) was added at the interface of semiconductor and electrolyte. The reason introduce $W_{ss}$ in the fit circuit is that as show in Figure 3-11B, the EIS arc was decreased greatly after electrochemical reduction, meaning a strong charge exchange happened at the interface of semiconductor and electrolyte. In this case, a concentration polarization could not be ignored, so a $W_{ss}$ introduced. As shown in Table 3-1, the $R_t$ and $R_{ss}$ are $1.69 \times 10^3$ and 10.99 Ω/cm$^2$, respectively. Comparing these values with the BiMoVO photoanode, we could found that the $R_t$ of -0.8-BiMoVO photoanode decreased near

1000 orders of magnitude than that of BiMoVO photoanode. Meanwhile, $R_{ss}$ of the two photoanodes almost remains the same, indicating that the charge transfer capacity of BiMoVO photoanode can be improved greatly by reducing at -0.8 V.

Figure 3-14 presents the photoinduced I-V curves about BiMoVO photoanodes with different electrochemical reduction potentials. Compared with the BiMoVO photoanode (Figure 3-7C), the photocurrent density of -0.6-BiMoVO photoanode did not increase, indicating that the surface state of -0.6-BiMoVO photoanode did not change after this potential treatment. However, with the electrochemical reduction potential enhance to -0.8 V, the photocurrent density of the -0.8-BiMoVO photoanode increased greatly. Further increasing the reduction potential to -1 V, the photocurrent density decreased a little. It is worth noting that when the reduction potential increased to -1.2 V, its photocurrent density decreased dramatically. It is well known that the surface bond states of the $BiVO_4$ would be changed by applying reduction energy.[29-32] Thus, combining the HRTEM images showed in Figure 3-5C and 3-5D, we speculated that the bond states on the (020) facet of BiMoVO have been evolved differently with the electrochemical reduction energy increasing gradually. Thus, we employed XPS method to clarify the relevance between the bond state of BiMoVO and the electrochemical reduction potentials.

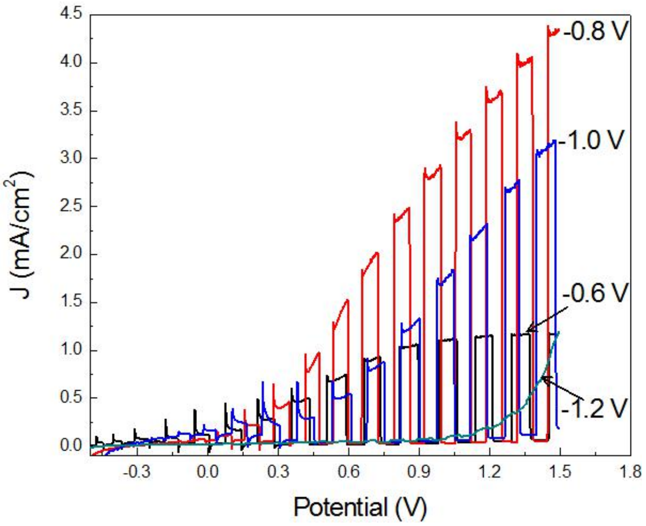

**Figure 3-14.** Photoinduced I-V curves of BiMoVO photoanodes which treated by different reduction potential at -0.6 V, -0.8 V, -1.0 V and -1.2 V, respectively

### §3.3.4. Analysis of the oxygen vacancy states

Figure 3-15 shows the $Bi_{4f}$, $V_{2p}$, $Mo_{3d}$, and $O_{1s}$ XPS results on the samples of BiMoVO, -0.8-BiMoVO and -1.2-BiMoVO, respectively.

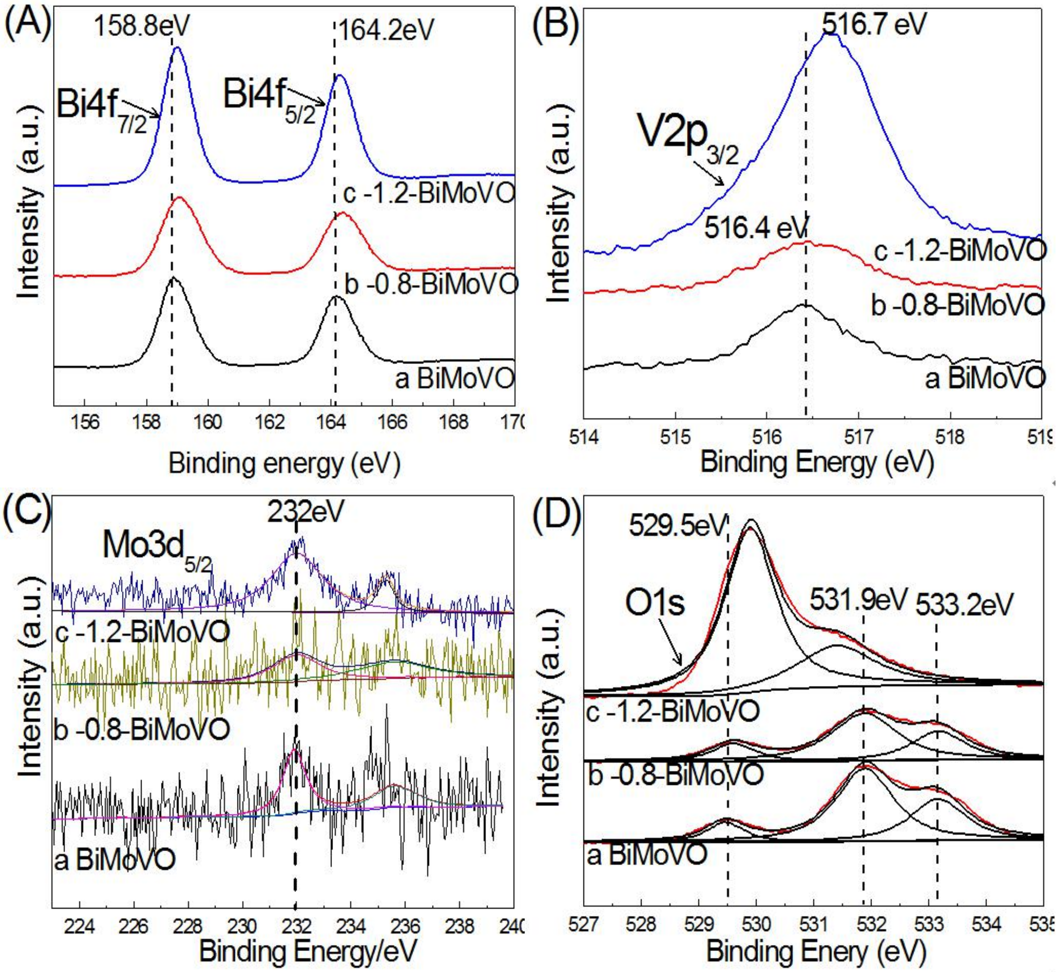

**Figure 3-15.** High resolution XPS of the elements on BiMoVO, -0.8-BiMoVO and -1.2-BiMoVO thin film, (A) $Bi_{4f}$; (B) $V_{2p}$; (C) $Mo_{3d}$; (D) $O_{1s}$.

Figure 3-15A shows the typical XPS $Bi_{4f}$ core states of these three photoanodes. It exhibits two binding energy of BiMoVO at 158.8 eV and 164.2 eV correspond to the Bi $4f_{7/2}$ and Bi $4f_{5/2}$, respectively. By comparison, these peaks are shifted to higher energy after electrochemical reduction. For a metal atom, the XPS binding energy proportional to the density of outer electrons. Usually, oxygen atom is much more electrophilic than metal atoms, so with the metal-O bands formation, the outer electrons on metal will transfer to oxygen. However, with the metal-O bands cracking, the outer electrons density on metal atom will increase, resulting in the XPS binding energy move to higher level. In this case, the XPS binding energy of Bi moved to higher level after electrochemical reduction, indicating that the Bi-O bonds on

-0.8-BiMoVO and -1.2-BiMoVO photoanodes both cracked. Figure 3-15B presents the $V_{2p}$ XPS results about these three samples. For the samples of BiMoVO and -0.8-BiMoVO, the $V_{2p}$ XPS peaks locate at 516.4 eV, meaning that the state of V-O bonds was not changed after treated by a -0.8 V reduction potential. However, the corresponding peak of -1.2-BiMoVO shifts to 516.7 eV, indicating that V-O bonds cracked on -1.2-BiMoVO. From the above result, we can conclude that a quasi-oxygen vacancy (Only Bi-O bond cracked) formed on the surface of -0.8-BiMoVO photoanode, but a real oxygen vacancy (Both Bi-O and V-O bonds cracked) formed on the surface of -1.2-BiMoVO photoanode.

The XPS result of $Mo_{3d}$ is shown in Figure 3-15C, in which because of the low content of Mo element on these three photoanode, the corresponding peaks are weak. However, these three peaks all keep at 232.0 eV, meaning that the Mo-O bonds were not cracked with the electrochemical reduction potential increasing.

Figure 3-15D presents the XPS peaks of O 1s. It is shown that for the sample of BiMoVO, the O 1s core can be split into three peaks, 529.5 eV, 531.9 eV and 533.2 eV, which represented the lattice oxygen, surface hydroxide and surface adsorb water, as previously reported. [16, 21] The peaks located at 529.5 eV of BiMoVO shifted to the higher energy direction after electrochemical reduction at -0.8 V and -1.2 V, meaning that the state of metal-oxygen bonds in the of -0.8-BiMoVO and -1.2-BiMoVO crystals were changed. Meanwhile, $O_{1s}$ on the surface of -1.2-BiMoVO just can split into two peaks, including lattice oxygen and surface hydroxide. The concentrations of surface hydroxide radicals and surface adsorbed water on the surface of -1.2-BiMoVO decrease dramatically, which phenomenon provides an evidence for real oxygen vacancy formation on it. So, combining of the PEC performance and XPS results, we can confirm that oxygen vacancy is not a positive factor to improve the PEC performance of BiMoVO photoanode, but quasi-oxygen vacancy forming on the surface of the active facet is more efficient. This result is different with previous report by Luo etc.[32]. At that case, they claimed that the pretreatment (electrochemical reduction) makes some $Mo^{6+}$ are reduced and dissolved in to electrolyte that to increase the PEC performance of BiMoVO photoanode. So, in this case, we have prepared pure $BiVO_4$ by the same experimental steps with BiMoVO photoanode, and reduction it under -0.8 V for 5 Mins (-0.8-$BiVO_4$) also. The corresponding PEC performance results show in Figure 3-7A and 3-7B. From this resuls, it can be found that compared with pure $BiVO_4$ photoanode, the -0.8-$BiVO_4$ photoanode presents a much higher photocurrent and smaller EIS arc (shown in Figure 3-16), these phenomenons are very similar to the sample of BiMoVO. However, there is not Mo element in the pure $BiVO_4$ photoanode, meaning that Mo element is not the main reason to influence the PEC performance of BiMoVO photoanode after constant potenial reduction. In Lou's work,[32] they found that the Bi 4f peak and V 2p peak are shifted to the lower binding energy. However, in our work, as shown in Figure 3-15, the Bi 4f peak and V 2p peak are shifted to the higher binding energy, meaning that the PEC improving mechanism in our work is different with Luo's work. This difference may be induced by the different electrochemical reduction methods. In Luo's work, the oxygen vacancy was not easy to be formed on the surface of Mo-doped $BiVO_4$, because of the CV reduction method not only provide negative potential to reduce the photoanode, but also provide a positive potential to oxide it. In our case, the oxygen vacancy has sufficient condition to form under persistent negative potential reduction.

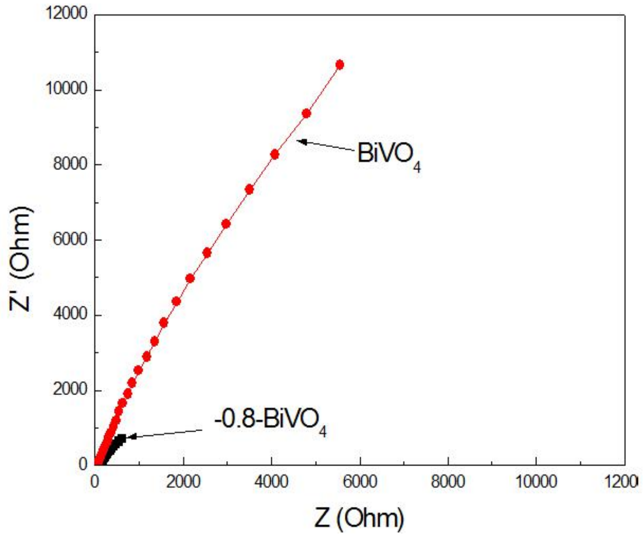

**Figure 3-16.** EIS curves of pure $BiVO_4$ and -0.8-$BiVO_4$ photoanodes.

### §3.3.5. Theoretical calculation

The DFT calculation was employed to research the characteristics change relative to the different surface situations of BiMoVO further. As we know, (020) is the high active facet of $BiVO_4$, and we can observe the (020) on the surface of BiMoVO by HRTEM showed in Figure 3-5D clearly. So, we calculated the (020) surface of monoclinic $BiVO_4$ firstly. The results (Figure 3-17A) show that, structurely, on the (020) surface of monoclinic $BiVO_4$, the bulk three-fold coordinated oxygen atoms (one O atom with two Bi and one V bonded together) of $O_{3c1}$ and $O_{3c2}$ have changed into one-fold coordinated surface ones of $O_{1c1}$ and $O_{1c2}$ after surface stabilization. The Bi-O distances are elongated up to 3.479 Å level much larger than that of the bulk one (2.351 Å). It means that the appearance of the highly active (020) surface will bring large distortion to the material and drastically Bi-O bonds broken. Each of the oxygen atoms have two Bi-O bonds broken, with only one V-O bond left. And they were changed from $O_{3c}$ into $O_{1c}$. The reduction of surface occurred. This result is consistent with the surface segregation of oxygen vancancy on the monoclinic $BiVO_4$.[35] And it is also consistent well to the experimental findings of Bi-O bonds broken in the XPS (Figure 3-15A) measurements. These can be the inherent reasons of the largely enhanced conductivity of the photoanodes displayed in the Mott-Schottky plots (Figure 3-11A) and EIS curves (Figure 3-11B). The 5 nm disorder layer observed in TEM (Figure 3-5D) can be attributed to the surface reduction, too. And the largely conversion of the material conducticity can also be read from the density of states of the system (Figure 3-17B and 3-17C).

Figure 3-17B and 3-17C show the total DOSs of bulk and (020) facets, respectively. The major contribution of valence band (VB) and conduction band (CB) are the same as that in bulk as earlier job described.[35] Besides, in the regions of VB (-18 to -15 eV and -10 to -8eV), the DOS of the (020) facet is more delocalized than that of bulk $BiVO_4$, which means a larger charge mobility.[45] Moreover, the upper edge of VB is becoming more smooth and the bottom of the CB is lowered somewhat than that of the bulk. All these can also contribute to a better charge mobility. Then the DOS analysis confirmed the larger charge mobility further for the (020) surface exposed $BiVO_4$ material from the microscopic electronic structure point of view. So calculation results confirmed that the experimental discovery of larger charge mobility accompanied with surface reduction by the Bi-O bond broken presented above is reasonable.

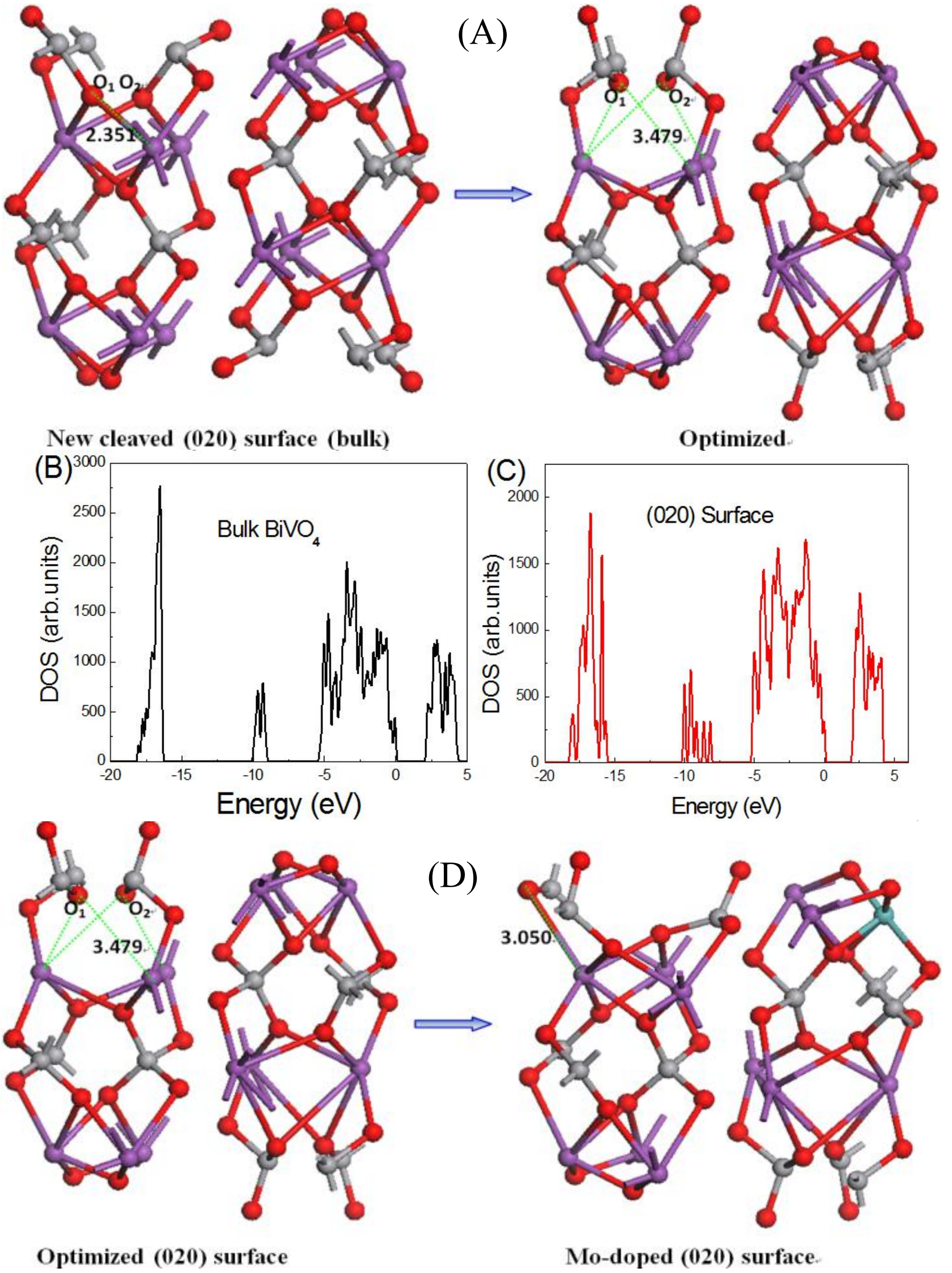

**Figure 3-17.** $BiVO_4$ (020) surface new cleaved (bulk) and optimized (The red, oxygen; grey, vanadium; purple, bismuth.) (A); The density of states of bulk $BiVO_4$ and its (020) surface show in (B) and (C); the pure and Mo-doped $BiVO_4$ (020) surface (D).

**Table 3-2**. Doping formation energy of Mo doping onto V or Bi site with different depths.

| | Depth | Mo on V site | Mo on Bi site |
|---|---|---|---|
| $E_{form}$ (eV) | First layer | -1.89 | -7.04 |
| | Second layer | -1.43 | -5.78 |

As for the Mo-doped $BiVO_4$, we found that Mo preferred to dope on Bi site on the

$BiVO_4$ (020) surface just as Ding et al ever disclosed [46] and the doping inclined to occur near the outermost surface based on doping formation energy calculation (Table 3-2). When Mo doped on Bi site, the (020) surface was found to display relatively small elongation of Bi-O bonds (Figure 3-17D), which can be said to decrease the surface reduction due to the surface stabilization somewhat. Then it can be imagined that electrochemical reduction and Mo doping can find a balance between them so that the performance of the photoanode can be adjusted to a good level.

Thus, from the above research, we indicate that oxygen vacancy on the surface of BiMoVO photoanode is a double-edged sword for the photoelectrochemical performance. It can increase the free charge density of BiMoVO, but inducing the recombiation of free photogenerated carriers. As shown in Figure 3-18, this section demostrate that quasi-oxygen vacancy forming on the surface of the BiMoVO active facet is the true reason to improve the photoelectrochemical performance of it.

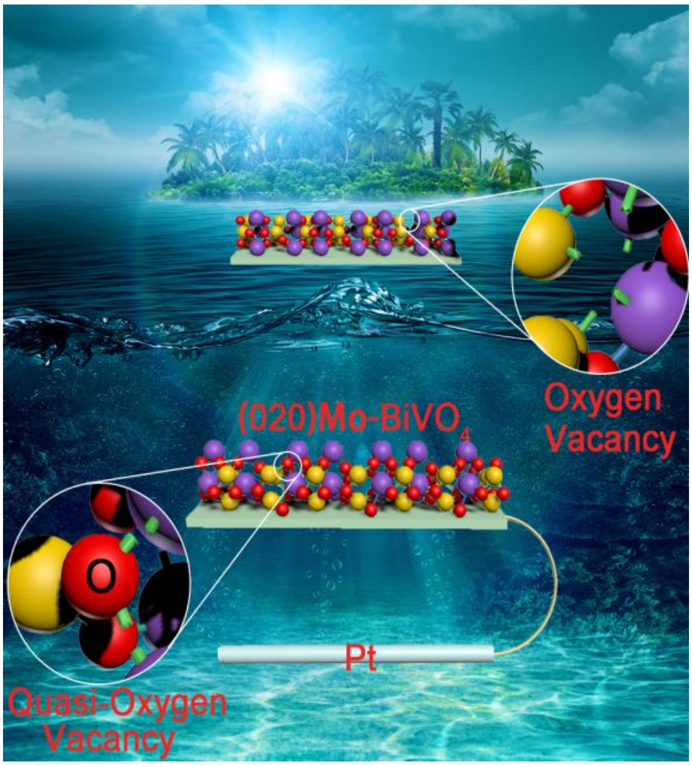

**Figure 3-18.** The function of quasi-oxygen vacancy on BiMoVO photoanode.

## §3.4. Conclusion

In this study, we prepared Mo doped $BiVO_4$ photoanode by a simple electrochemical deposition method. The surface defect state of the BiMoVO was changed along with the reduction potentials increasing. When -0.8 V applied on the BiMoVO photoanode, only the Bi-O bonds on (020) facet was broken, and quasi-oxygen vacancy formed. In this case, a 4.3 mA/cm$^2$ photocurrent density could be achieved (AM 1.5 G one sun, vs Ag/AgCl 1.5 V). With the reduction potential increased to -1.2 V, both Bi-O and V-O bonds on (020) were cracked. At this time, the oxygen vacancy formed on it. However, the corresponding PEC performance decreased dramatically. Further experimental data and DFT calculation data indicated that oxygen vacancy was not the real reason to improve the PEC performance of a BiMoVO photoanode, but just some Bi-O bonds broken on the active facet.

## §3.5. Reference

[1] W.J. Ong, L.L. Tan, Y.H. Ng, S.T. Yong and S.P. Chai, “Graphitic Carbon Nitride (g-$C_3N_4$)-Based Photocatalysts for Artificial Photosynthesis and Environmental Remediation: Are We a Step Closer To Achieving Sustainability?” *Chem. Rev,* 116, (2016) 7159.

[2] W.J. Ong, L.L. Tan, S.P. Chai, S.T. Yong and A.R. Mohamed, “Facet-Dependent Photocatalytic Properties of $TiO_2$-Based Composites for Energy Conversion and Environmental Remediation,” *ChemSusChem,* 7, (2014) 690.

[3] J. Feng, M. Gong, M.J. Kenney, J.Z. Wu, B. Zhang, Y.Li and H. Dai, “Nickel-coated silicon photocathode for water splitting in alkaline electrolytes,” *Nano Res,* 8, (2015) 1577.

[4] L.J. Guo, Y.J. Wang and T. He, “Photocatalytic Reduction of $CO_2$ over Heterostructure Semiconductors into Value-Added Chemicals,” *Chem. Rec,* 16, (2016) 1918.

[5] W.J. Ong, L.L. Tan, S.P. Chai and S.T. Yong, “Heterojunction engineering of graphitic carbon nitride (g-$C_3N_4$) viaPt loading with improved daylight-induced photocatalytic reduction of carbon dioxide to methane,” *Dalton Trans,* 44, (2015) 1249.

[6] T.W. Kim and K.S. Choi, “Nanoporous $BiVO_4$ photoanodes with dual-layer oxygen evolution catalysts for solar water splitting,” *Science*, 343, (2014) 990.

[7] J.K. Cooper, S. Gul, F.M. Toma, L. Chen, P.A. Glans, J. Guo, J.W. Ager, J. Yano and I.D. Sharp, “Electronic Structure of Monoclinic $BiVO_4$,” *Chem. Mater,* 26, (2014) 5365.

[8] S. Hu, C.X. Xiang, S. Haussener, A.D. Berger and N.S. Lewis, “An Analysis of the Optimal Band Gaps of Light Absorbers in Integrated Tandem Photoelectrochemical Water-Splitting Systems,” *Energy Environ. Sci,* 6, (2013) 2984.

[9] G. Li, D. Zhang, J.C. Yu, “Ordered mesoporous $BiVO_4$ through nanocasting: a superior visible light-driven photocatalyst,” *Chem. Mater,* 20, (2008) 3983.

[10] W.J. Jo, J.W. Jang, K.J. Kong, H.J. Kang, J.Y. Kim, H.Jun, Y. Jun and J.S. Lee, “Phosphate doping into monoclinic $BiVO_4$ for enhanced photoelectrochemical water oxidation activity,” *Angew. Chem. Int. Ed,* 51, (2012) 3147.

[11] J.H. Kim, Y. Jo, J.H. Kim, J.W. Jang, H.J. Kang, Y.H. Lee, D.S. Kim, Y. Jun and J.S. Lee, “Wireless solar water splitting device with robust cobalt-catalyzed, dual-doped $BiVO_4$ photoanode and perovskite solar cell in tandem: A dual absorber artificial leaf,” *ACS nano,* 9, (2015) 11820.

[12] Z. Jiang, Y. Liu, T. Jing, B. Huang, X. Zhang, X. Qin, Y. Dai and M.H. Whangbo, “Enhancing the Photocatalytic Activity of $BiVO_4$ for Oxygen Evolution by Ce Doping: $Ce^{3+}$ Ions as Hole Traps,” *J. Phys. Chem. C,* 120, (2016) 2058.

[13] W. Luo, Z. Yang, Z. Li, J. Zhang, J. Liu, Z. Zhao, Z. Wang, S. Yan, T. Yu and Z. Zou, “Solar hydrogen generation from seawater with a modified $BiVO_4$ photoanode,” *Energy Environ. Sci,* 4, (2011) 4046.

[14] Z. Wang, W. Luo, S. Yan, J. Feng, Z. Zhao, Y. Zhu, Z. Li and Z. Zou, “$BiVO_4$ nano–leaves: Mild synthesis and improved photocatalytic activity for $O_2$ production under visible light irradiation,” *CrystEngComm*, 13, (2011) 2500.

[15] Y. Wei, J. Su, X. Wan, L. Guo and L. Vayssieres, “Spontaneous photoelectric field-enhancement effect prompts the low cost hierarchical growth of highly ordered heteronanostructures for solar water splitting,” *Nano Res,* 9, (2016) 1561.

[16] H. Jiang, H. Dai, X. Meng, K. Ji, L. Zhang and J. Deng, “Porous olive-like $BiVO_4$: alcoho-hydrothermal preparation and excellent visible-light-driven photocatalytic performance for the degradation of phenol,” *Appl. Catal. B,* 105, (2011) 326.

[17] G. Xi and J. Ye, “Synthesis of bismuth vanadate nanoplates with exposed {001} facets and enhanced visible-light photocatalytic properties,” *Chem. Comm.,* 46, (2010) 1893.

[18] R. Li, F. Zhang, D. Wang, J. Yang, M. Li, J. Zhu, X. Zhou, H. Han and C. Li, “Spatial separation of photogenerated electrons and holes among {010} and {110}

crystal facets of $BiVO_4$," *Nat. comm.,* 4, (2013) 1432.

[19] R. Li, H. Han, F. Zhang, D. Wang and C. Li, "Highly efficient photocatalysts constructed by rational assembly of dual-cocatalysts separately on different facets of $BiVO_4$," *Energy Environ. Science*, 7, (2014) 1369.

[20] S.M. Thalluri, M. Hussain, G. Saracco, J. Barber and N. Russo, "Green-synthesized BiVO4 oriented along {040} facets for visible-light-driven ethylene degradation," *Ind. Eng. Chem. Res,* 53, (2014) 2640.

[21] J.Z. Yin, S.B. Huang, Z.C. Jian, M.L. Pan, Y.Q. Zhang, Z.B. Fei and X.R. Xu, "Enhancement of the visible light photocatalytic activity of heterojunction $In_2O_3/BiVO_4$ composites," *Appl. Phys. A,* 120, (2015) 1529.

[22] D.K. Zhong, S. Choi and D.R. Gamelin, "Near-complete suppression of surface recombination in solar photoelectrolysis by "Co-Pi" catalyst-modified W: $BiVO_4$," *J. Am. Chem. Soc,* 133, (2011) 18370.

[23] M. Zhong, T. Hisatomi, Y. Kuang, J. Zhao, M. Liu, A. Iwase, Q. Jia, H. Nishiyama, T. Minegishi, M. Nakabayashi, N. Shibata, R. Niishiro, C. Katayama, H. Shibano, M. Katayama, A. Kudo, T. Yamada and K. Domen, "Surface Modification of $CoO_x$ Loaded $BiVO_4$ Photoanodes with Ultrathin p-Type NiO Layers for Improved Solar Water Oxidation," *J. Am. Chem. Soc*,137, (2011) 5053.

[24] S.K. Pilli, T.G. Deutsch, T.E. Furtak, J.A. Turner, L.D. Brown and A.M. "Herring, Light induced water oxidation on cobalt-phosphate (Co–Pi) catalyst modified semi-transparent, porous $SiO_2$–$BiVO_4$ electrodes," *Phys. Chem. Chem. Phys,* 14, (2012) 7032.

[25] A.J.E. Rettie, H.C. Lee, L.G. Marshall, J.F. Lin, C. Capan, J. Lindemuth, J.S. McCloy, J. Zhou, A.J. Bard and C.B. Mullins, "Combined Charge Carrier Transport and Photoelectrochemical Characterization of $BiVO_4$ Single Crystals: Intrinsic Behavior of a Complex Metal Oxide," *J. Am. Chem. Soc,* 135, (2013) 11389.

[26] A.J.E. Rettie, W.D. Chemelewski, D. Emin and C.B. Mullins, "Unravelling Small-Polaron Transport in Metal Oxide Photoelectrodes," *J. Phys. Chem. Lett*, 7, (2013) 471.

[27] B. Wang, S. Shen and L. Guo, "Surface Reconstruction of Facet-Functionalized SrTiO3 Nanocrystals for Photocatalytic Hydrogen Evolution," *ChemCatChem*, 8, (2016) 798.

[28] J.K. Cooper, Y. Ling, C. Longo, Y. Li and J.Z. Zhang, "Effects of hydrogen

treatment and air annealing on ultrafast charge carrier dynamics in ZnO nanowires under in situ photoelectrochemical conditions," *J. Phys. Chem. C*, 116, (2012) 17360.

[29]G. Wang, H. Wang, Y. Ling, Y. Tang and X. Yang, "Hydrogen-treated $TiO_2$ nanowire arrays for photoelectrochemical water splitting," *Nano lett.*, 11, (2011) 3026.

[30] M. Xing, W. Fang, M. Nasir, Y. Ma, J. Zhang and M. Anpo, "Self-doped $Ti^{3+}$-enhanced $TiO_2$ nanoparticles with a high-performance photocatalysis," *J. Catal.,* 297, (2013) 236.

[31] H. Tan, Z. Zhao, W. B. Zhu, E. N. Coker, B. Li, M. Zheng, W. Yu, H. Fan and Z. Sun, "Oxygen vacancy enhanced photocatalytic activity of pervoskite $SrTiO_3$," *ACS Appl. Mater. Interfaces,* 6, (2014) 19184.

[32] W. Luo, Z. Li, T. Yu and Z. Zou, "Effects of surface electrochemical pretreatment on the photoelectrochemical performance of Mo-doped $BiVO_4$," *J. Phys. Chem. C,* 116, (2012) 5076.

[33] G. Wang, Y. Yang, Y. Ling, H. Wang, X. Lu, Y.C. Pu, J. Zhang, Y. Tong and Y. Li, "An electrochemical method to enhance the performance of metal oxides for photoelectrochemical water oxidation," *J. Mater. Chem. A,* 4, (2016) 2849.

[34] J.K. Cooper, S.B. Scott, Y. Ling, J. Yang, S. Hao, Y. Li, F. M. Toma, M. Stutzmann, K.V. Lakshmi and I.D. Sharp, "Role of Hydrogen in Defining the n-Type Character of $BiVO_4$ Photoanodes," *Chem. Mater.,* 28, (2016) 5761.

[35] M.D. Rossell, P. Agrawal, A. Borgschulte, C. Hébert, D. Passerone, R. Erni, "Direct evidence of surface reduction in monoclinic $BiVO_4$." *Chem. Mater.,* 27 (2015) 3593.

[36] D.D. Qin, T. Wang, Y.M. Song, C.L. Tao, "Reduced monoclinic BiVO4 for improved photoelectrochemical oxidation of water under visible light," *Dalton Trans.,* 43 (2014) 7691.

[37] C.R. Fell, D. Qian, K.J. Carroll, M. Chi, J.L. Jones and Y.S. Meng, "Correlation between oxygen vacancy, microstrain, and cation distribution in lithium-excess layered oxides during the first electrochemical cycle," *Chem. Mater.,* 25, (2013) 1621.

[38] H.Y. Lee, S.J. Clark and J. Robertson, "Calculation of point defects in rutile TiO2 by the screened-exchange hybrid functional," *Phys. Rev. B,* 86 (2012) 075209.

[39] N. Zhang, X. Li, H. Ye, S. Chen, H. Ju, D. Liu, Y. Lin, W. Ye, C. Wang, Q. Xu, J. Zhu, L. Song, J. Jiang and Y. Xiong, "Oxide Defect Engineering Enables to Couple

Solar Energy into Oxygen Activation." *J. Am. Chem. Soc.,* 138 (2016) 8928.

[40] A.D. Martinez, E.L. Warren, P. Gorai, K.A. Borup, D. Kuciauskas, P.C. Dippo, B.R. Ortiz, R.T. Macaluso, S.D. Nguyen, A.L. Greenaway, S.W. Boettcher, A.G. Norman, V. Stevanovic´, E.S. Toberer and A.C. Tamboli, "Solar energy conversion properties and defect physics of $ZnSiP_2$," *Energy Environ. Sci., 9* (2016) 1031.

[41] F. Kurnia, Y.H. Ng, R. Amal, N. Valanoor and J.N. Hart, "Defect engineering of ZnS thin films for photoelectrochemical water-splitting under visible light," *Solar Energy Mater. Solar Cells,* 153, (2016) 179.

[42]L. Shan, H. Liu and G. Wang, "Preparation of tungsten-doped BiVO4 and enhanced photocatalytic activity," *J. Nanopart. Res.,* 17, (2015) 181.

[43]Z. Hu, Z. Shen and J. C. Yu, "Covalent Fixation of Surface Oxygen Atoms on Hematite Photoanode for Enhanced Water Oxidation," *Chem. Mater*., 28, (2016) 564.

[44]Z. Hu, G. Liu, X. Chen, Z. Shen and J.C. Yu, "Enhancing Charge Separation in Metallic Photocatalysts: A Case Study of the Conducting Molybdenum Dioxide," *Adv. Funct. Mater.,* 26, (2016) 4445.

[45]J. Yang, D. Wang, X. Zhou and C. Li, "A Theoretical Study on the Mechanism of Photocatalytic Oxygen Evolution on $BiVO_4$ in Aqueous Solution," *Chem. Eur. J*., 19, (2013) 1320.

[46] K. Ding, B. Chen, Z. Fang, Y. Zhang and Z. Chen, "Why the photocatalytic activity of Mo-doped $BiVO_4$ is enhanced: a comprehensive density functional study," *Phys. Chem. Chem. Phys*., 16, (2014) 13465.

[47]B. Delley, "From molecules to solids with the $DMol^3$ approach," *J. Chem. Phys*., 113 (2000) 7756.

# Chapter 4: Fabrication of $WO_3$ nanoflower thin film photoanode on etched-titanium substrate

## §4.1. Introduction

$WO_3$, with the bandgap of 2.6 eV, is an ideal semiconductor material for PEC water splitting.[1] It can not only absorb the visible light, but also cheap and easy to get, and the synthesis method is gentle and diverse. In recent years, the synthesis of different nano $WO_3$ photoanodes gradually attractted people's attention. To date, many different nano $WO_3$ photoanodes have been successfully synthesized. Nano structure of the $WO_3$ semiconductor is relative to the PEC performance of the photoanode. Some special nano structures of $WO_3$ photoanode, such as nanorod, nanosheet, mesopours, [2-8] have been proved beneficial for its PEC property. For the one reason, these special nanostructures could provide more active reaction sites during the PEC reaction process. For the other reason, direct charge transfer channel could be fabricated in the $WO_3$ photoanode thin film by these special nanostructures.

To date, $WO_3$ nanoflower (NF) growth on the conducting substrate directly has not been reported. However, the PEC performance of a photoanode can be improved by advanced NFr structure, because this structure can provide more PEC reaction active sites and unique photogenerated electron transfer route. Thus, in this section, we develop a method to fabricate $WO_3$ NF thin film on morphology controlled titanium substrate. The growth process and the PEC performance of the $WO_3$ NF photoanode were investigated also.

## §4.2. Experimental section

### §4.2.1. Preparation of the NF-structured $WO_3$ thin-film photoelectrode

The etched Ti substrate was obtained as the following. A Ti sheet (5.8×1.3 cm) was firstly rinsed with cleaning agents to remove surface greasy dirt, then ultrasonically cleaned for 15 min in a mixed solution with the proportion of water: ethanol: acetone = 1: 1: 1. Subsequently, this Ti sheet was immersed in deionized water and ultrasonically cleaned for 15 min. After rinsed with deionized water, the Ti sheet was then immersed in concentrated HCl solution (37 %) and etched for 60 min at 90 °C controlled by water bath. The etched Ti substrate was finally obtained after rinsed with deionized water.

0.625 g of $H_2WO_4$ and 0.5 g of polyvinyl alcohol (PVA) were dissolved in 10 mL of $H_2O_2$ (30%). After 15 min of ultrasonic treatment and then 3 h of stirring, the $H_2WO_4$ and PVA were completely dissolved into $H_2O_2$ solution, and a transparent sol was obtained. The sol was coated on the surface of the etched Ti sheet by spinning coating method (1000 $r \cdot min^{-1}$, 30 s), then dried at 80 °C. The spinning coating and drying process was repeated for another two more times. After annealing at 500 °C for 2 h, a $WO_3$ seed layer was coated on the etched Ti substrate.

0.7931 g of $WCl_6$ was dissolved in 70 mL of ethanol. The solution was kept for stirring until a transparent clear solution was obtained. This solution was then transferred to a 100-mL autoclave. The prepared etched Ti substrate coated with $WO_3$ seed layer was put into the autoclave, relying on the inner wall with the coated $WO_3$ seed layer facedown. The hydrothermal reaction was carried out at 100 °C for different time (1, 3, 4, 4.5, 4.75, 5, 8, 10 h). The Ti substrate was then taken out, rinsed with deionized water, dried in air and sintered at 500 °C for 2 h. The NF-structured $WO_3$ thin film was obtained on the Ti substrate. The samples obtained after 1, 3, 4, 4.5, 4.75, 5, 8, 10 h of hydrothermal reaction were labeled as $WO_3$-E1, $WO_3$-E3, $WO_3$-E4, $WO_3$-E4.5, $WO_3$-E5, $WO_3$-E8 and $WO_3$-E10, respectively.

### §4.2.2. Characterizations of the prepared samples

The crystalline structures of the prepared $WO_3$ NF-structured thin-film photoelectrodes were identified through X-ray diffraction (XRD) (D/MAX-2500/PC; Rigaku Co., Tokyo, Japan). The morphologies of the prepared $WO_3$ NF-structured thin-film photoelectrodes were investigated by using scanning electron microscope (SEM) (F250, FEI Company, USA). The bonding information of the prepared samples were analyzed by X-ray photoelectron spectroscopy (XPS, Axis Ultra, Kratos Analytical Ltd., England). The light absorption properties were investigated by using a UV/Vis diffuse reflectance spectrophotometer (U-41000; HITACHI, Tokyo, Japan).

### §4.2.3. Photoelectrochemical performance measurements

A three-electrode system was employed to measure the photoelectrochemical performance of the prepared photoelectrodes. The prepared $WO_3$ photoelectrodes are served as the working electrode, a platinum electrode is acted as the counter electrode, and Ag/AgCl (saturated KCl) is served as the reference electrode. The light with the intensity of 100 $mW \cdot cm^{-2}$ (AM 1.5) was produced by a 300-W Xe lamp (PLS-SXE 300C, Beijing Perfectlight). The variations of the current densities with time (i-t curves) under intermittent light on and off were measured at a bias potential of 1 V (vs. Ag/AgCl). The linear sweep voltammetry i-V curves were measured from 0 to 1.5 V (vs. Ag/AgCl) with a scan rate of 0.05 $V \cdot s^{-1}$. All tests were carried out in 0.1 M $Na_2SO_4$ electrolyte using the CHI660D electrochemical workstation (Shanghai Chenhua Instrument Co., Ltd., Shanghai, China).

## §4.3. Results and Discussion

### §4.3.1. Growth process of the $WO_3$ NF photoanode

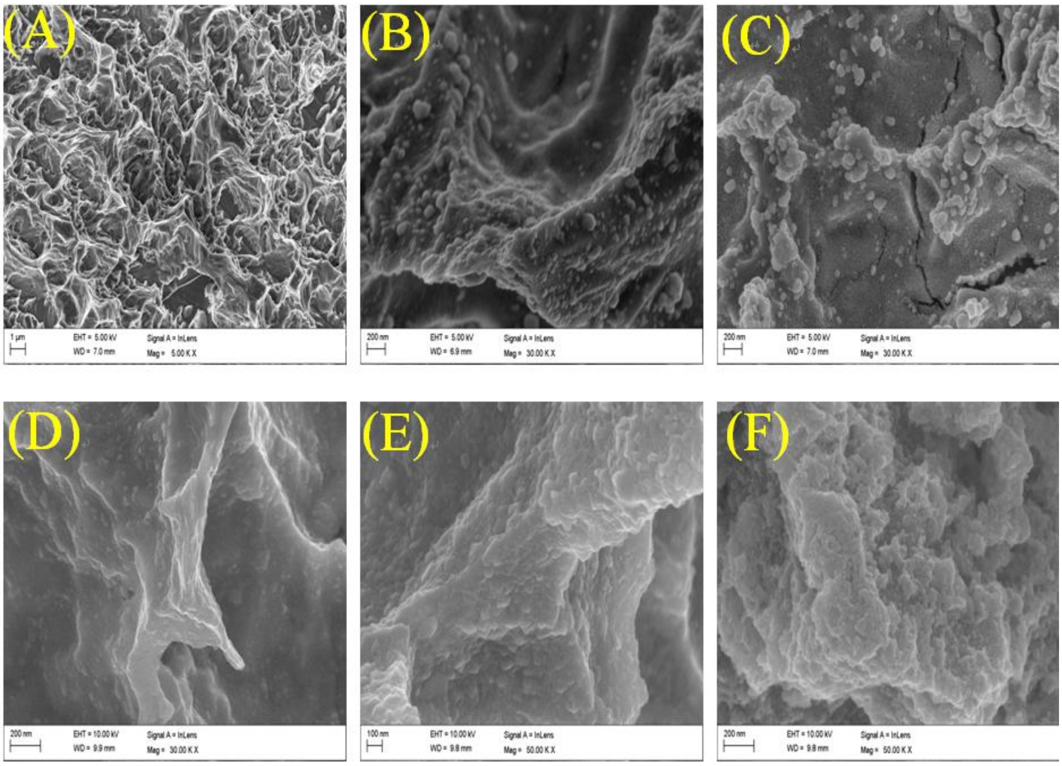

**Figure 4-1.** SEM images of the etched Ti substrate (A), $WO_3$ seed layer coated on the etched Ti substrate (B) and the $WO_3$ thin films after 1 h ($WO_3$-E1, C), 3 h ($WO_3$-E3, D), 4 h ($WO_3$-E4, E) and 4.5 h ($WO_3$-E4.5, F) of hydrothermal reaction.

Firstly, the growth process of $WO_3$ NF thin film was investigated. The SEM images with different growth time are showed in Figure 4-1. Figure 4-1A presents the SEM image of the etched Ti substrate. The unique sharp-edged mountain like structure can be found on the surface of Ti substrate after chemical etching. Then, the $WO_3$ nanoseeds were coated on the surface of etched Ti substrate, as shown in Figure 4-1B, many nanoparticles with diameter less than 50 nm were dispersed along the mountain like structure. Subsequently, the $WO_3$ seeds covered etched Ti substrates were transfer to the hydrothermal reactors and reacted for 1h, 3h, 4h and 4.5 h, respectively. And the SEM images of the prepared samples are showed in Figure 4-1C to 4-1F. From these images, we can find that with the hydrothermal reaction duration extension from 0 to 4.5 h, the thickness of $WO_3$ thin films increase obviously. However, no nanoflower like structure can be observed in these figures. This phenomenon indicated that the $WO_3$ NF could form in the initial 4.5 h, but this is a key stage for the $WO_3$ crystal nucleus formation on the etched Ti substrate.

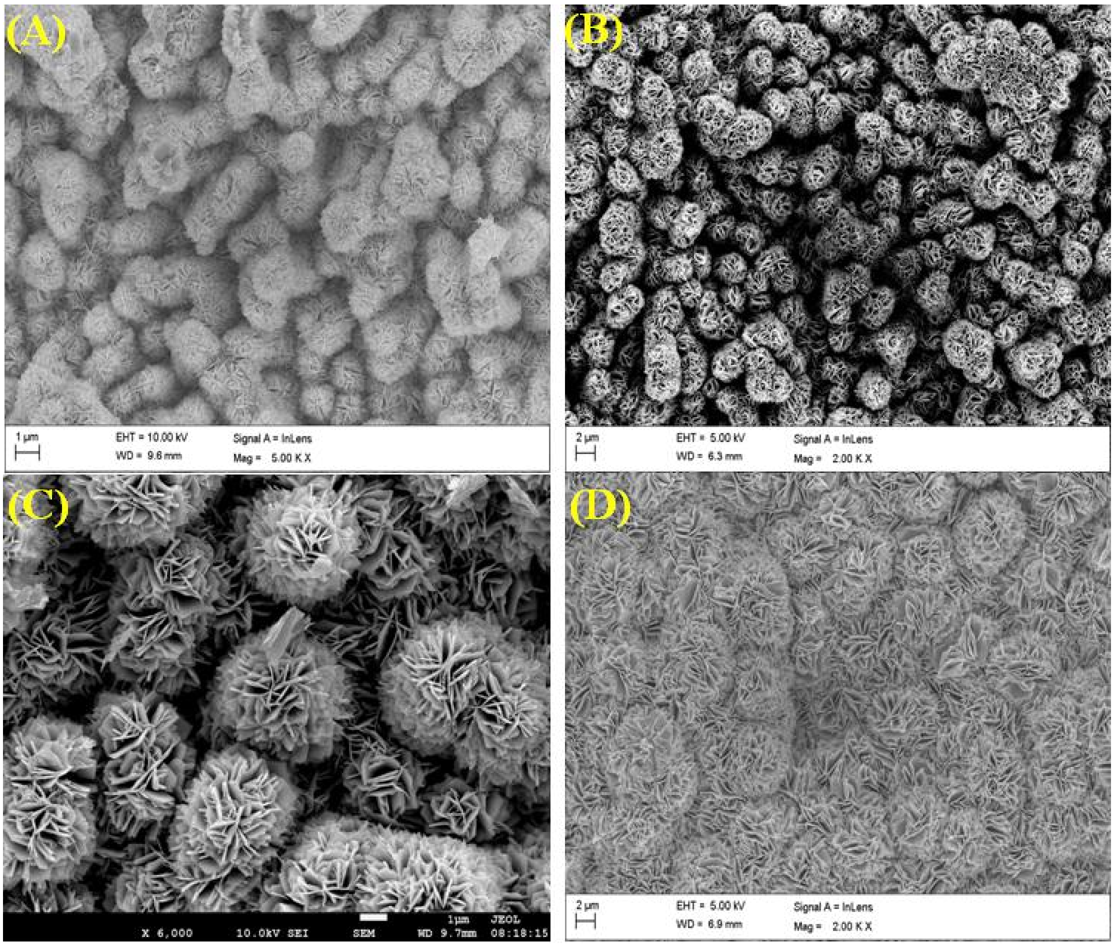

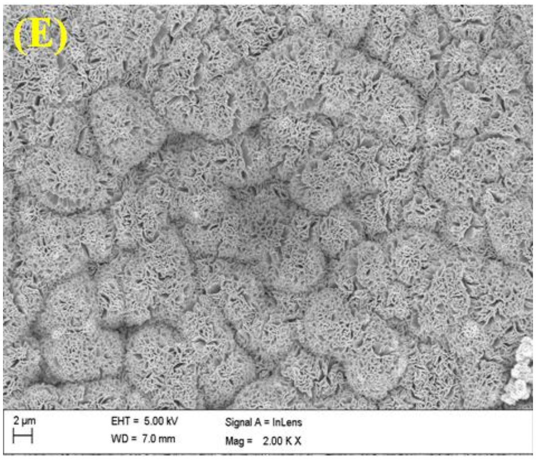

Figure 4-2. SEM images of the $WO_3$ thin films after 4.75 h ($WO_3$-E4.75, A), 5 h ($WO_3$-E5, B), 8 h ($WO_3$-E8, C), 10 h ($WO_3$-E10, D), 12 h ($WO_3$-E12, E) of hydrothermal reaction.

Figure 4-2 presents the SEM images of the $WO_3$ thin films after 4.75 h (A), 5 h (B), 10 h (C) and 12 h (D) hydrothermal reaction. Figure 4-2A shows the images of $WO_3$ thin film after 4.75 h of hydrothermal reaction. In this image, rudiment NF structures with a diameter less than 1 μm appeared on the surface of etched Ti. However after 15 Min, as shown in Figure 4-2B, compared with the $WO_3$ thin film showed in Figure 4-2A, the nanoflower-structured $WO_3$ rudiment emerged after only 15 minutes. With the hydrothermal time exceeding to 8 h, as shown in Figure 4-2C, well-defined $WO_3$ nanoflower structure could be observed. The 3-D NF fabricated by 2-D $WO_3$ nanosheet, and the diameter of the 3-D NF was approximate 5 μm, which is much larger than the one growth for 5 h. However, when the growth time exceeding 10 h, as shown in Figure 4-2D and 4-2E, the NF structure of $WO_3$ changed to a porous structure gradually.

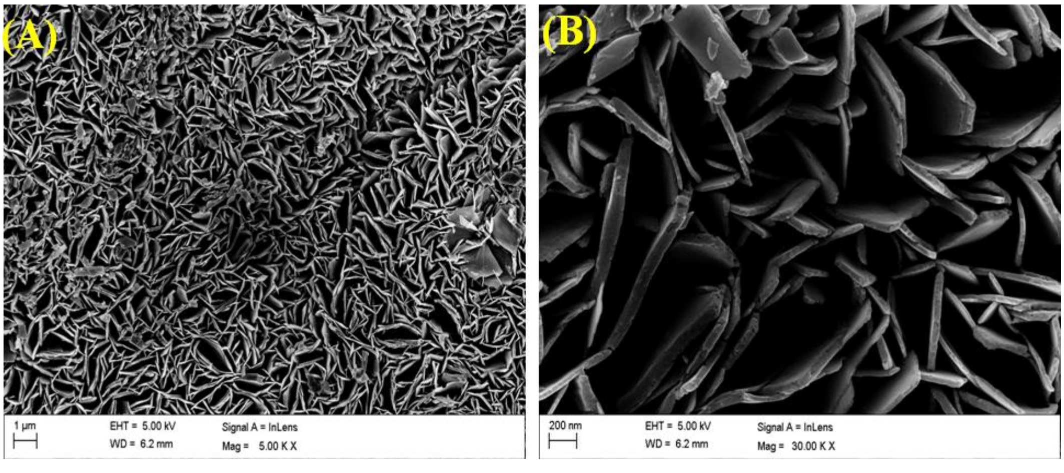

**Figure 4-3.** SEM image of vertical growth $WO_3$ nanosheet on polished Ti substrate. (A) low resolution; (B) high resolution.

$WO_3$ growth on smooth Ti substrate was prepared also, and the result shown in Figure 4-3. From these images, we can find that a vertical $WO_3$ nanosheet array could be achieved, and the top length and thickness of nanosheet were nearly 300 nm and 20 nm, respectively. So, compared Figure 4-2 with Figure 4-3, we can get the information that sharp-edged Ti substrate is the core point to induce $WO_3$ NF structure growing.

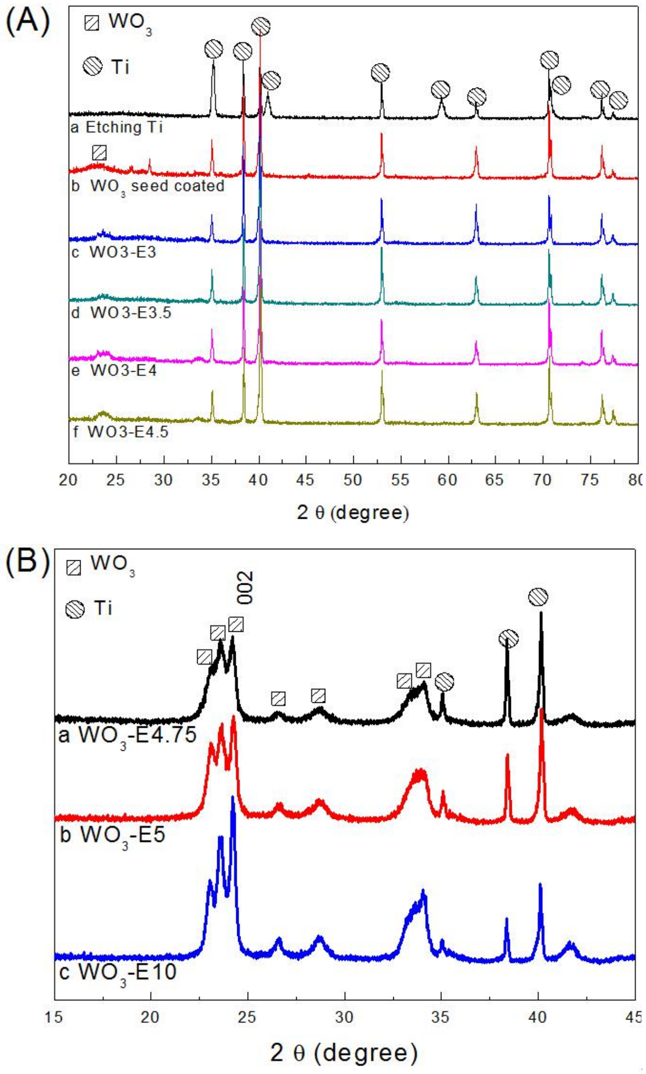

**Figure 4-4**. The XRD patterns of the prepared series $WO_3$ thin films. (A) The XRD results of the $WO_3$ thin films with the hydrothermal reaction durations less than 4.5 h; (B) The XRD results of the $WO_3$ thin films with the hydrothermal reaction time more than 4.5 h.

Figure 4-4 shows the other XRD results of the prepared $WO_3$ thin films on the etched Ti substrate. Figure 4-4A shows the XRD results of the $WO_3$ thin films with the hydrothermal reaction duration less than 4.5 h. Only a weak diffraction peak of

$WO_3$ at 23° can be observed and the main diffraction peaks are come from the Ti substrate, demonstrating that $WO_3$ did not growth during the first 4.5 h of the hydrothermal reaction. These results are in accord with the SEM images showed in Figure 4-1. Figure 4-4B shows the XRD results of the $WO_3$ thin films with the hydrothermal reaction time more than 4.5 h. The intensities of the diffraction peaks corresponding to $WO_3$ are obviously enhanced, demonstrating that the $WO_3$ thin films go through a rapid growth period with hydrothermal reaction duration >4.5 h. Further increasing of the hydrothermal reaction duration, the intensities of the diffraction peaks corresponding to $WO_3$ are gradually enhanced, and the diffraction peaks corresponding to the Ti substrate can still be observed. This may be due to the sharp-edged surface of the etched Ti substrate. The ridgy parts of the Ti substrate are close to the surface of the $WO_3$ thin film, resulting in the detectability of Ti in the XRD patterns.

Figure 4-5 shows the growth processes of $WO_3$ on smooth Ti and etched Ti substrates with different nanostructures, respectively. The strategy in Fig. 4-5A shows a common method for a vertical $WO_3$ nanosheet thin film growth on smooth Ti substrate. The other strategy is etching the Ti substrate surface firstly to form a sharp-mountain-like structure prior to deposition of $WO_3$ seeds. As described in Figure 4-5B, the sharp edge of etched Ti substrate can provide an orientation force to control the nucleus process of $WO_3$ nanosheets, and finally to fabricate a flower-like $WO_3$ thin film after hydrothermal growth. The SEM images corresponding to the steps in Figure 4-5B are presented to illustrate the morphology evolution (Figure 4-5C). As shown in Figure 4-5C(i), we can find that the surface morphology of Ti substrate change to a sharp-mountain-like structure after acid etching, and the $WO_3$ seed NPs with a diameter of 20 nm are uniformly distributed on the surface (Figure 4-5C(ii)). The sharp-mountain-like structure and $WO_3$ seed NPs can be found clearly. Subsequently, the hydrothermal method was employed to grow $WO_3$ nanostructures on the etched Ti substrate covered with $WO_3$ nanoseeds. When the hydrothermal growth time extent to 4.75 h, as shown in Figure 4-5C(iii), the $WO_3$ NFs composed of nanosheet with a size less than 500 nm appeared on the etched Ti substrate. The size of the $WO_3$ NFs became larger with the extension of hydrothermal reaction time. As shown in Figure 4-5C(iv), a well-defined $WO_3$ NFs thin film is obtained as the hydrothermal time extended to 8 h.

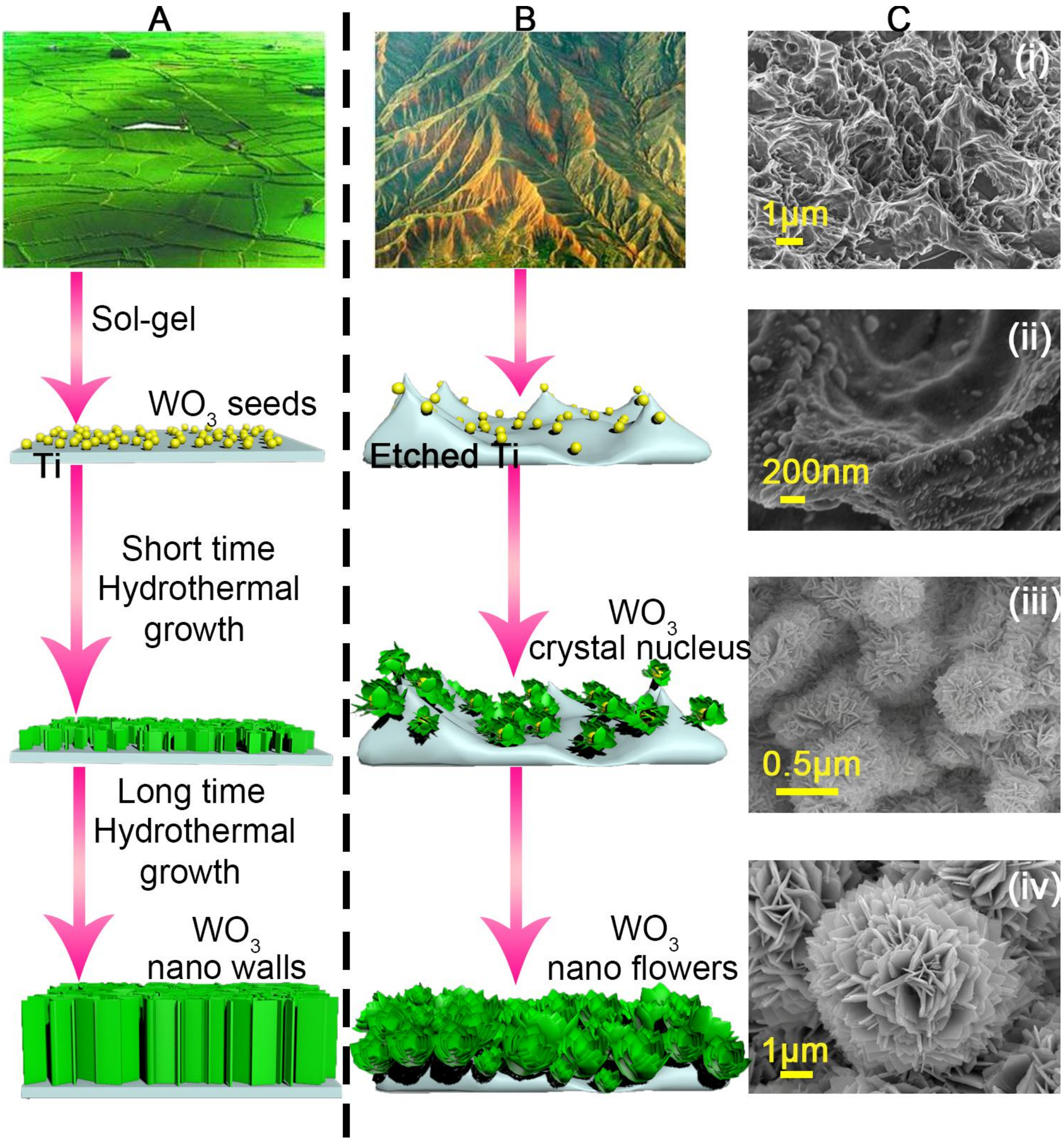

**Figure 4-5**. (A) Schematic diagram of $WO_3$ nanosheet thin film preparation process; (B) $WO_3$ NF like thin film preparation process; (C) SEM images of $WO_3$ NF thin film growth process corresponding to (B).

### §4.3.1. Optical property and PEC performance of $WO_3$ NF photoanode

Figure 4-6 shows the UV/Vis diffuse reflectance spectra of the etched substrate (a), the $WO_3$ seeds coated on the etched Ti substrate (b) and the prepared series $WO_3$ NFs thin films on the etched Ti substrate (c-k). Curve 4-6a shows the UV/Vis diffuse reflectance spectrum of the etched Ti substrate. The characteristic light absorption below 380 nm may come from the naturally oxidized $TiO_2$ ultrathin layer on the surface of the etched Ti substrate. Curve 4-6b to 4-6f are the UV/Vis diffusion reflectance spectra of the $WO_3$ seeds coated on the etched Ti substrate and the series of $WO_3$ thin films on etched Ti substrate which hydrothermal reaction time are lower than 4.5 h. No characteristic light absorption of $WO_3$ can be clearly observed in these spectra. This result indicated that $WO_3$ did not growth quickly in the hydrothermal growth term less than 4.5 h. When the hydrothermal reaction time reaching 4.75 h and exceeding 4.75 h, the characteristic absorption edges of these samples are observed at 460 nm, which point to the predominant light absorption of $WO_3$.

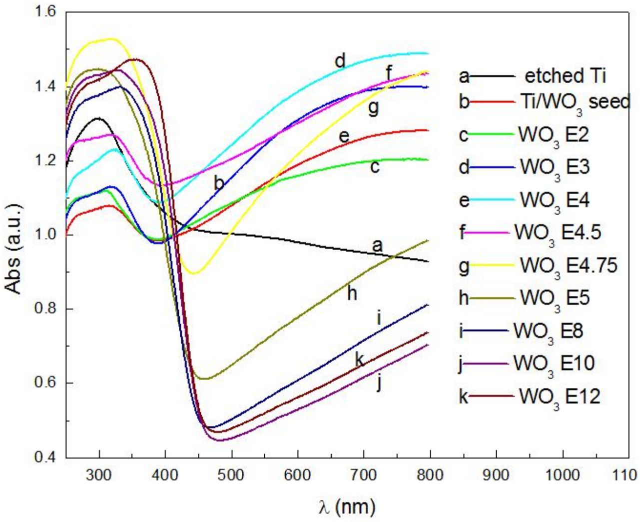

**Figure 4-6**. The UV/Vis diffuse reflectance spectra of the etched Ti substrate (a), the $WO_3$ seeds coated on the etched Ti substrate (b) and the prepared series $WO_3$ thin films on the etched Ti substrate (c-k).

Figure 4-7A shows the photoinduced i-t curves of the prepared series $WO_3$ NF photoanode (1 h to 10 h of hydrothermal growth time) with light switched on and off. As shown in Curves 4-7Aa~4-7Ad, the photogenerated current densities of the prepared $WO_3$ thin-film photoanodes with the hydrothermal growth time less than 4.5 h are very low. Curve 4-7Ae shows the photo current densities with light switched on and off for the prepared $WO_3$ photoanode with 4.75 h of hydrothermal growth. The steady photogenerated current density of this photoelectrode is 0.75 $mA \cdot cm^{-2}$, which is 7.5 times higher than that of $WO_3$-E4.5. The photoinduced current densities of the $WO_3$ thin-film photoelectrodes increase with further increase the hydrothermal growth time. When it reaches 8 h, the steady photogenerated current density of this photoelectrode is 1.80 $mA \cdot cm^{-2}$, which the maximum value. The photogenerated current density of the corresponding photoanodes are decreased by increasing the hydrothermal growth time. Therefore, the optimal hydrothermal growth time for the nanoflower-structured $WO_3$ is 8 h. Curve 4-7Ai shows the photo current densities of the nanoplate-structured $WO_3$ thin film photoanode with 8 h of hydrothermal reaction.

This photoanode is prepared on an unetched Ti substrate. The photoinduced current density of this photoanode is only 0.4 mA·cm$^{-2}$, which value is about one fourth of that of the nanoflower-structured $WO_3$ thin film photoelectrode. The big difference of the photoinduced current densities between $WO_3$-P8 and $WO_3$-E8 shows that the nanoflower-structured $WO_3$ possesses much higher photoelectrochemical properties.

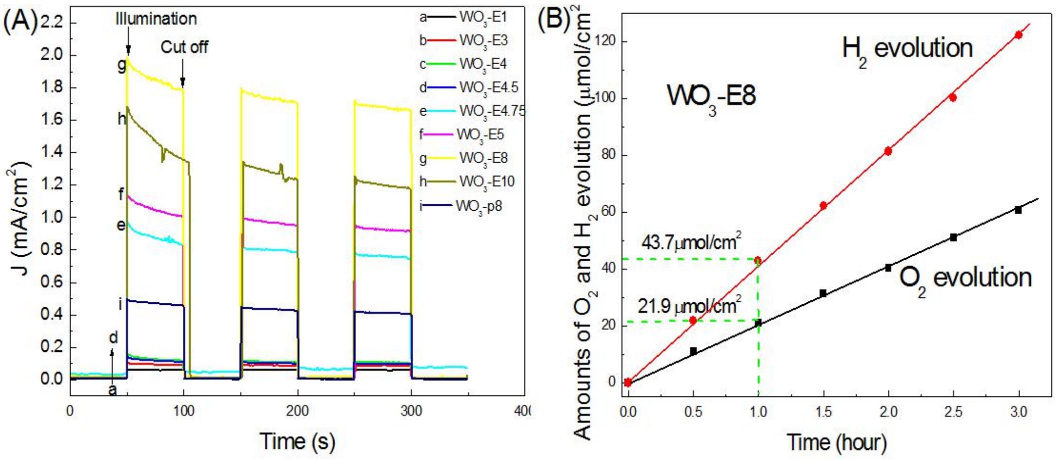

**Figure 4-7**. (A) Photoinduced i-t curves of the prepared $WO_3$ NF photoanodes; (B) PEC water splitting for hydrogen and oxygen evolution performance of $WO_3$-8E, tested under AM 1.5 G (100 mW/cm$^2$) illumination, in 0.1 M $Na_2SO_4$ electrolyte, bias potentiao 1.0 V (vs. Ag/AgCl).

The PEC water splitting for hydrogen and oxygen evolution performance of $WO_3$-8E photoanode is showed in Figure 4-7B. The total test time was 3 hours. In the first one hour, the oxygen and hydrogen evolution amounts are 21.9 and 43.7 μmol/cm$^2$, respectively, the proportion of the oxygen and hydrogen amount is near 1:2, which value very approachs to the theoretical proportion of the water splitting, indicating the water was decomposed completely by the PEC process of the photoanode. Meanwhile, both the oxygen and hydrogen evolution amount points are linear in 3 hours, this phenomenon indicated that the PEC performance of $WO_3$-8E is stable during working process.

Figure 4-8A shows the photoinduced volt-ampere characteristic curves (I-V curves) of the prepared series $WO_3$ thin-film photoelectrodes with the hydrothermal reaction time less than 4.5 h. With the increase of the hydrothermal reaction time from 0 to 4.5 h, the photogenerated current density of the prepared $WO_3$ photoanode increase. However, the photogenerated current density of the $WO_3$ thin-film photoelectrode with 4.5 h of hydrothermal reaction is only 0.15 mA·cm$^{-2}$ at the bias potential of 1.5 V (vs Ag/AgCl). Figure 4-8B shows the photoinduced I-V curves of the prepared $WO_3$ thin-film photoanodes with the hydrothermal growth time longer than 4.5 h. Because of the positive conduction band potential of $WO_3$, the onset bias potential of the photogenerated current density on the I-V curves is close to 0.2 V. With the further increase of the bias potential to 0.4 V, the photogenerated current density increased rapidly. When the hydrothermal growth time increasing from 4.75 h to 8 h, the photogenerated current density shows a upward trend. When the hydrothermal growth time reached 8 h, the $WO_3$ NF photoanode shows the largest photoinduced current density (2.0 $mA\cdot cm^{-2}$). This result demonstrates that NF like structure can improve the PEC performance of the $WO_3$ photoanode, and after the hydrothermal growth time exceeded 4.75 h, the nanoflower like structure gradually changed to perfect and the film thickness increased rapidly. Therefore, the optical absorption sites and active reaction sites were enhanced, resulting in the photogenerated current density increasing. However, with the growth time longer than 8 hours, the morphology of the $WO_3$ thin film changed from the nanoflower like structure to a mesoporous structure, so that decreased the active reaction sites and transfer rate of the reaction matters during the PEC reaction process.

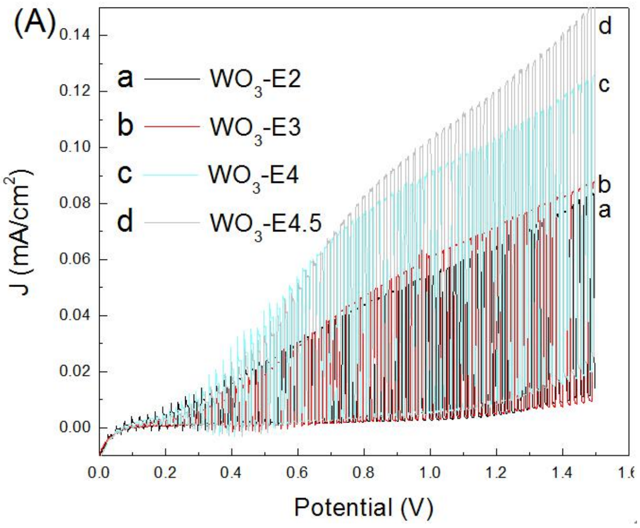

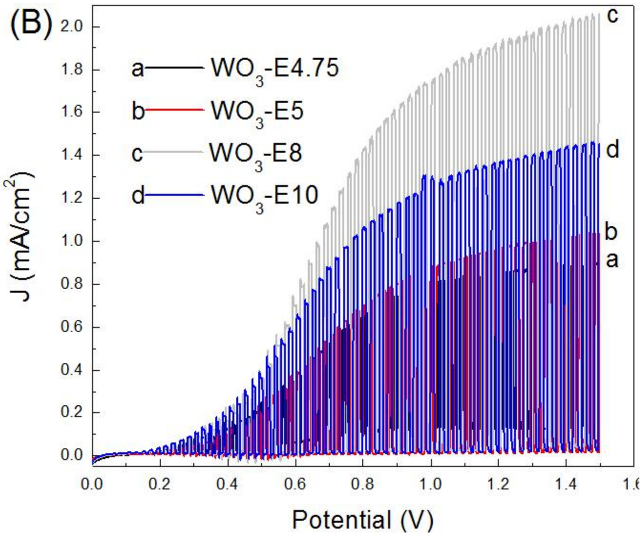

**Figure 4-8.** The photoelectrochemical performance of the prepared series nanoflower-structured $WO_3$ thin-film photoelectrodes with different hydrothermal reaction time. (A) The photoinduced I-V characteristic curves of the prepared series $WO_3$ thin-film photoelectrodes with the hydrothermal reaction time less than 4.5 h; (B) The photoinduced I-V curves of the prepared series $WO_3$ thin-film photoelectrodes with the hydrothermal reaction time more than 4.5 h.

**Table 4-1**. Comparison of the PEC performance of the typical $WO_3$ photoelectrodes reported in literature and in the present study.

| $WO_3$ with different structure | Light intensity ($mW\cdot cm^{-2}$) | Bias potential (V) | Electrolyte | Photoinduced current density ($mA\cdot cm^{-2}$) | Ref. |
|---|---|---|---|---|---|
| $WO_3$ Flake wall | 100 (AM 1.5) | 1.0 V (vs Ag/AgCl) | $Na_2SO_4$ (0.1 M) | 1.4 | [9] |
| Molecular iron modified $WO_3$ | 100 (AM 1.5) | 1.0 V (vs Ag/AgCl) | $Na_2SO_4$ (0.1 M) | 1.1 | [10] |
| $WO_3$ planar film | 100 (AM 1.5) | 1.0 V (vs Ag/AgCl) | $Na_2SO_4$ (0.5 M) | 1.0 | [11] |
| $WO_3$ planar film | 100 (AM 1.5) | 1.0 V (vs Ag/AgCl) | $Na_2SO_4$ (0.5 M) | 0.5 | [12] |
| $WO_3$ Nanorod array | 100 (AM 1.5) | 1.0 V (vs Ag/AgCl) | $Na_2SO_4$ (0.5 M) | 0.25 | [13] |
| $WO_3$ Nanoflower | 100 (AM 1.5) | 1.0 V (vs Ag/AgCl) | $Na_2SO_4$ (0.1 M) | 1.8 | Present study |

Table 4-1 shows the photoelectrochemical performance of $WO_3$ with different morphologies prepared in recent years, and compared them with this work. According to the reports from the literatures, the best photoelectrochemical performance was obtained by $WO_3$ with flake wall like structure in $Na_2SO_4$ solution under the illumination of AM 1.5 (100 mW·cm$^{-2}$) and at the bias potential of 1 V (vs Ag/AgCl), and the photoinduced current density of $WO_3$ with this structure could reach 1.4 mA · cm$^{-2}$. In the present work, for the nanoflower-structured $WO_3$ thin-film photoelectrode with 8 h of hydrothermal reaction, a photoinduced current density of 1.8 mA·cm$^{-2}$ was obtained under the same test condition as in the compared references, which is significantly enhanced compared with that in the previous reports.

## §4.4. Conclusion

In summary, well-defined $WO_3$ NF photoanodes were fabricated. The sharp-edage mountain like structure of the titaninum substrate plays an important role to induce the $WO_3$ NF structure growth on it. The sharp edge of etched Ti substrate can provide an orientation force to control the nucleus growth process of $WO_3$ nanosheets, and finally to fabricate a flower-like $WO_3$ thin film after hydrothermal growth. The $WO_3$ NF formation process could be divided into two parts. First part is the nucleus step, which occurred at the initial 4.5 hours hydrothermal growth. The second part is the $WO_3$ NF quick growth stage. In this stage, the $WO_3$ nanosheets on NF would explosive growth, and achieved a well-defined NF structure with the growth time exceeding to 8 h. Further extending the growth time, the NF structure would transfer to mesoporous thin film structure. The $WO_3$ NF photoanode with 8 h growth time shows the best PEC performance, a 1.8 mA/cm$^2$ photocurrent density (bias potential 1V vs Ag/AgCl) could be achieved in $NaSO_4$ electrolyte under 100 mW/cm$^2$ AM 1.5G simulate sun light illumination.

## §4.4. Reference

[1] X. Liu, F. Wang and Q. Wang, “Nanostructure-based $WO_3$ photoanodes for photoelectrochemical water splitting,” *Phys. Chem.y Chem. Phys.,* 14, (2012) 7894.

[2] J. Polleux, N. Pinna, M. Antonietti and M. Niederberger, “Growth and assembly of crystalline tungsten oxide nanostructures assisted by bioligation,” *J. Am. Chem. Soc.*, 127, (2005) 15595.

[3] H.G. Choi, Y.H. Jung and D.K. Kim, “Solvothermal synthesis of tungsten oxide nanorod/nanowire/nanosheet,” *J. Am. Ceram. Soc.*, 88, (2005) 1684.

[4] J.M. Wang, P.S. Lee and J.Ma, “Synthesis, growth mechanism and room-temperature blue luminescence emission of uniform W03 nanosheets with W as starting material,” *J. Cryst. Growth*, 311, (2009) 316.

[5] J.M. Ma, J. Zhang, S.R. Wang, T.H. Wang, J.B. Lian, X.C. Duan and W.J. Zheng, “Topochemical preparation of $WO_3$ nanoplates through precursor $H_2WO_4$ and their gas-sensing performances,” *J. Phys. Chem. C*, 115, (2011) 18157.

[6] S.L. Bai, K.W. Zhang, R.X. Luo, D.Q. Li, A.F. Chen and C.C. Liu, “Low-temperature hydrothermal synthesis of $WO_3$ nanorods and their sensing properties for $NO_2$,” *J. Mater. Chem.*, 22, (2012) 12643.

[7] F. Zheng, M. Guo and M. Zhang, “Hydrothermal preparation and optical properties of orientation-controlled $WO_3$ nanorod arrays on ITO substrates,” *CrystEngComm*, 15, (2013) 277.

[8] X.M. Fu and Z.Z. Yang, “$WO_3$ nanorods synthesized using the hydrothermal method and its light-sensitive character,” *Chin. Ceram.*, 3, (2011) 005.

[9] F. Amano, D. Li and B. Ohtani, “Fabrication and Photoelectrochemical Property of Tungsten(VI) Oxide Films with a Flake-wall Structure,” *Chem. Commun.*, 46, (2010) 2769.

[11] B.M. Klepser and B.M. Bartlett, “Anchoring a Molecular Iron Catalyst to Solar-Responsive $WO_3$ Improves the Rate and Selectivity of Photoelectrochemical Water Oxidation,” *J. Am. Chem. Soc.*, 136, (2014) 1694.

[12] K. Zhang, X.J. Shi, J.K. Kim and J.H. Park, “Photoelectrochemical Cells with Tungsten Trioxide/Mo-doped $BiVO_4$ Bilayers,” *Phys. Chem. Chem. Phys.*, 14, (2012) 11119.

[13] J. Su, L. Guo, N. Bao amd C.A. Grimes, “Nanostructured $WO_3/BiVO_4$ Heterojunction Films for Efficient Photoelectrochemical Water Splitting,” *Nano Lett.*, 11, (2011) 1928.

# Chapter 5: Photogenerated-carrier separation along edge dislocation of $WO_3$ nanoflower single crystal photoanode

## §5.1. Introduction

$WO_3$ is a classic photoanode semiconductor with the bandgap of 2.6 eV, and its theoretical photoelectric conversion efficiency can reach 4.8%. [1] However, up to now, the photoelectric conversion efficiency of the $WO_3$ photoanodes is far behind that of the maximum theoretical value. [2-5] There are series of problems to limit the photoanode property of $WO_3$, such as low photons capture capacity, high charge transfer resistance and slow surface reaction rate etc.[1] Among them, photogenerated carrier recombination is a key process to cut down the photoelectric conversion efficiency of $WO_3$ photoanodes. [6-9]

It is reasonable to understand that photogenerated carriers can be separated by the heterojunction interface or mixed phase-junction in the semiconductors system. Since an interfacial band bending caused by Fermi level equilibrium in the space charge region can trigger the efficient carriers separation. [10-12] Recently, amounts of evidences demonstrated that the photogenerated carriers could be separated at different surface crystal facets in single crystal semiconductors, such as $TiO_2$ [13-15] and $BiVO_4$ [16-18]. It is believed that energy level difference among various crystal facets, so-called crystal facets heterojunction, could drive efficient charge separation.

Point defects, such as oxygen vacancies, have been widely employed to improve the PEC water oxidation performance of photoanodes. [19-23] However, in this field, line defects (dislocations) on photoanodes have not attracted attention. Dislocation, especially edge dislocation, is usually formed by the facets sliding in the crystal when high temperature and mechanical/gas pressures are applied on the crystal. With the facets sliding occurring in the crystal, two different facets will expose on either side of the dislocation line. [24-26] Thus, it can be speculated that an efficient charge separation could be improved along the dislocation, if the energy difference of the two facets between the dislocation line is large enough. Compared with the surface crystal facets heterojunction, the effective crystal facets heterojuction area can be enlarged greatly by introducing suitable dislocations in the crystal, so that increase the PEC performance of the photoanode further.

Herein, we prepared a well-defined hierarchical $WO_3$ NF-like thin film photoanode on etched Ti substrate, (After etching, keen-edged nanostructures would be formed on the surface of Ti substrate. They can provide lopsided pressure and extrusion during the $WO_3$ single crystal growth and fabrication, in order to compel the dislocation formed on $WO_3$ crystal). The NF structure was composed of single crystal mesoporous $WO_3$ 2D-nanoflakes. Observing the crystal at the atomic level, there were many dislocations observed on the $WO_3$ nanoflakes forming by the mismatch of (020) and (002) facets. More importantly, the dislocation density on $WO_3$ nanoflake could be adjusted by controlling the annealing time. It was observed that the photo-induced charge separation capacity of the $WO_3$ photoanodes were decreased with the dislocation decreasing, which means that line defects resulted from dislocation on $WO_3$ photoanode can improve the photo-induced charge separation efficiency during the PEC water oxidation process. To reveal the mechanism on this phenomenon, the density functional theory (DFT) calculation was carried out to investigate the band energy structure of the (020) and (002) facets along the dislocation line. Apparently, there are a band energy difference between the (020) and (002) facets, which leads to the enhancement on charge separation between the two facets.

## §5.2. Experimental section

### §5.2.1. Controlling the edged dislocation density on NF-structured $WO_3$ photoelectrode

The $WO_3$-E8 photoanode was prepared as the method introduced in Chapter 4. For controlling the edged dislocation concentration, several of $WO_3$-E8 thin films were treated at 500 °C for 2 h, 4 h, 8 h, and 12 h respectively, and labeled as $WO_3$-E8-2h, $WO_3$-E8-4h, $WO_3$-E8-8h and $WO_3$-E8-12h.

### §5.2.2 Characterizations of the prepared samples

The crystalline structures of the prepared $WO_3$ NF-structured thin-film photoelectrodes were identified through X-ray diffraction (XRD) (D/MAX-2500/PC; Rigaku Co., Tokyo, Japan). The morphologies of the prepared $WO_3$ NF-structured thin-film photoelectrodes were investigated by using scanning electron microscope (SEM) (F250, FEI Company, USA). The microstructure, interface status and bonding information of the prepared samples were analyzed by using a field emission high-resolution transmission electron microscope (FEI G2F20, FEI Company, USA), and X-ray photoelectron spectroscopy (XPS, Axis Ultra, Kratos Analytical Ltd., England). The light absorption properties were investigated by using a UV/Vis diffuse reflectance spectrophotometer (U-41000; HITACHI, Tokyo, Japan). For defect confirmation, the crystal structure of $WO_3$ [27] is primitive monoclinic structure with space group P2/n, lattice parameters a = 0.7297 nm, b = 0.7539 nm, c = 0.7688 nm and beta = 90.91°. In order to find out what kind of the defects could be possible for monoclinic $WO_3$ crystal, the sample of $WO_3$ crystal heated for 2 h was extensively investigated by using high resolution transmission electron microscopy (HRTEM).

### §5.2.3. Photoelectrochemical performance measurements

A three-electrode system was employed to measure the photoelectrochemical performance of the prepared photoelectrodes. The prepared $WO_3$ photoelectrodes are served as the working electrode, a platinum electrode is acted as the counter electrode, and Ag/AgCl (saturated KCl) is served as the reference electrode. The light with the intensity of 100 $mW\cdot cm^{-2}$ (AM 1.5) was produced by a 300-W Xe lamp (PLS-SXE 300C, Beijing Perfectlight). The variations of the current densities with time (i-t curves) under intermittent light on and off were measured at a bias potential of 1 V (vs. Ag/AgCl). The linear sweep voltammetry i-V curves were measured from 0 to 1.5 V (vs. Ag/AgCl) with a scan rate of 0.05 $V\cdot s^{-1}$. The incident photon-to-current conversion efficiency (IPCE) of the prepared photoelectrodes were tested at the bais potental of 1.5 V (vs. Ag/AgCl) by using a 300-W Xe lamp with a monochromator. All tests were carried out in 0.1 M $Na_2SO_4$ electrolyte using the CHI660D electrochemical workstation (Shanghai Chenhua Instrument Co., Ltd., Shanghai, China). Mott-Schottky plots were measured at the potential range of -0.2 V ~ 1.5 V and the frequency of 10 Hz with an AC voltage magnitude of 10 mV.

### §5.2.4. Theoretical calculation

The calculations were performed by the first-principles calculations based on spin-polarized density functional theory (DFT). The Vienna Ab initio Simulation Package (VASP) is used to solve Kohn-Sham equations with periodic boundary conditions and a plane wave basis set.[28-31] Electron-ion interactions were described by projector-augmented wave (PAW) potentials; [32] exchange and correlation energies were also calculated by using the Perdew-Burke-Ernzerhof form of the spin-polarized generalized gradient approximation (GGA-PBE). [33] We used a kinetic energy cutoff of 450 eV for all calculations, and the convergence threshold was set to $10^{-5}$ eV in energy and $10^{-3}$ eV/Å in force, and cell dimensions along the z direction were 15 Å to avoid interaction between layers. In order to improve the description of the electronic structure of $WO_3$ systems, we adopt a DFT+U method with U-J values of 4.5 eV for W atom. The Monkhorst-Pack k-point grids (2×2×1) are employed for Brillouin zone integration for all the structures, using approximately same k-point density for reciprocal cells of different sizes. As the {020} and {002} surfaces of γ-monoclinic $WO_3$ are predominant exposed crystal faces in this work, [34] these two surfaces were modeled by a periodic slab with four-$WO_2$ layers and three-O monolayers cleaved from the optimized bulk structures. For all of the slab calculations, two bottom $WO_2$ layers and one O-monolayer were fixed at the bulk position while the others are relaxed. By optimizing the pure γ-monoclinic $WO_3$ structure, we got the lattice parameters as following: a=7.464, b=7.663, c=7.833 Å and β=90.36°, which are in reasonable agreement with the experiment data[7] and previous DFT studies. [35-40]

## §5.3. Results and Discussion

### §5.3.1. Nanostructure, component and crystal analysis

Figure 5-1A and 5-1B presents the SEM image of $WO_3$-E8-2h and $WO_3$-E8-12h, respectively. Both samples showed well-defined NF like structure, the flower structured clusters are assembled by nanosheet structures. The diameters are approximately 5 μm, the length of the nanosheet are approximately 200 nm. These results indicated that the nanosturctrue of the $WO_3$-E8 was not changed with the annealing time exceeding to 12 hours under 500 °C.

Figure 5-1 C is the cross-section SEM of $WO_3$-E8-2h, it can be found from this image that the thickness of the $WO_3$ NF thin film is approximately 6 μm. Figure 5-1 D shows the EDS mapping of $WO_3$-E8-2h. From this image, the W and O elements can be observed, which is in according with the components of the $WO_3$.

Figure 5-2 shows the XPS spectra of the $WO_3$-E8-2h. Figure 5-2A shows the total XPS survey spectrum of this sample, W and O elements can be observed. The elemental compositions fit those of $WO_3$. The C1s peak comes from the background of XPS tests. Figure 5-2B and Figure 5-2C show the high resolution W4f and O2p core level XPS spectra of this sample, respectively. The binding energy peaks observed in Figure 5-2B and Figure 5-2C can be attributed to the W-O bond in $WO_3$. Figure 5-2D shows the high resolution Ti2p core level XPS spectrum of this sample, Ti XPS peak did not observed on this curve. XPS tests can only detect the elemental bonding information of the materials with the depth less than 10 nm. This result indicated that $WO_3$ layer covered on Ti substrate was thickness enough.

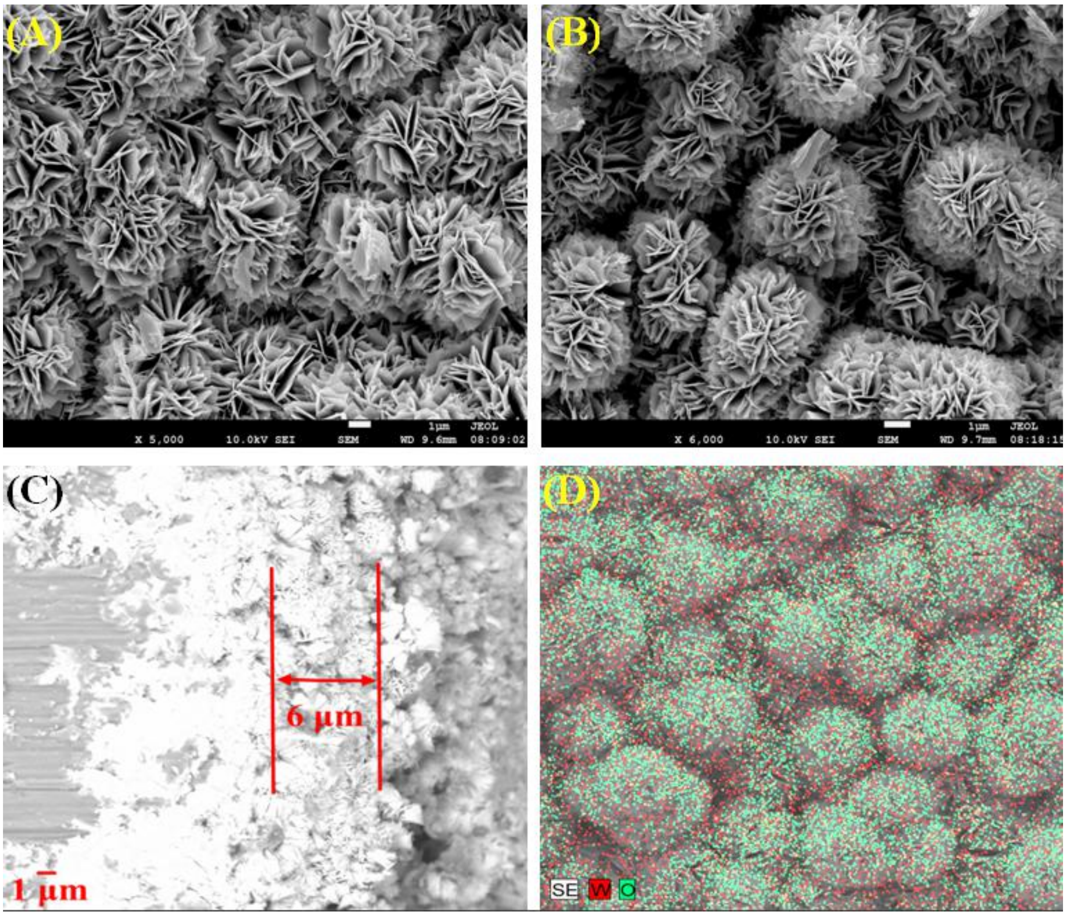

**Figure 5-1.** SEM images of (A) $WO_3$-E8-2h and (B) $WO_3$-E8-12h. (C) is the cross-section SEM of $WO_3$-E8-2h. (D) is the EDS mapping of $WO_3$-E8-2h.

The crystal phases of the $WO_3$-E8 with different annealing times at 500 °C were tested and the results show in Figure 5-3. Nanostructure and crystal phase of the semiconductor are two factors to influence the PEC performance of photoanode. The SEM images showed in Figure 5-1A and 5-1B have indicated that the nanostructure of $WO_3$-E8 photoanode has not been changed with the annealing time increasing. Herein, as shown in Figure 5-3, we can found that all samples presented a monoclinic phase of the $WO_3$, indicating that the crystal phase of the $WO_3$-E8 was not changed with the annearling time increasing from 2 h to 12 h.

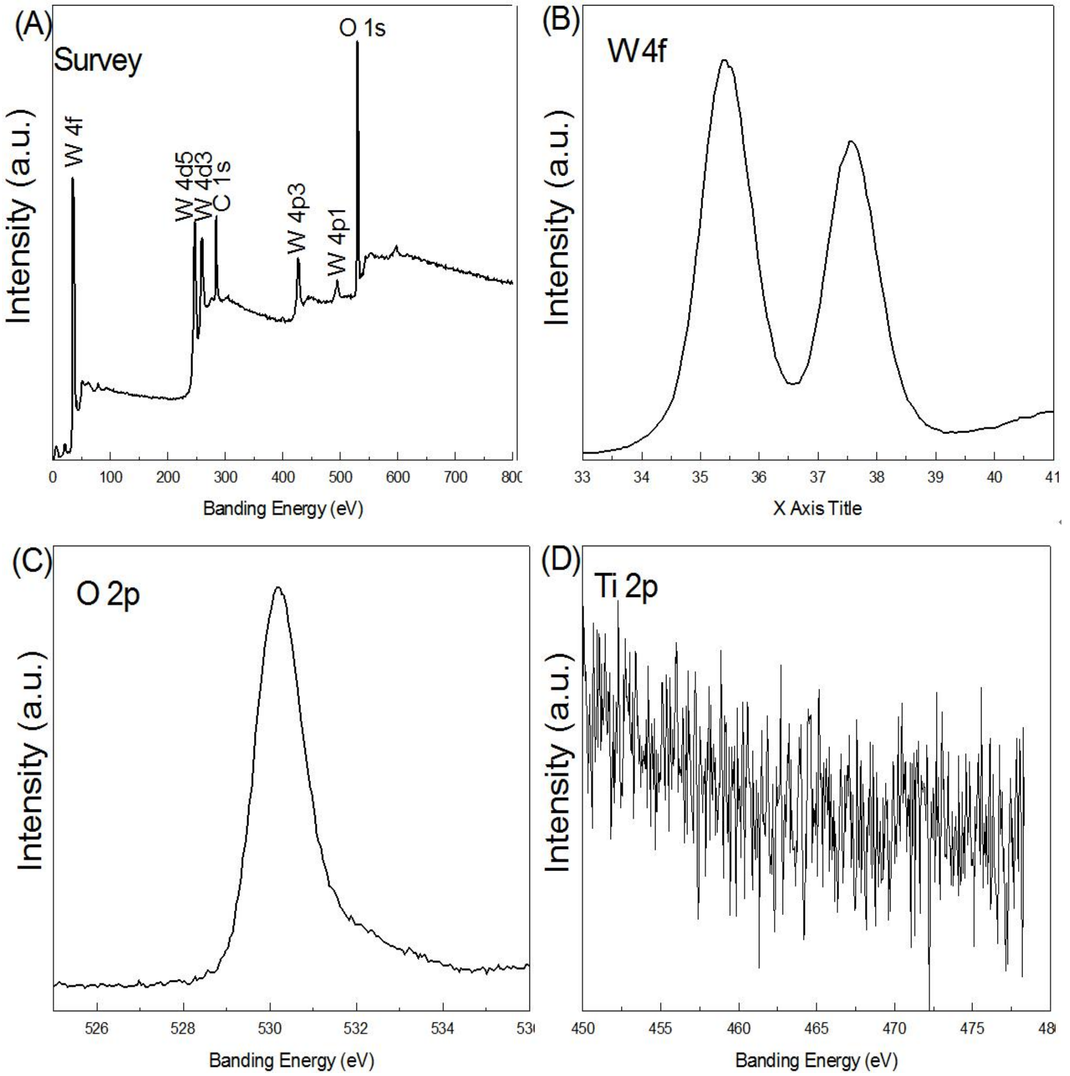

**Figure 5-2**. The XPS spectra of the $WO_3$ thin film after 8 h of hydrothermal reaction on the etched Ti substrate. (A) the total XPS survey spectrum; (B) the W4f core level XPS spectrum; (C) the O2p core level XPS spectrum; (D) the Ti2p core level XPS spectrum.

### §5.3.2. Dislocation analysis

The TEM technology was employed to analyze the dislocation structure of $WO_3$ NFs. Figure 5-4 shows the TEM images of $WO_3$-E8-2h thin film with low and high resolution. The low resolution TEM image is showed in Figure 5-3A, there are many tips with diameter ~ 20 nm can be found on the surface of $WO_3$ nanosheet. Figure 5-4B to 4D present the HRTEM image of this nanosheet. From the HRTEM image and SAED patter shown on Figure 5-4B, it can be found that the (002) and (020) facets exposed on the surface of $WO_3$-E8-2h nanosheet. From Figure 5-4C and 5-4D, the dislocation area can be found clearly on the surface of $WO_3$ nanosheet. And the (002) and (020) facets distribution on each side of the dislocation area, like the schematic showed in Figure 5-4E.

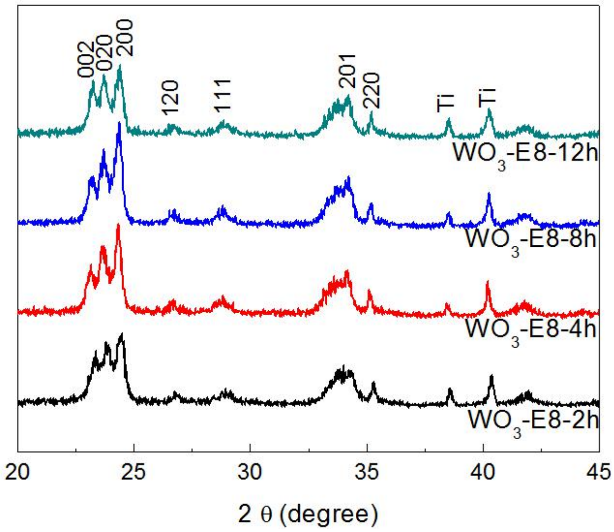

**Figure 5-3**. XRD results of $WO_3$-E8 with different annealing times at 500 °C.

The crystal structure of $WO_3$ NFs was analyzed by the HRTEM technology further. As shown in **Figure 5-5A**, a pseudo-square shaped nanosheet is observed for the film with 8 h hydrothermal treatment and 2 h annealing ($WO_3$-E8-2h). The SEAD pattern obtained from the nanosheet (**Figure 5-5B**) could be indexed as [010] zone axis of monoclinic $WO_3$ crystal (**Figure 5-5C**) with the lattice parameters mentioned above. It indicates a well-developed single crystalline morphology formed in the hydrothermal and subsequent annealing process. However, as shown in **Figure 5-5D**, obvious dislocation line can be observed in the HRTEM image of the selected area in **Figure 5-5A**. By applying inverse fast Fourier transformation (IFFT) with the generator (200) diffracted vector (inset of Panel (E) in **Figure 5-5**), an edge dislocation line is clearly revealed by using a red arrow. A semi-plane was apparent at the dislocation core area. As illustrated in **Figure 5-5F**, the Burgers circus was plotted in the IFFT image which is created from the both diffracted vectors (200) and (002). It is clear that there is a gap between the start point and the end point of the Burgers circus. The difference vector defines the Burgers vector of this edge dislocation. The vector is assigned to [100]/2 as it is parallel to the normal of the plane (200), and it

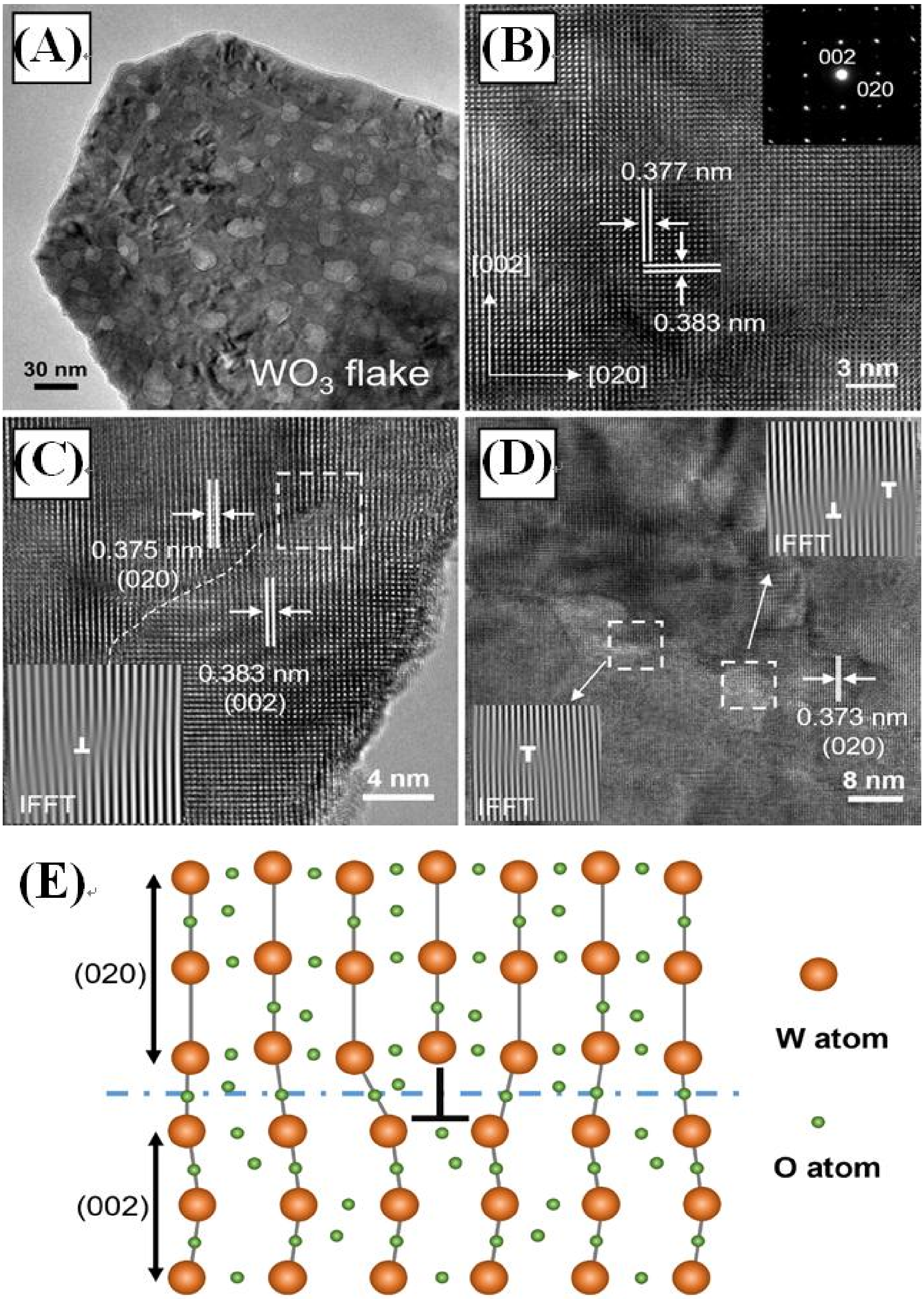

**Figure 5-4**. TEM images of $WO_3$-E8-2h thin film with low (A) and high resolution (B), (C) and (D); Selected area electron diffraction (SAED) pattern for this sample is inserted in (B); and the corresponding IFFT images insert in (C) and (D).

has a length of half of the d-spacing of (100). It is noticed that the Burgers vector [100]/2 is perpendicular to the dislocation line (near parallel to the zone axis [010]), which indicates that the dislocation belongs to an edge-type dislocation rather than a screw-type dislocation. The formation of the dislocations on the $WO_3$ nanosheet should be attributed to the keen-edged nanostructures on the surface of Ti substrate. These sharp-edged nanostructures can provide lopsided pressure and extrusion during the growth of $WO_3$ single crystal which leads to the generation of edge-type dislocations on the $WO_3$ nanosheet. As shown in **Figure 5-5G** to **Figure 5-5I**, the Burgers vector of the edge dislocation line is parallel to [100] and formed by inserting a semi-plane of (200).

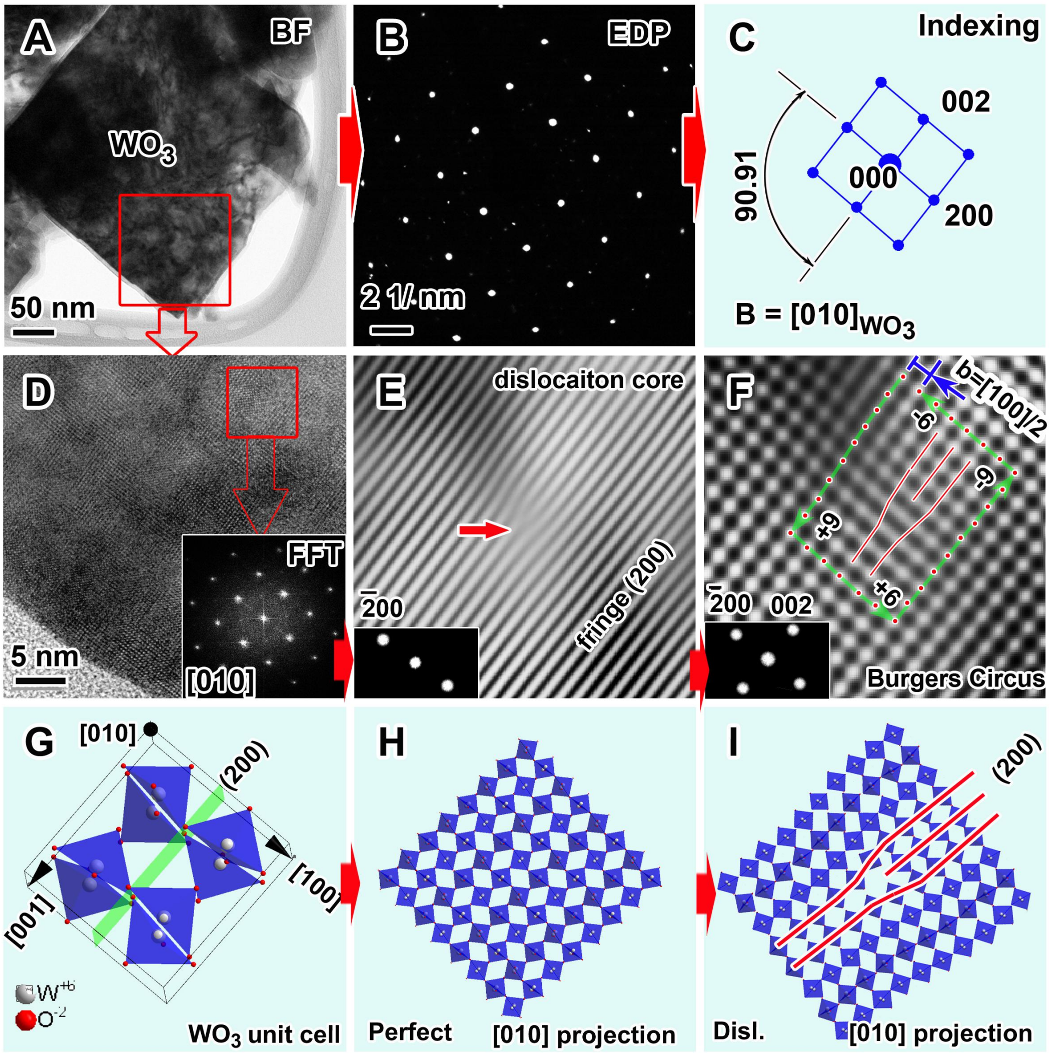

**Figure 5-5**. Transmission electron microscopic (TEM) investigation of dislocation line in monoclinic structure $WO_3$ single crystal. (A) Bright field (BF) image of a pseudo-square shaped $WO_3$ crystal heated for 2 h. (B) The selected area electron diffraction (SAED) pattern corresponding to Panel (A). It can be indexed with the lattice parameters of monoclinic $WO_3$ crystal as shown in Panel (C) where the included angle between (200) and (020). A high resolution TEM image in Panel (D) shows well defined crystalline lattice fringes of planes (200) and (020). Inset of Panel (D) is the fast Fourier transformation (FFT) image which is identical to the EDP in

Panel (B). (E) An inverse FFT image generated by using the diffracted vector (200) only (in-set) indicates a single edge dislocation (red arrow) highlighted by mono planar fringe of (200). The indexing of this Burgers vector as shown in Panel (E) is plotted in Panel (F) which was created by using both (200) and (002) diffracted vectors. As shown by semi-transparent green Burger circus, the Burgers vector of this edge dislocation could be assigned to [100]/2. (G) to (I) are the Burgers vector of the edge dislocation line is parallel to [100] and formed by inserting a semi-plane of (200).

We tried to identify the dislocation line density in the monoclinic crystal $WO_3$ by using the Burgers vector of edge dislocation line in monoclinic crystal $WO_3$.

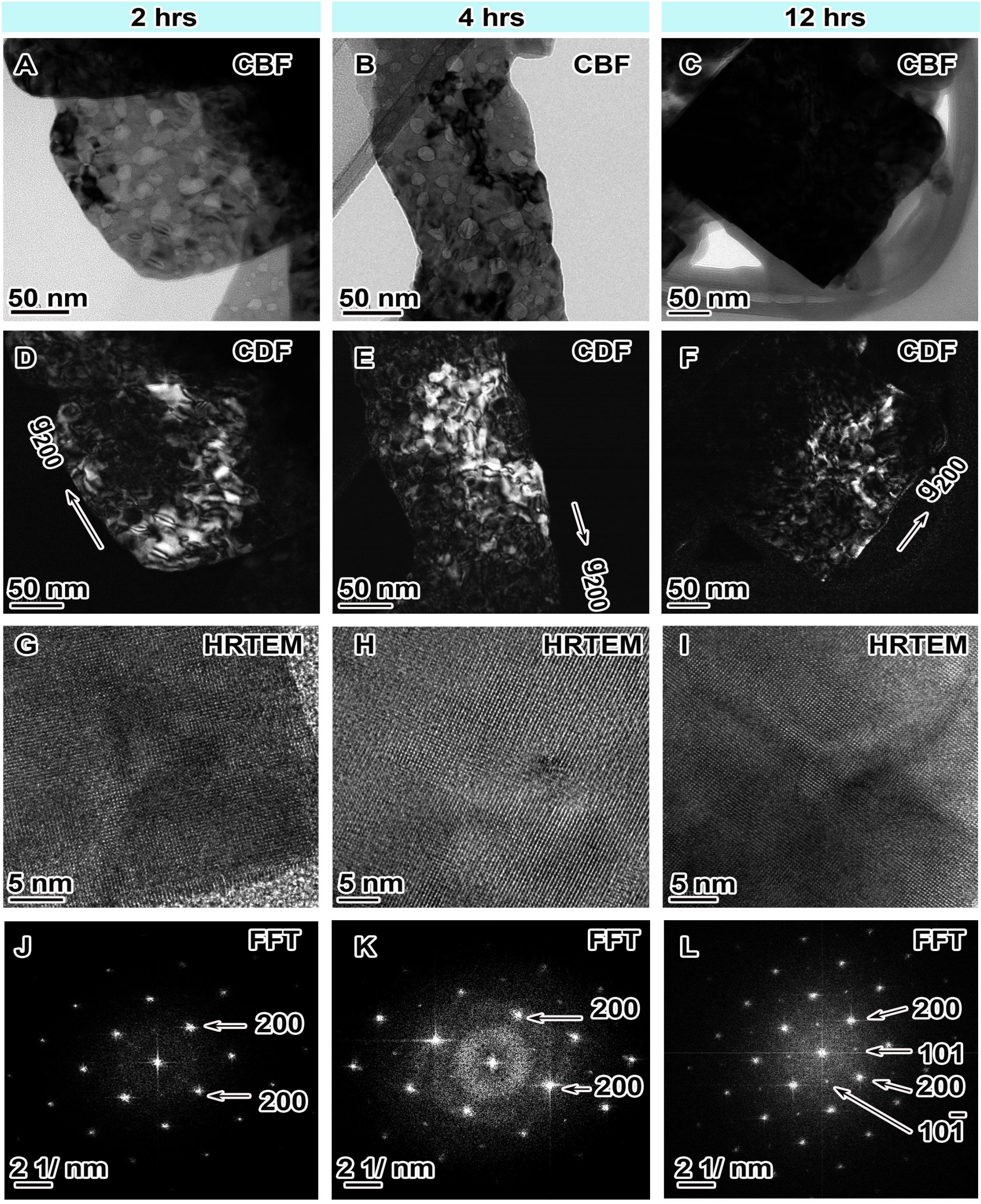

**Figure 5-6.** TEM characterizations of dislocation lines in $WO_3$ samples heated for 2, 4 and 12 h

separated. (A) to (C) are bright field image of a single crystal $WO_3$ which indicated a transition stage of morphology evolution and the degree of crystallinity. (D) to (F) are the corresponding centered dark field images by using diffracted vector (200). (G) to (I) are the HRTEM images separately where the FFT images showed a clear super diffraction {101} sharpening during the elongation of heating.

A dislocation line has only one Burgers vector **V**, which defines the tension of the dislocation. If this vector is lining in a plane (hkl) noted as $\mathbf{g}_{\mathbf{hkl}}$, the magnified image does not show the contrast of this dislocation line. This is due to that the amplitude is proportional to the point product of the two vectors, i.e., $\mathbf{V} \cdot \mathbf{g}_{\mathbf{hkl}}$. So this gives us a chance to identify dislocation qualitatively. When an incident electron beam travels along the microscope optical axis and penetrating the crystalline sample containing a dislocation area, we can determine the dislocation quantity from the magnified image under centered bright field illumination condition (using transmitted electron beam parallel to optical axis) or under centered dark field illumination condition (using diffracted electron beam parallel to optical axis). Herein, the dislocation lines were illustrated by using the diffracted vector (200) to generate centered dark field image for each of the three $WO_3$ samples. More dislocation lines are visible, higher density of dislocation exists in the investigated sample. The comparison of bright field TEM images (Figure 5-6A to 5-6C) and centered dark field images (Figure 5-6D to Figure 5-6F) indicates that the density of dislocation lines (white color line features in dark filed images) reduces gradually with the extension of thermal treatment time. As shown in Figure 5-6G to Figure 5-6L, the evolution from defect-rich to well-crystalized $WO_3$ was also confirmed by appearance of sharpening diffraction spots of {101} planes during the heating stage. It is proposed that there exist such a competition between the decreasing of the density of dislocation lines and the sharpening of super diffraction {101} plane. Given that the surface pits on $WO_3$ crystals make little effect to bulk crystal growth even though the size of such pits enlarging and the number of the pits reducing, both the dislocation line and super diffraction {101} are dominating the final crystallinity of the monoclinic $WO_3$ crystal.

### §5.3.3. PEC performance of $WO_3$ photoanodes

For proving the function of dislocation on $WO_3$ NF photoanode, the photoelectrochemical performance of these samples were tested, and the results present in Fig. 4. Fig. 4A and 4B present the photoinduced I-V curves and IPCE values of $WO_3$-E8-2h and $WO_3$-E8-12h NF photoanodes, respectively. Because of the sample with 8 h hydrothermal growth time shows the better PEC performance than other growth time samples, the $WO_3$ photoanode with 8 h hydrothermal growth time was employed to research further.

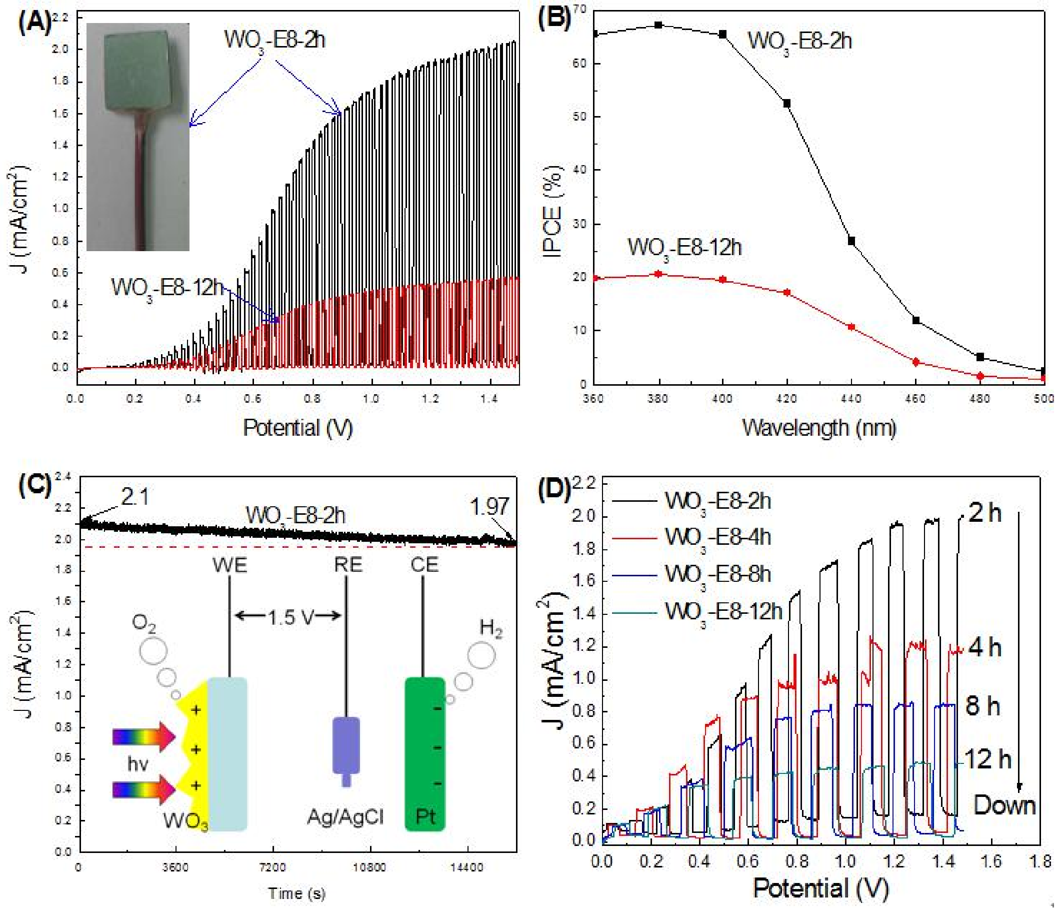

**Figure 5-7.** (A) Photoinduced I-V curves (B) IPCE curves of $WO_3$-E8-2h and $WO_3$-E8-12h testing at a bias potential 1.5 V (vs Ag/AgCl); (C) Photoinduced I-V curves of $WO_3$ photoanodes with different annealing times; (D) Photoinduced I-t curve of $WO_3$-E8-2h with a 4.5 h testing. All test carried out in 0.1 M $Na_2SO_4$ electrolyte, for photoinduced I-V curves and photoincuced I-t curve testing, a 100 mW/cm$^2$ AM 1.5 G was employed.

As shown in Figure 5-7A, the photocurrent density of $WO_3$-E8-2h NF photoanode increased sharply with the bias potential scanning from 0 V to 1.5 V, which increase tendency is much sharper than that of $WO_3$-E8-12h NF photoanode. IPCE values about these two samples are showed in Figure 5-7B. When the wavelength of the incident light less than 420 nm, the IPCE value of $WO_3$-E8-2h NF photoanode is keep over 70%, which value nearly triples higher than $WO_3$-E8-12h NF photoanodes. The IPCE values of both samples decrease quickly with the wavelength higher than 420 nm, meaning that $WO_3$-E8-2h photoanode shows higher conversion capacity for the light with the wavelength less than 420 nm. Figure 5-7C presents the photocurrent stability of $WO_3$-E8-2h NF photoanode, and the testing system is inserted in this figure. From the photoinduced current curve, we can find that the photocurrent slightly decreased for 2.1 mA/cm$^2$ to 1.97 mA/cm$^2$ for a 4.5 h continuous illumination, indicating a steady PEC performance of $WO_3$-E8-2h NF photoanode.

Figure 5-7D presents the photoinduced I-V curves of $WO_3$ NF like photoanodes with difference annealing times at 500 °C. The TEM results have proved that the dislocation density was decreased gradually with the annealing time extending. As shown in Fig. 4C, the photocurrent density of each photoanode decay gradually with the annealing time increasing. Meanwhile, we can obtain the information from the SEM (Figure 5-1A and Figure 5-1B) and XRD (Figure 5-3) of these samples that the nano morphology and crystal structure of the $WO_3$ NF thin film did not change with the annealing time extending from 2 h to 12 h at 500 °C. Thus, combination of the TEM results, the dislocation density on the $WO_3$ single crystal can improve the PEC performance of the $WO_3$ NF photoanode.

### §5.3.4. Theoretical Calculation

With the formation of dislocation on $WO_3$ NF photoanode, as shown in the Figure 5-4 and Figure 5-5, the (020) and (002) are exposed along with the dislocation line. This defect structure may provide a facet heterojunction static electric field to improve the photogenerated charge separation capacity. Thus, the theoretical calculation method was employed to confirm the band energy structures and water splitting reaction active energy of the (020) and (002) facets. As shown in Figure 5-8A to Figure 5-8C, the γ-monoclinic $WO_3$ (space group $P2_1/n$) was obtained from previous works.[7] Figure 5-8D shows the calculated Density of states (DOS) and the simplified diagram of different energy levels for (002) and (020) facets of monoclinic $WO_3$ by density functional theory. The differences of the energy levels in the conduction bands ($\Delta E_g$ (CB)) and the valence bands ($\Delta E_g$ (VB)) between the (002) and {020} facets are computed about 0.38 and 0.23 eV, respectively, which means the spatial charge separation between (002) and (020) facets is feasible because of their different band energy levels. This phenomenon is similar to the surface facet heterojunction effective for the improving of photogenerated carriers separation rate. As shown in the insert of Figure 5-8D, the photogenerated electrons will transfer from the (002) to (020), and the holes will transfer from the (020) to (002). Based on the rectification effect of n-type $WO_3$, the OER reaction induced by photogenerated holes will happen on its surface, so the OER energy barrier on the two facets should be assessed. The radical O, OH, and OOH are put onto (002) and (020) surfaces of γ-monoclinic $WO_3$, which are the model of *O, *OH and *OOH. We plotted the free energy profile to describe OER sub-steps on (002) and (020) surfaces of γ-monoclinic $WO_3$ in acidic environment (as shown in Figure 5-8E and Figure 5-8F). We found that the OER steps on (020) surface is downhill first, then uphill at zero potential, but on (002) surface, this trend is uphill. However, it is worthy of noting that some of the intermediate steps turn to be downhill both on (002) and (020) surfaces with the increase of potential. In the case of (002) surface, the maximum value of the potential at which all reactions are still exothermic is 3.23 V, while the same is 3.50 V in the case of (020) surface. Therefore, the (002) surface is a slightly better candidate as an OER catalyst in acidic medium than the (020) surface. Especially, the OER on the two surfaces preferentially follows the 4e reduction pathway rather than the 2e reduction pathway, which is a big advantage for the $WO_3$ as OER catalyst.

Combining the above results, the possible function of dislocations in the $WO_3$ crystal is shown in Figure 5-8G. We introduced a Taosim idea “Tai-ji” to explain the function of dislocation in the separation process of photogernerated carriers. “Tai-ji” is an energy balance system, which is united by a cathode and anode. Although the energies of the anode and cathode are different, they can limit each other to keep balance. The situation of a well-defined $WO_3$ crystal is similar to the “Tai-ji” system. In the case of $WO_3$-E8-2h, the energy balance in the crystal would be broken when a mismatch formation between (002) and (020) facets. So, combining with Figure 5-8D, this un-balanced energy can promote the transport process of the photogenerated electrons from (002) to (020) facets, and holes from (020) to (002) facets, which means the spatial charge separation between (002) and (020) facet is feasible because of their different energy levels.

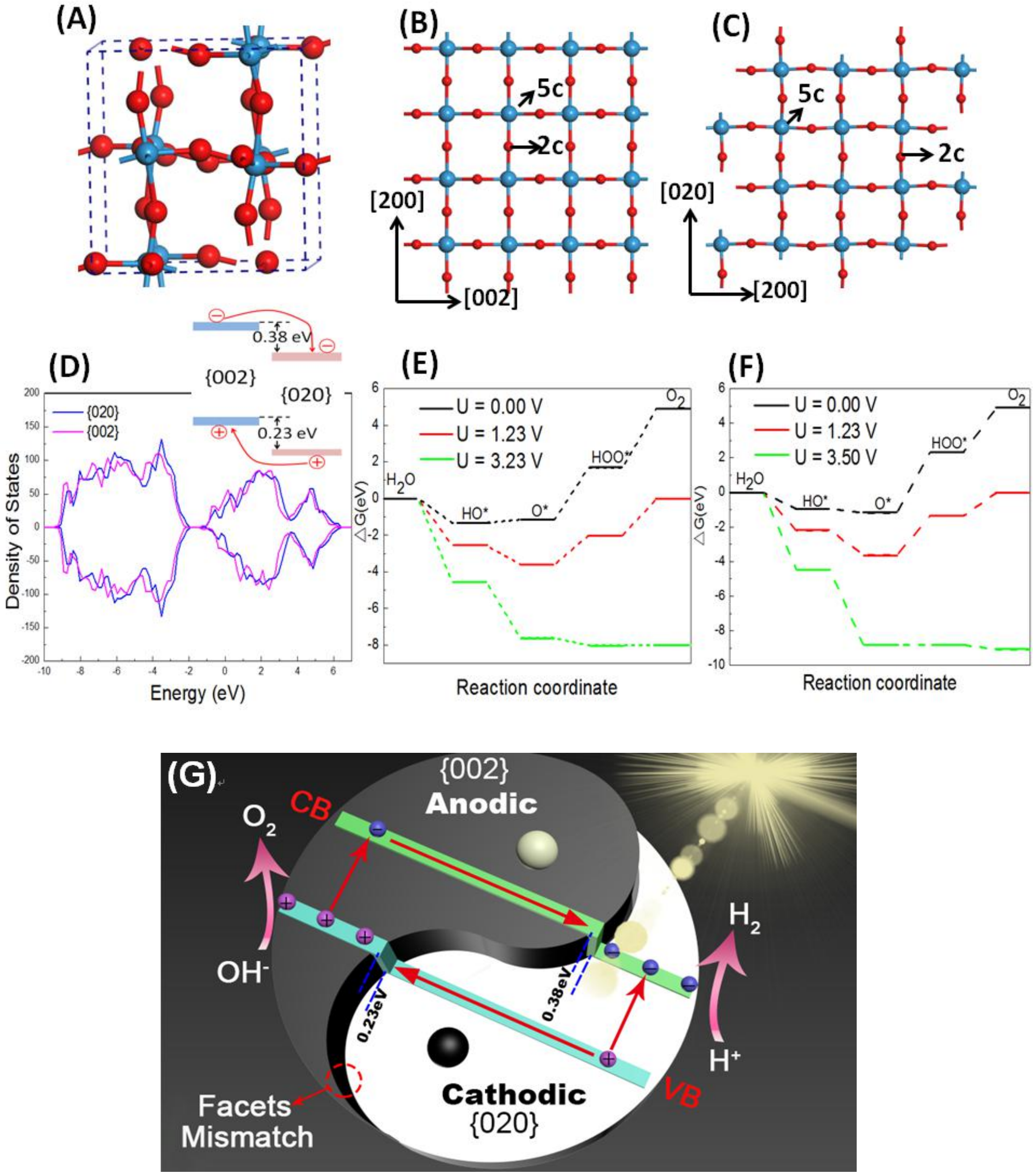

**Figure 5-8**. Schematic atomic structures of γ-monoclinic $WO_3$: (A) the unit cell of γ-monoclinic $WO_3$; (B) Top view of one-layer (010) surface; (C) Top view of one-layer (002) surface; (D) DOS density of the (020) and (002) facets; (E) and (F) Free energy diagrams for OER pathway on (020) and (002) surfaces, respectively. The large blue and small red spheres represent W and O atoms, respectively; (G) Photogenerated carriers separation mechanism at the dislocation interface stacking by ( 002) and (020) facets mismatch.

## §5.4. Conclusion

In this chapter, we reported a NF like $WO_3$ single crystal thin film photoanode, and achieved a 1.8 $mA\cdot cm^{-2}$ photocurrent density at a bias potential of 1.0 V (vs

Ag/AgCl), under AM 1.5 G one sun illumination in $Na_2SO_4$ electrolyte, this is the highest value of pure $WO_3$ photoanode at the same test conditions. More importantly, we find that many dislocations distributed on the surface of $WO_3$ NF resulted from mismatching of {002} and {020} facets. The density of dislocations on $WO_3$ NF could be decreased by extending the annealing time at 500 °C, meanwhile, the photocurrent densities of them were decreased gradually with the dislocation density decreasing. The results of DOS calculation showed that along the mismatch interface of dislocation, the photogenerated hot carriers can be separated by this dislocation interface driving because of the energy difference of {002} and {020} facets, and can improve the photocurrent density of $WO_3$ photoanode.

## §5.4. Reference

[1] X. Liu, F. Wang and Q. Wang, "Nanostructure-based $WO_3$ photoanodes for photoelectrochemical water splitting," *Phys. Chem. Chem. Phys.,* 14, (2012) 7894.

[2] W. Li, P. Da, Y. Zhang, Y. Wang, X. Lin, X. Gong and G. Zheng, "$WO_3$ nanoflakes for enhanced photoelectrochemical conversion," *ACS nano.* 8, (2014) 11770.

[3] G. Wang, Y. Ling, H. Wang, X. Yang, C. Wang, J.Z. Zhang and Y. Li, "Hydrogen-treated WO3 nanoflakes show enhanced photostability," *Energy & Environ. Sci.*, 5, (2012) 6180.

[4] Z. Jiao, J. Wang, L. Ke, X.W. Sun and H.V. Demir, "Morphology-tailored synthesis of tungsten trioxide (hydrate) thin films and their photocatalytic properties," *ACS Appl.Mater. Interfaces,* 3, (2011) 229.

[5] N.Wang, D.Wang, M. Li, J. Shi and C. Li, "Photoelectrochemical water oxidation on photoanodes fabricated with hexagonal nanoflower and nanoblock $WO_3$," *Nanoscale,* 6, (2014) 2061.

[6] K.Zhang, X.J. Shi, J.K. Kim and J.H. Park, "Photoelectrochemical cells with tungsten trioxide/Mo-doped $BiVO_4$ bilayers," *Phys. Chem. Chem. Phys.,* 14, (2012) 11119.

[7] J. Su, L. Guo, N. Bao and C.A. Grimes, "Nanostructured $WO_3$/$BiVO_4$ heterojunction films for efficient photoelectrochemical water splitting," *Nano lett.s,* 11, (2011) 1928.

[8] Y. Pihosh, I. Turkevych, K. Mawatari, T. Asai, T. Hisatomi, J. Uemura, M. Tosa,

K. Shimamura, J. Kubota, K. Domen and T. Kitamori, “Nanostructured $WO_3/BiVO_4$ photoanodes for efficient photoelectrochemical water splitting,” *Small,* 10, (2014) 3692.

[9] P.M. Rao, L. Cai, C. Liu, I.S. Cho, C.H. Lee, J.M. Weisse, P. Yang and X. Zheng, “Simultaneously efficient light absorption and charge separation in $WO_3/BiVO_4$ core/shell nanowire photoanode for photoelectrochemical water oxidation,” *Nano lett.,* 14, (2014) 1099.

[10] K.M. Schindler and M. Kunst, “Charge-carrier dynamics in titania powders,” *J. Phys. Chem.,* 94, (1990) 8222.

[11] G. Yu, C.H. Lee, A.J. Heeger, N. Herron, E.M. Mccarron, L. Cong, G.C. Spalding, C.A. Nordman and A.M. Goldman, “Phase separation of photogenerated carriers and photoinduced superconductivity in high-T c materials,” *Phys. Rev. B,* 45, (1992) 4964.

[12] R. Marschall, “Semiconductor composites: strategies for enhancing charge carrier separation to improve photocatalytic activity,” *Adv. Funct. Mater.,* 24, (2014) 2421.

[13] S. Selcuk, A. Selloni, “Facet-dependent trapping and dynamics of excess electrons at anatase $TiO_2$ surfaces and aqueous interfaces,” *Nat. Mater.,* 15, (2016) 110.

[14] J. Yu, J. Low, W. Xiao, P. Zhou and M. Jaroniec, “Enhanced photocatalytic $CO_2$-reduction activity of anatase $TiO_2$ by coexposed {001} and {101} facets,” *J. Am. Chem.Soc.,* 136, (2014) 8839.

[15] N. Roy, Y. Sohn and D. Pradhan, “Synergy of low-energy {101} and high-energy {001} $TiO_2$ crystal facets for enhanced photocatalysis,” *ACS nano,* 7, (2013) 2532.

[16] R. Li, F. Zhang, D. Wang, J. Yang, M. Li, J. Zhu, X. Zhou, H. Han, C. Li, “Spatial separation of photogenerated electrons and holes among {010} and {110} crystal facets of $BiVO_4$,” *Nat. Comm.,* 4, (2013) 1432 .

[17] R. Li, H. Han, F. Zhang, D. Wang and C. Li, “Highly efficient photocatalysts constructed by rational assembly of dual-cocatalysts separately on different facets of $BiVO_4$,” *Energy Environ. Sci.*, 7, (2014) 1369.

[18] J. Zhu, F. Fan, R. Chen, H. An, Z. Feng and C. Li, “Direct imaging of highly anisotropic photogenerated charge separations on different facets of a single $BiVO_4$

photocatalyst," *Angew. Chem. Inter. Ed.*, 127, (2015) 9239.

[19] G. Fu, S. Yan, T. Yu and Z. Zou, "Oxygen related recombination defects in $Ta_3N_5$ water splitting photoanode," *Appl. Phys. Lett.,* 107, (2015) 171902.

[20] H. Wang, L. Jia, P. Bogdanoff, S. Fiechter, H. Möhwald and D. Shchukin, "Size-related native defect engineering in high intensity ultrasonication of nanoparticles for photoelectrochemical water splitting," *Energy Environ.Sci.*, 6, (2013) 799.

[21] N. Zhang, X. Li, H. Ye, S. Chen, H. Ju, D. Liu, Y. Lin, W. Ye, C. Wang, Q. Xu, J. Zhu, L. Song, J. Jiang and Y. Xiong, "Oxide Defect Engineering Enables to Couple Solar Energy into Oxygen Activation," *J. Am. Chem. Soc.,* 138, (2016) 8928.

[22] X. Chen, L. Liu, Y.Y. Peter and S.S. Mao, "Increasing solar absorption for photocatalysis with black hydrogenated titanium dioxide nanocrystals," *Science,* 331, (2011) 746.

[23] L. Liu, Y.Y.Peter, X. Chen, S.S. Mao and D.Z. Shen, "Hydrogenation and disorder in engineered black $TiO_2$," *Phys.Rev.Lett.* 111, (2013) 065505.

[24] R.L. Penn and J.F. Banfield, "Imperfect oriented attachment: dislocation generation in defect-free nanocrystals," *Science,* 281, (1998) 969.

[25] C.L. Kelchner, S.J. Plimpton and J.C. Hamilton, "Dislocation nucleation and defect structure during surface indentation," *Phys. Rev. B,* 58, (1998) 11085.

[26] D.J. Eaglesham and M. Cerullo, "Dislocation-free stranski-krastanow growth of Ge on Si (100)," *Phys. Rev. Lett.,* 64, (1990) 1943.

[27] B.O. Loopstra, P. Boldrini, "Neutron diffraction investigation of $WO_3$," *Acta Crystallographica,* 21, (1966) 158.

[28] M. Armbrüster, H. Borrmann, M. Wedel, Y. Prots, R. Giedigkeit and P. Gille, "Refinement of the crystal structure of palladium gallium (1:1), PdGa," *Zeitschrift für Kristallographie-New Crystal Structures,* 225, (2010) 617.

[29] G. Kresse and J. Hafner, "Ab initio molecular dynamics for liquid metals," *Phys. Rev. B,* 47, (1993) 558 .

[30] G. Kresse and J. Furthmüller, "Efficient iterative schemes for ab initio total-energy calculations using a plane-wave basis set," *Phys. Rev. B,* 54, (1996), 11169 .

[31] G. Kresse, and J. Furthmüller, "Efficiency of ab-initio total energy calculations for metals and semiconductors using a plane-wave basis set," *Comput. Mater. Sci.,*6,

(1996), 15.

[32] G. Kresse and J. Furthmüller, "Efficient iterative schemes for ab initio total-energy calculations using a plane-wave basis set," *Phys. Rev. B,* 54, (1996) 11169 .

[33] D. Vanderbilt, "Soft self-consistent pseudopotentials in a generalized eigenvalue formalism," *Phys. Rev. B,* 41, (1990) 7892 .

[34] B.O. Loopstra and P. Boldrini, "Neutron diffraction investigation of $WO_3$," *Acta Crystallographica,* 21, (1966) 158.

[35] M. Levy, and T. Pagnier, "Ab initio DFT computation of $SnO_2$ and $WO_3$ slabs and gas-surface interactions," *Sens. Actuators B: Chemical,* 126, (2007) 204.

[36] I.N. Yakovkin, and M. Gutowski, "Driving force for the $WO_3$ (001) surface relaxation," *Surf.Sci.,* 601, (2007) 1481.

[37] S. Ling, D. Mei, and M. Gutowski, "Reactivity of hydrogen and methanol on (001) surfaces of $WO_3$, $ReO_3$, $WO_3/ReO_3$ and $ReO_3/WO_3$," *Catal. Today,* 165, (2011) 41.

[38] A. Valdes, and G.J. Kroes, "First principles study of the photo-oxidation of water on tungsten trioxide ($WO_3$)," *J.Chem.Phys.,* 130, (2009) 114701.

[39] H. Jin, J. Zhu, J. Hu, Y. Li, Y. Zhang, X. Huang, K. Ding, W. Chen, "Structural and electronic properties of tungsten trioxides: from cluster to solid surface," *Theor. Chem. Acc.*, 130, (2011) 103.

[40] C. Lambert-Mauriat, V. Oison, L. Saadi, and K. Aguir, "Ab initio study of oxygen point defects on tungsten trioxide surface," *Surf. Sci.,* 606, (2012) 40.

# Chapter 6: Conclusions and Future Works

## §6.1. Summary and Conclusions

Photoelectrochemical (PEC) water splitting for hydrogen evolution is a potential technique to solve the questions of energy shortage and environment pollution. For improving PEC performance of photoanode, in this thesis, we developed quasi-oxygen vacancy and edge dislocation to modify the Mo-doped $BiVO_4$ and $WO_3$ nanoflower like photoanodes, and the details as follows:

Fistly, we fabricated oxygen vacancy point defect on the surface of BiMoVO photoanode, and the states of the oxygen vacancy was changed along with the reduction potentials increasing. Only the Bi-O bonds on (020) facet was broken, and quasi-oxygen vacancy formed, a highest 4.3 mA/cm$^2$ photocurrent density could be achieved (AM 1.5 G one sun, vs Ag/AgCl 1.5 V). Further experimental data and DFT calculation data indicated that oxygen vacancy was not the real reason to improve the PEC performance of a BiMoVO photoanode, but just some Bi-O bonds broken on the active facet.

Secondly, $WO_3$ well-defended nanoflower like photoanode was fabricated on etched-Ti substrate by hydrothermal method for the first time, and the $WO_3$ single crystal thin film photoanode achieved a 1.8 mA·cm$^{-2}$ photocurrent density at a bias potential of 1.0 V (vs Ag/AgCl), under AM 1.5 G one sun illumination in $Na_2SO_4$ electrolyte, this is the highest value of pure $WO_3$ photoanode at the same test conditions as we know. With the growth time exceed 8 hours, the nanoflower structure of the $WO_3$ thin film disappeared and the PEC performance of the corresponding photoanode was decreased too.

Lastly, further study found that many linear defect dislocations distributed on the surface of $WO_3$ nanoflower by {002} and {020} facets mismatch. The density of dislocations on $WO_3$ nanoflower could be decreased by extending the annealing time at 500 °C, meanwhile, the photocurrent densities of them were decreased gradually with the dislocation density decreasing. Further DOS calculation results shows that at the mismatch interface of dislocation, because of the energy difference of {002} and {020} facets, the photogenerated hot carriers can be separated by this dislocation interface driving, that to improve the photocurrent density of $WO_3$ photoanode.

## §6.2. Suggestion for future works

As shown in chapter 3, the PEC performance of Mo-doped $BiVO_4$ photoanode was improved greatly after surface quasi-oxygen vacancy modification. However, from the photoinduced i-t curve, we can find that the PEC performance stability of the modified photoanode is not well, indicating unstable quasi-oxygen vacancy on the surface of the photoanode. Thus, the stability of the surface quasi-oxygen vacancy need to improve. Deposition of ultrathin nano inert layer or oxygen evolution co-catalysis metal oxide on the surface of quasi-oxygen vacancy modified photoanode can be considered.

In this thesis, chapter 5, the edge dislocation on the surface of $WO_3$ NF photoanode has been proved beneficial for its PEC performance improving. However, the mechanism is still unclear. So, in the near future, some in-situ microscope methods need be developed to research the real function of the dislocation during the PEC process. Furthermore, some proactive methods for dislocation fabrication should be developed, then synthesis more dislocation modified photoanodes or photocatalysts.

# Acknowledgements

The coming September marks the terminus of my journey of doctor study and I would like to take this opportunity to thank all those who have helped and supported me in completing the academic life.

First and foremost, I would like to give my utmost gratitude to my supervisor, Associate Professor Jin-Ping Ao, for his encouragement, patience and selflessness guidance during entire duration of this research work. Moreover, his active attitude and spirit in life also influence me greatly.

Secondly, I would like to thinks my wife Ruiling Wang, for her unselfish assistance in the daily live and help on my Japanese language study. In addition, thanks for her encourage when my research not proceeding well enough.

Many thanks extend to the students Tong Zhang, Tian Xie, Taofei Pu, Zhangcheng Liu, Naoto Okada, Kensaku Yagi, Xiaobo Li, Lei Wang, in Ao group, for their help and patience in my research and life.

I would especially like to thank Prof. Weibing Li in Qingdao University of Science and Technology and her students Jing Tian, Zhiwei Chen and Weiqiang Zheng for the support of photoelectrochemical performance testing.

Last and certainly not the least, I am forever indebted to my parents and family, who have been supporting me through all of the accomplishments of my academic life. Their indefinite love has made the things different in every aspect of my life.

# Biography

Yuyu Bu was born in Chong Qing, China on 1th January 1986.

2004.09-2008.07: he graduated with a Bachelor of Environemnt Science from Qingdao University of Science and Technology, China.

2009.09-2012.07: he was recommended to complete his Master of Science degree in Enivronment Science from Qingdao University of Science and Technology, China.

2012.09-2015.05: he served as an Assistant Engineer in Institute of Oceanology, Chinese Academy of Sciences.

2015.10-present: he has been engaged in the investigation of defect on semiconductor photoanode for photoelectrochemical water splitting in Tokushima University, Tokushima, Japan.

He has received the following awards:

The Research Award of International Exchange, Tokushima University (平成 29 年度国際交流研究奨励賞).

# Publication list

## Scientific Papers

[1] ***Yuyu Bu***, Jing Tian, Zhiwei Chen, Qiang Zhang, Weibing Li, FengHui Tian, Jin-Ping Ao. Optimization of the photoelectrochemical performance of Mo-doped $BiVO_4$ photoanode by controlling the metal-oxygen bonds state on (020) facet, Advanced Materials Interfaces*,* 2017*,* 4*,* 1601235.

[2] ***Yuyu Bu***, Zhiwei Chen, Tian Xie, Weibing Li and Jin-Ping Ao*, Fabrication of $C_3N_4$ ultrathin flakes by mechanical grind method with enhanced photocatalysis and photoelectrochemical performance, RSC Advances, 2016, 6, 47813–47819.

[3] ***Yuyu Bu***, Jin-Ping Ao*, A review on photoelectrochemical cathodic protection semiconductor thin films for metals, Green Energy & Environment, 2017, doi.org/10.1016/j.gee.2017.02.003. (In press)

[4] Lei Wang, ***Yuyu Bu***, Liuan Li*, Jin-Ping Ao*, Effect of thermal oxidation treatment on pH sensitivity of AlGaN/GaN heterostructure ion-sensitive field-effect transistors, Applied Surface Science, 2017, 411, 144–148.

[5] Lei Wang, ***Yuyu Bu***, Jin-Ping Ao*, Effect of oxygen plasma treatment on the performance of AlGaN/GaN ion-sensitive field-effect transistors, Diamond & Related Materials, 2017, 73, 1–6.

[6] Weibing Li, Yaping Zhang, **Y*uyu Bu***, Zhuoyuan Chen*, One-pot synthesis of the $BiVO_4$/BiOBr heterojunction composite for enhanced photocatalytic performance, Journal of Alloys and Compounds, 2016, 680, 677-684.

[7] Weibing Li, Yaping Zhang, Guodong Tian, Shuya Xie, Qingqing Xu, Lin Wang, Jiming Tian, ***Yuyu Bu*****, Fabrication of graphene-modified nano-sized red phosphorus for enhanced photocatalytic performance, Journal of Molecular Catalysis A: Chemical, 2016, 423, 356-364.

[8] Hongwei Wang, Wenqiang Zheng, Weibing Li, FengHui Tiana, Shaoping Kuang, ***Yuyu Bu****, Jin-Ping Ao, Control the energy band potential of ZnMgO solid solution with enhanced photocatalytic hydrogen evolution capacity, Applied Catalysis B: Environmental, 2017, 217, 523–529.

## International Conference Presentations

[1] ***Yuyu Bu***, Weibing Li, Jin-Ping Ao, Fabrication of Large-scaled Multilayer $C_3N_4$ Ultrathin Flake by Mechanical Grind Method with Enhanced Photocatalysis

Performance(Poster). 10th International Conference on New Diamond and Nano Carbons, 2016, May 22~26, Xi'an, China.

[2] ***Yuyu Bu***, Tian Xie, Weibing Li, Jin-Ping Ao. Fabricating of $WO_3$ Nanoflower Like Photoanode for Water Oxidation (Oral), 26th IUPAC International Symposium of Photochmistry, 2016, April 3~8, Osaka, Japan.